Local Optics Corrections in the HL-LHC

Thesis dissertation defended by

Jaime María Coello de Portugal - Martínez Vázquez

Directed by: Dr. Rogelio Tomás García and Dr. Yuri Kubyshin

Nuclear Engineering and Ionising Radiation PhD programme

Institut de Tècniques Energètiques

February, 2021

Abstract

In order to push the performance of current and future particle colliders, it is necessary to drive the beams at the locations of the experiments to decreasingly smaller sizes. This progress towards smaller beam sizes in the interaction points requires accelerators that must accommodate larger beam sizes in the surroundings and therefore strong magnetic errors in these regions must be suppressed. This thesis presents a study on the consequences of these magnetic errors and several mitigation techniques to correct their influence.

As a specific example, in this thesis the quadrupole triplet of the future HL-LHC is studied. Simulations of its expected magnetic errors are carried out and their correctability is assessed. For this a new automatic local correction algorithm is also presented which allows to perform Monte-Carlo simulations of the errors and their corrections.

In recent years it has become clear that the main limiting factor to control the beam size in the interaction points is the quality of the measurement of the β-function at this point. In this thesis some of the limitations of the current measurement method, K-modulation, are studied, some developments made to improve the accuracy of this method are discussed and two new complementary techniques that are expected to surpass its accuracy are presented.

These new techniques are the computation of the minimum β near the IP using the betatron phase measured with new instrumentation and a procedure to locate the beam waist via luminosity scans. These two techniques are presented both with their theoretical framework and their experimental validation on the LHC. These are the first results of a possible complement to the K-modulation method in future colliders.

The optics scheme that has been used in the LHC and is going to be used in HL-LHC pushes the β-functions to higher values also far away from the interaction regions. It has been observed in the LHC that this scheme enhances the magnetic errors of the arc magnets too, where there are no correctors to control local errors available. In the thesis, in order to counteract these errors, it is proposed to implement optics correction using orbit bumps over sextupoles, thus correcting the optics errors via feed-down for the first time in the LHC.

These results suggest that drastic changes in the commissioning strategy will be necessary in the HL-LHC, as they will require intermediate luminosity measurements.

To accommodate the larger beam sizes expected in HL-LHC, the new Nb_3Sn superconductor technology is going to be used in the HL–LHC triplet, which allows to increase the magnets aperture while keeping the same magnetic field strength on the central axis. However, the superconductors built using this technology show an unstable behaviour during magnetic-field ramps, this effect is called flux jumps.

In this thesis the effect of flux jumps on the beam emittance is studied for the first time. The studied case is of two 11 T dipoles that are going to be installed in the LHC, in the HL–LHC triplet and in the main bending dipoles of the FCC-hh.

Finally, many of the software improvements developed during the studies presented in this thesis are also described. These include a thorough process of refactoring of outdated software tools, introducing modern data analysis frameworks. A graphical user interface to handle the automatic local correction algorithm which makes easier the computation of these sometimes complex corrections is briefly presented. A new harmonic analysis framework designed to replace older tools, whose development had been frozen, is also described. This new framework has allowed to further develop the harmonic analysis algorithms for optics measurements, improving their precision and performance.

Acknowledgements

Firstly, I would like to acknowledge the massive help I received during these many years from my supervisor Rogelio Tomas Garcia. Without his great advice and guidance this thesis would not have been possible. Also, many thanks to my university supervisor Yuri Kubyshin, for the great comments and corrections that significantly improved this work and for patient handling the administrative procedures with the university.

I extend my acknowledgements to Massimo Giovannozzi and Gianluigi Arduini, for the very interesting comments during the presentations of my research and proofreading my publications.

I would like to continue thanking all the colleagues that helped me across this long, tough, and fun journey. In more or less chronological order:

To Andy Sven Lagner, for being a great guiding hand in my first contact with the software of the team and helping me breach the gap between computing and physics.

To Piotr Skowronski, Ewen Hamish Maclean, and Tobias Persson, for setting the basis of a big part of my research and for all their guidance in Accelerator Physics in the different projects on which we worked together. May the GUI not break again.

To Felix Carlier, for somehow making fun escaping the many physics and programming pits we encountered. Escape that sometimes took us to some shady clubs in Geneva.

To Ana Garcia-Tabares, or "Anaaaaaa" in case of emergency, for many hours we spent navigating the rocks we encountered in that sea that is the Beta-Beat.src. Did you learn git already?

To Lukas Malina, for coming with me in the sneaky ways to developing the secret projects and the huge effort improving and cleaning the team's programs.

To Elena Fol, firstly for the many hours teaming up to develop and fix team's programs and after for the great time learning together how to teach the machines, which have been such an useful tool in my career.

To Joschua Dilly, for the time we spent thinking how to push for the finest quality in our software and for continuing this effort. See you in the other side.

To Andreas Wegscheider, for the fun time spent investigating that interest we share on original programming languages. One day, we will see some of them sneaking into our software.

To Michael Hofer, for keeping me up to date with the social life in the group and the latest developments in our field. I will resist saying thanks for the organisation of the many hikes too.

Also, for making me have such a great time in Geneva, both at work and outside, I would like to

thank Fabien Plassard, Michael Schenk, Xavier Valls and Elena Villhauer.

In conclusion to all the members of the Optics Measurements and Corrections team and friends made during my studies, thank you all... for taking me home.

Finally, I will like to thank my family and friends back in Spain, for their continuous support and advice all these years, even across the long distances and for coping with my... detached personality. Even if I tend not to show it that much, you help me a great deal.

Contents

Chapter 1

Introduction

Accelerator Physics is the branch of physics that studies machines designed to store and typically accelerate charged particles using electromagnetic fields under controlled conditions to be used commonly for medical or industrial applications or for fundamental research. Furthermore, this science tries to describe the behaviour of the particles inside these machines, called Particle Accelerators.

The discovery of the atomic nucleus using natural radioactive sources and the interest in studying it deeply, motivated the invention of the first man-made particle accelerator, designed in collaboration by J. D. Cockcroft and E. Walton with which they achieved the first artificial nuclear disintegration [1].

Since then, the progress of high energy physics, which has historically been the main drive of the progress of accelerator physics, has required particle beams of increasing energy.

This requirement of higher energies motivated the design of different accelerator geometries, being the successor of the Cockcroft-Walton electrostatic accelerator the Cyclotron, invented by E. O. Lawrence. In cyclotrons the beam is kept in a curved trajectory using a magnetic field and is accelerated many times by an oscillating electric field making the beam to move in spiral outwards as it energy increases.

Cyclotron energy is limited to few percent of the speed of light though, when relativistic effects start to be significant. The synchrotron, invented by V. Veksler in 1944, is a more complicated particle accelerator that keeps the particle beam turning with a constant radius. To achieve this, the bending strength of dipoles is kept synchronized with the increasing energy of the beam. Nowadays, the world's most energetic particle beams have been achieved using synchrotrons being nowadays the largest the Large Hadron Collider (LHC).

The LHC and its high luminosity upgrade, High Luminosity LHC (HL-LHC), are the central focus of this thesis. In this chapter an introduction to transversal beam dynamics and beam optics follows, describing then the main characteristics of the LHC and the HL-LHC and providing an introduction on how the beam optics are measured and corrected on this machine.

Chapter 2 studies if current approaches used to measure and correct strong localised magnetic errors will be precise enough on the HL-LHC. Some issues of current approaches to characterise the beam optics at the interaction points will be described and a full alternative will be provided, theoretically and experimentally in the LHC. Local magnetic errors sources in the arcs that have been observed in the LHC and will arise in the HL-LHC due to its optics configuration are also

studied and it is demonstrated how to correct this error sources, also with experimental results in the LHC. Most of the studies presented in Chapter 2 have been published in [2].

Chapter 3 presents a study on flux jumps, a type of magnetic errors that happen in superconducting magnets. Flux jumps are expected to be stronger in the HL-LHC final focus triplet as it uses the new Nb_3Sn superconducting technology. The effect on the beam emittance, orbit and tune caused by these flux jumps in the HL-LHC triplet (and the reaction of its current-regulation loop) is studied, with measurements of the effect being performed on prototypes of the magnets. The effect of the flux jumps is also studied on the 11 T dipoles that are planned to be installed in the LHC after Long Shutdown 2. Additionally, flux jumps on the hadron-hadron Future Circular Collider are explored, as this machine is being designed to use this new technology in many more magnets than the HL-LHC. This study has been published in [3].

Chapter 4, presents a summary of many improvements which have been proposed in the framework of this thesis and introduced to the Optics Measurements and Corrections (OMC) software tools. A brief description of these tools is presented, showing the effort that was made on refactoring and adding new features. A new Python Graphical User Interface (GUI) used to easily perform local corrections is described. Also, Harpy, a new implementation in Python of the Laskar algorithm is presented, to serve as a replacement for legacy tools.

Chapter 5 wraps up this thesis summarising its main results and exposing some of the possible follow-ups for the future to the work presented here.

1.1 Beam optics

This section introduces the basics of transverse beam dynamics and more specifically beam optics necessary to define the concepts, equations and figures of merit discussed in the rest of the thesis. Therefore, it will not be an exhaustive manual of beam dynamics. In the present section the transverse equations of motion of beam particles in circular accelerators are introduced. For a more extensive view on general accelerator physics the following books are recommended: [4, 5, 6].

To force the particles inside the accelerator to describe a closed trajectory, they are put through magnetic fields that deflect their trajectories. The force applied to the beam is the Lorentz force F_L given by the equation:

$$\vec{F}_L = q\left(\vec{E} + \vec{v} \times \vec{B}\right) \ , \tag{1.1}$$

where q is the particle charge, $\vec{E}$ the magnetic field, $\vec{v}$ the particle velocity and $\vec{B}$ the magnetic field induction. The particles speed $|\vec{v}|$, which in most accelerators is close to the speed of light makes the force excerpted by the magnetic field significantly stronger than the one produced by the electric field for reasonable values of $|\vec{B}|$ and $|\vec{E}|$, respectively. Therefore, magnetic fields are typically used to guide particles in high energy accelerators.

To steer the beam, dipole magnets with a magnetic field B perpendicular to the beam trajectory are used (Fig. 1.2). For a more convenient description of the trajectory of particles around the accelerator the local moving coordinate system shown in Fig. 1.1 is typically introduced, where s denotes the position of the particle along the ideal orbit (with an arbitrary initial point $s = 0$) and x and y are the horizontal and vertical deviations of the particle position with respect to this ideal

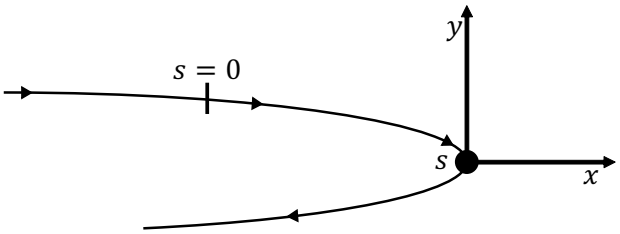

Figure 1.1: Illustration depicting the coordinate system used to describe the particle trajectory. The coordinate system moves with the particle with s describing the path length of the particle along the ideal orbit from some arbitrary initial point $s = 0$ and x and y measuring respectively the horizontal and vertical distance from this ideal orbit.

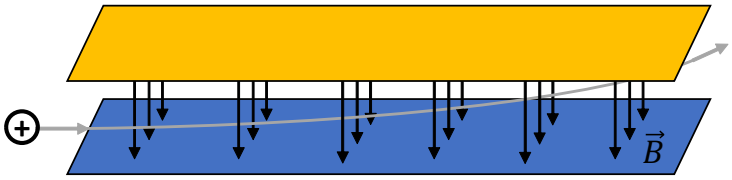

Figure 1.2: Illustration of a dipole magnet producing a magnetic field perpendicular to the beam trajectory. The Lorentz force applied to the beam makes it follow a curved trajectory.

orbit.

The magnetic bending force plays the role of the centripetal force of the beam as it passes through a magnet while moving along the machine ring. Therefore, defining the magnetic field strength and bending radius as functions $B(s)$ and $\rho(s)$ of the position s in the accelerator and denoting $v = |\vec{v}|$, we can derive:

$$m\gamma\frac{v^2}{\rho(s)} = qvB(s) \ , \tag{1.2}$$

where m is the mass of the particle, $\gamma = \left(\sqrt{1-\frac{v^2}{c^2}}\right)^{-1}$ denotes the relativistic Lorentz factor. Rearranging the terms and introducing the particle momentum $p = \gamma mv$ the normalised bending strength

$$\frac{1}{\rho(s)} = \frac{eB(s)}{p} \ , \tag{1.3}$$

is obtained.

Restoring forces are needed to keep the particles oscillating around the ideal trajectory and to stop them from drifting away. Therefore, a Lorentz force, and thus a magnetic field that increases linearly with the transverse deviation from the ideal orbit is needed:

$$\begin{aligned} B_x &= -gy \\ B_y &= -gx, \end{aligned} \tag{1.4}$$

with B_x, B_y being the magnetic field components and g being the magnetic gradient. Quadrupole magnets are used to generate such magnetic fields, acting as magnetic lenses, focusing or defocusing beam trajectories with respect to the ideal orbit. Deflected by these magnetic forces, particles in the accelerator oscillate around the ideal trajectory. These oscillations are called betatron oscillations. Because of the similarity of these restoring forces to optical lenses, the branch of Accelerator Physics that studies the motion of particles under focusing forces is named Beam Optics.

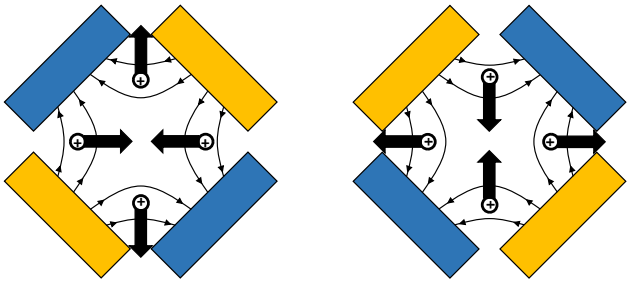

Figure 1.3: Illustration of a quadrupole magnet effect acting on positively charged particles moving into the plane of the drawing away from the reader. Thin lines with arrows are magnetic field lines, thick arrows are magnetic force vectors. On the left, a horizontally focusing magnet is shown, describing how it focuses horizontally deviated particles towards the ideal trajectory and defocuses vertically deviated ones away from it. On the right, a quadrupole magnet with opposite polarity causes a vertically focusing and horizontally defocusing force.

Quadrupole fields though, cannot act as focusing lenses in both the horizontal and vertical planes at the same time, as shown in Fig. 1.3. A horizontally focusing quadrupole defocuses the beam in the vertical plane and the other way around.

Similar to the bending strength, the quadrupole strength k is given by the gradient g normalised to the beam momentum, $k = gq/p$.

The focusing force linear in the particle deviation from the ideal orbit can be interpreted as a restoring force of a harmonic oscillator. The quadrupole force can be viewed as the force excerpted by a spring compressing and elongating to push the particle towards the rest position, namely the ideal orbit at the central axis of a quadrupole. Therefore, the equation of motion of particles subjected to the quadrupole magnetic field is the general differential equation of a harmonic oscillator:

$$z'' + Kz = 0, \tag{1.5}$$

where the prime denotes the derivative with respect to the path length s, z is either x or y and K is the "spring constant" of the oscillator. This equation can be specified for the x- and y-planes as:

$$x'' + \left(\frac{1}{\rho^2} - k\right) x = 0 \tag{1.6}$$

$$y'' + ky = 0 \tag{1.7}$$

The term $1/\rho^2$ that appears in the horizontal plane accounts for the so called "weak focusing" of the dipoles, which applies a restoring force in the horizontal plane even in absence of quadrupoles, but it is weak for large accelerators rings.

The general solution of the differential equation Eq. (1.5) is the linear combination of two independent solutions C(s) and S(s):

$$\begin{aligned} x(s) &= C(s)x_0 + S(s)\frac{x_0'}{\sqrt{K}} \\ x'(s) &= C'(s)x_0 + S'(s)\frac{x_0'}{\sqrt{K}}, \end{aligned} \tag{1.8}$$

where x_0 and $x_0'/\sqrt{K}$ are the coefficients of this linear combination that can be found by imposing

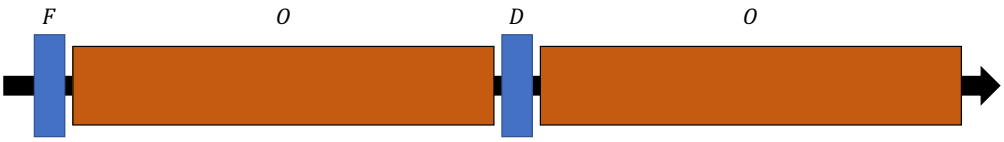

Figure 1.4: Schematic of the FODO cells used to achieve both planes focusing. These are placed in series all over the accelerator circumference.

the initial conditions at $s = 0$. Considering the motion inside a horizontally focusing quadrupole (positive K) the following specific solution is obtained:

$$x(s) = x_0 \cos\left(\sqrt{|K|}s\right) + \frac{x'_0}{\sqrt{|K|}} \sin\left(\sqrt{|K|}s\right) \tag{1.9}$$

$$x'(s) = -x_0\sqrt{|K|} \sin\left(\sqrt{|K|}s\right) + x_0 \cos\left(\sqrt{|K|}s\right) \ . \tag{1.10}$$

The change of the trajectory from the entrance of the quadrupole at $s = s_0$ to its exit at $s = s_1$ can be expressed in matrix notation as:

$$\begin{pmatrix} x \\ x' \end{pmatrix}_{s1} = M_{foc} \begin{pmatrix} x \\ x' \end{pmatrix}_{s0} , \tag{1.11}$$

with, for a quadrupole of length l given by

$$M_{foc} = \begin{pmatrix} \cos(\sqrt{|K|}l) & \frac{1}{\sqrt{|K|}} \sin(\sqrt{|K|}l) \\ -\sqrt{|K|} \sin(\sqrt{|K|}l) & \cos(\sqrt{|K|}l) \end{pmatrix} \tag{1.12}$$

The transport matrices for a horizontally defocusing quadrupole (negative K) and for a drift space (K=0) are:

$$M_{def} = \begin{pmatrix} \cosh(\sqrt{|K|}s) & \frac{1}{\sqrt{|K|}} \sinh(\sqrt{|K|}s) \\ \sqrt{|K|} \sinh(\sqrt{|K|}s) & \cosh(\sqrt{|K|}s) \end{pmatrix}, \ M_{drift} = \begin{pmatrix} 1 & l \\ 0 & 1 \end{pmatrix}. \tag{1.13}$$

In a vertically focusing quadrupole the focusing and defocusing planes swap w.r.t a horizontally focusing quadrupole, and so do their matrices: $M^{hor}_{foc} = M^{ver}_{def}$ and $M^{ver}_{foc} = M^{hor}_{def}$. With these definitions, the overall effect of several focusing and defocusing quadrupole magnets and drift spaces between them on particles trajectories can be computed by multiplying the corresponding matrices.

To achieve an effective focusing in both planes, sets of cells of focusing-defocusing quadrupole pairs, called FODO cells, are used. The typical structure are like the one shown in Fig 1.4. Such cells are put is series all around the accelerator.

While traversing these FODO cells, the beam crosses the spaced focusing and defocusing quadrupoles turn by turn. Therefore, it sees a non-continuous "spring constant" K, which must be a periodic function of the position s in the accelerator with period L, the accelerator ring length (perimeter), so that $K(s) = K(s + L)$.

Using these properties, the equation of motion in the horizontal plane can be written as:

$$x''(s) - K(s)x(s) = 0. \tag{1.14}$$

This is the equation of a harmonic oscillator with periodic restoring properties, in mathematics it is called "Hill's Equation". Its general solution can be written as:

$$x(s) = \sqrt{\epsilon}\sqrt{\beta(s)}\cos(\psi(s) + \phi) \tag{1.15}$$

$$x'(s) = -\frac{\sqrt{\epsilon}}{\sqrt{\beta}(s)}[\alpha(s)\cos(\psi(s) + \phi) + \sin(\psi(s) + \phi)] \tag{1.16}$$

where $\beta(s)$ is the so called β-function, a periodic function ($\beta(s) = \beta(s + L)$) which is determined by the magnetic lattice of the accelerator, the function $\alpha(s)$ is defined as $\alpha(s) = \frac{-1}{2}\beta'(s)$, ϵ is called the single particle emittance and is a constant determined by the initial conditions, and ϕ is the initial phase. The function $\psi(s)$ is given by

$$\psi(s) = \int_{s_0}^{s} \frac{ds}{\beta(s)}, \tag{1.17}$$

that can be checked by introducing Eq. (1.15) into Eq. (1.14). This is the "phase-advance" function between the points s_0 and s of the particles trajectory in the accelerator. The phase-advance for a full revolution around the accelerator is called the tune of the machine and describes the number of oscillations of the particles with respect to the ideal orbit per revolution:

$$Q = \frac{1}{2\pi}\oint \frac{ds}{\beta(s)}, \tag{1.18}$$

Combining Eq. (1.15) and Eq. (1.16) and defining $\gamma(s) = \frac{1+\alpha(s)^2}{\beta(s)}$ the following relation can be obtained:

$$\epsilon = \gamma(s)x^2(s) + 2\alpha(s)x(s)x'(s) + \beta(s)x'^2(s). \tag{1.19}$$

This equation defines an ellipse in the (x, x') phase space for each point s in the accelerator, as shown in Fig. 1.5. The particle positions in the phase space at a specific point of the accelerator ring moves around this ellipse according to the tune of the machine.

The parameter ϵ called emittance, defines the area of this ellipse, $\pi\epsilon$. From the optics point of view, in absence of additional influences like coupling between planes (Sec. 1.3.1) or acceleration, the emittance is a constant of motion around the accelerator. More details are given in Sec. 1.1.1.

The β-function defines the maximum deviation of the particle trajectory from the ideal one:

$$\hat{x} = \sqrt{\epsilon\beta(s)} \tag{1.20}$$

at any point in the accelerator, the so called beam envelope. This quantity determines the beam size at each point of the accelerator.

Using Eq. (1.8) and Eq. (1.19) an expression for the matrix transformation of $\alpha(s)$, $\beta(s)$ and $\gamma(s)$,

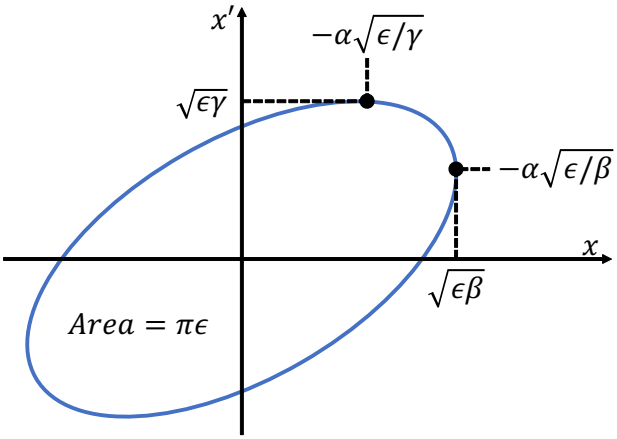

Figure 1.5: Illustration of the phase-space ellipse at an arbitrary point of the accelerator ring. Particle position in the phase space revolve moves the ellipse turn-by-turn according to the tune. The points of maximum beam size and maximum beam divergence are marked with their corresponding Twiss parameters.

called Twiss parameters, between any two points in the machine can be obtained:

$$\begin{pmatrix} \beta \\ \alpha \\ \gamma \end{pmatrix}_s = \begin{pmatrix} C^2 & -2SC & S^2 \\ -CC' & SC' + CS' & -SS' \\ C'^2 & -2S'C' & S'^2 \end{pmatrix} \begin{pmatrix} \beta \\ \alpha \\ \gamma \end{pmatrix}_0 \tag{1.21}$$

Here C and S are the independent solutions of the Hill's Equation introduced above. This matrix is called the transfer matrix of the Twiss parameters and is determined by the focusing properties of the magnetic lattice.

1.1.1 Beam emittance

The emittance describes the area of the phase spaces ellipse in the (x, x') or (y, y') coordinates space and it is typically expressed in $m \cdot rad$ units. It defines, together with the β-function, the beam size and beam slope. As far as the beam system is only affected by conservative forces, i.e. it has no way to interchange energy with its environment, the emittance is a constant of motion of the particles around the accelerator. However, there are certain effects that can effectively increase the emittance, for example mismatches between the optics in injection lines and the accelerator ring optics [7] or fast transitional changes in the optics of the machine [8].

Assuming the beam system is indeed conservative (a good approximation in a proton storage ring) the emittance cannot be reduced by optics means. Therefore, it is critical to reduce the effect of these emittance growth mechanisms in order to keep the beam sizes small. In Chapter 3 the impact of flux jumps, a type of field errors present in the new superconductor magnets used in the HL-LHC triplet, on the emittance will be studied.

Under acceleration though, it can be proven [9] that the emittance behaves as:

$$\epsilon \propto \frac{1}{\beta\gamma}, \tag{1.22}$$

if the relativistic factors β and γ change. This means that the emittance and therefore the beam size, shrinks during acceleration. As a consequence, at low energies the optics configurations must

have smaller maximum β-function value $\hat{\beta}$ for the beam to fit in the beam pipe aperture, whereas $\hat{\beta}$ can be increased after the beam has achieved higher energies. The normalised emittance is then defined as:

$$\epsilon_N = \epsilon\beta\gamma, \tag{1.23}$$

which is constant during acceleration. To distinguish these two quantities, the emittance defined in Eq. (1.19) is typically called geometric emittance, ϵ_{geom}.

1.2 Collider performance

In the previous section the basics of transversal beam dynamics were introduced. The type of accelerator described there is what is called a storage ring, i.e. a set of FODO cells whose only task is to keep the beam circulating for an indefinite time. The focus of this thesis is, however, on particle colliders which include special sections dedicated to make particle beams interact under controlled conditions.

The performance of particle colliders is typically measured by the two quantities, the total center of mass energy of particle collision and the number of particle interaction per unit of time they can achieve which is called luminosity.

Accelerators can produce particle collisions in two ways, either shooting the beam towards a static target or having two counter-rotating particle beams and making them to cross at particular locations. For two particles of mass m and the energy of the incident particle equal to E in a fixed target experiment the collision center of mass energy is $E_{coll} = \sqrt{2Emc^2}$ (assuming that $E \gg mc^2$) [10]. In a two beam collider of energy E per beam the achieved center of mass collision energy is $E_{coll} = 2E$. However, two beam particle colliders are typically much more complex to build as most of the accelerator lattice has to be duplicated in order to store and accelerate the two beams.

As the objective of building particle accelerators for high energy experiments is to produce collisions of particles in order to study certain physical phenomena under controlled conditions, the rate at which these physical processes happen is a crucial performance parameter of this type of machines. The physical process event rate can be written as [10]:

$$\frac{dR}{dt} = \sigma_p \mathcal{L}, \tag{1.24}$$

where $\frac{dR}{dt}$ is the number of events per unit of time, σ_p is the process cross-section to be explored and $\mathcal{L}$ is the accelerator luminosity.

For a collider with Gaussian shape profile of particle bunches the luminosity is given by:

$$\mathcal{L} = \frac{N_b f N_1 N_2}{4\pi\sigma_x\sigma_y} S \tag{1.25}$$

where N_1, N_2 are the number of particles in the first and second beam (the beams intensities), f is the beams revolution frequency, N_b is the number of bunches in the machine, σ_x, σ_y are the horizontal and vertical standard deviations of the bunch sizes at the Interaction Point (IP) considering identical bunch shapes in both beams and S is the luminosity reduction factor, which

depends on the way the beams cross.

Among the parameters of this equation, the beam sizes $\sigma_{x,y}$ have actually been defined in the previous section: these are the beam envelope sizes as defined in Eq. (1.20), $\sigma_{x,y} = \sqrt{\epsilon_{x,y}\beta^*_{x,y}}$. The β-function at the IPs, β^*, is an extremely important parameter of the machine optics and actually, different optics configurations are usually labelled according to the β^* they intend to achieve.

The β^* defines the performance of the accelerator from the optics point of view: the smaller the β^* is the more luminosity can be achieved. The downside of achieving small beam sizes is that they cause a large beam divergence. This can be understood by using the expression for the β-function in a drift space:

$$\beta(s) = \beta^* + \frac{s^2}{\beta^*}, \tag{1.26}$$

here the parameter s indicates the distance to the IP. As usually these interactions take place in the centre of very large particle detectors, there is no space near the IP to place quadrupoles to keep the β-function low. As it will be shown in the next section, because of this optics perturbation in those regions have a great impact on the global optics quality and therefore also on the safety of the machine.

To achieve a very small value of β^* at the IPs, the periodic lattice of the accelerator is interrupted and insertion regions are introduced. These insertions consist of a quadrupole triplet (or doublet) final focus system to squeeze the beam at the IP and a matching section that consists of several quadrupoles to match the periodic optics functions in the arcs to the required optics parameters at the entrance of the final focus quadrupoles section.

In Section 1.4 the lattice of the Large Hadron Collider and its experimental insertions are discussed in more detail.

1.3 Optics perturbations

In the previous sections the optics properties of an ideal circular accelerator have been discussed. However, the magnets the beam is put through are subjected to manufacture and installation tolerances and therefore the magnetic field they produce deviates from the design one.

As it will be shown in this section, measuring and correcting these imperfections is of crucial importance for the accelerators to operate according to their design performance and also safely.

Following the same way as in the previous sections, the first question to be asked is what happens if a bending dipole has an error in its magnetic field. Dipole errors drive the beam into a new closed orbit, $CO(s)$, different from the design one, which corresponds to $CO(s) = 0$. It can be shown that at each point s in the machine $CO(s)$ can be expressed as:

$$CO(s) = \frac{\sqrt{\beta(s)}}{2\sin(\pi Q)} \sum_i \sqrt{\beta_i}\theta_i \cos(\pi Q - |\psi(s) - \psi_i|) \ , \tag{1.27}$$

where the ith dipolar error is at a point at which the β-function is to β_i, giving an angular kick θ_i and with the phase advance between the ith dipole error and the point s given by $|\psi(s) - \psi_i|$. It should be noted that the absolute magnitude of this orbit perturbation is scaled with $1/\sin(\pi Q)$, which diverges when the tune of the machine approaches an integer number. A quadrupole placed

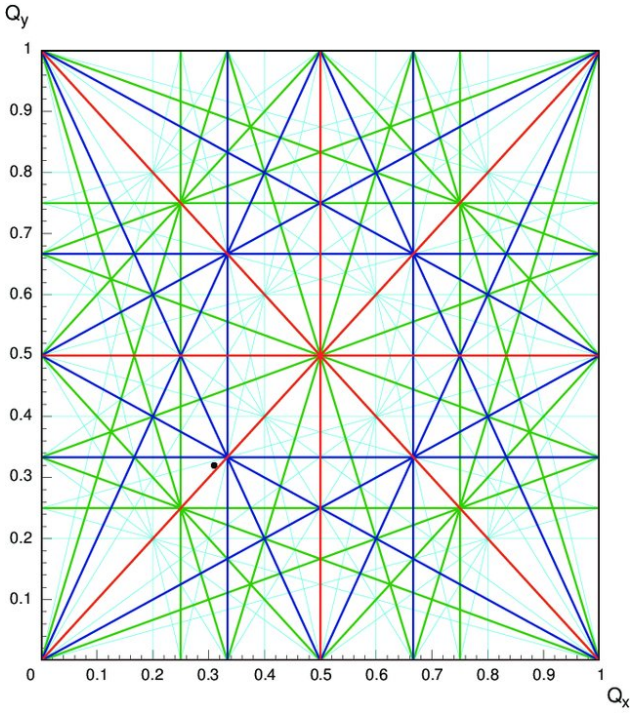

Figure 1.6: Tune diagram of the LHC [11], showing the resonance lines $nQ_x + mQ_y = N$ up to the fifth order. The black dot shows the operating point of the LHC.

with a transverse missalignment w.r.t. its design position in the machine acts as a correctly aligned quadrupole plus a dipole error at its position.

The most influential magnetic error, from an optics point of view, is an error in the magnetic field of quadrupole magnets. A single source of quadrupole error affects the tune of the machine as:

$$\Delta Q \approx \pm \frac{\beta_k \Delta k L}{4\pi} \tag{1.28}$$

where ΔkL is the integrated quadrupole strength of the error and β_k is the β-function at the position of the quadrupole error, with the sign being positive for the horizontal plane and negative for the vertical one. The quadrupole error also causes a deviation of the design β-function all around the machine as:

$$\frac{\Delta\beta}{\beta}(s) \approx \frac{\Delta k L \beta_k \cos(2\pi Q - 2|\psi(s) - \psi_k|)}{2\sin(2\pi Q)}, \tag{1.29}$$

where $\frac{\Delta\beta}{\beta}(s)$ is the relative deviation of the β-function w.r.t. its design value at the position s along the accelerator. This characteristics is called the β-beating and it is typically used as a the observable that determines the optics quality of the machine.

Similar to the formula in Eq (1.27), there is a global factor $\frac{1}{\sin(2\pi Q)}$ which describes an instablity for tunes close to half-integers driving the β-functions to infinity in the presence of quadrupole errors.

Similar instabilities also appear for higher order multipole magnetic errors. They happen when the tune is at the resonance frequencies satisfying $nQ_x + mQ_y = N$, and this situation should be avoided when choosing the tune of the machine. Fig 1.6 shows the resonances frequencies up to the 5th order with the operating point of the LHC marked in black.

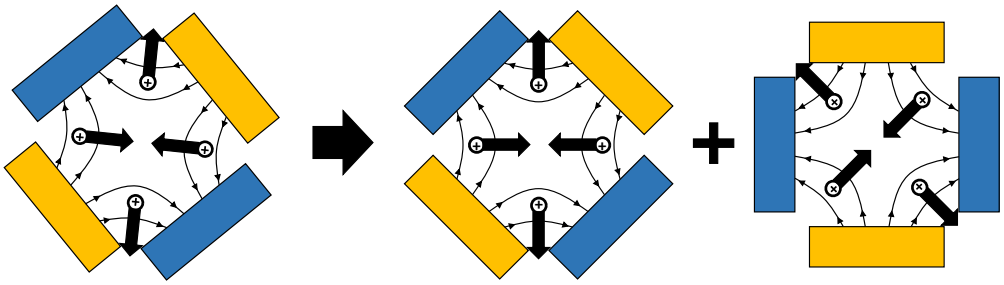

Figure 1.7: A quadrupole tilted along its longitudinal axis is equivalent to a combination of a straight up ideal quadrupole and a skew quadrupole.

1.3.1 Betatron coupling

Using the definitions for the transfer matrices Eq. (1.12) and Eq. (1.13) the transfer matrix for both planes across a horizontally focusing quadrupole can be written as

$$\begin{pmatrix} x \\ x' \\ y \\ y' \end{pmatrix}_1 = \begin{pmatrix} M_{foc} & 0 \\ 0 & M_{def} \end{pmatrix} \begin{pmatrix} x \\ x' \\ y \\ y' \end{pmatrix}_0 \tag{1.30}$$

From this it can be concluded that the motion of the particle across the quadrupole is totally independent in the x and y directions. This makes sense, as we defined the forces exerted by the quadrupoles in each direction to be proportional to the displacement in that direction only (see Eq. (1.4)):

$$F_x = -evgx, F_y = evgy. \tag{1.31}$$

This is only true in the ideal case though. If a quadrupole is installed with a slight tilt along its longitudinal axis (Fig 1.7), the particle crossing the quadrupole will feel a force in the x-direction that is proportional to its y-displacement (and the other way around). Then the motion in both planes becomes coupled.

This betatron coupling between the planes makes the horizontal and vertical tunes impossible to approach below a threshold typically named ΔQ_{min} [12], which measures how strong this $x - y$ coupling is. Coupling can drive the tunes into dangerous values close to resonances.

1.3.2 Beam momentum deviation

In the analysis done previously, it was assumed that all the particles in the beam have the same momentum. This is not true in a real machine as the beam has a non-zero longitudinal size and therefore the particles in the radio-frequency system are accelerated slightly differently. The deviation of a particle momentum relative to its design value is denoted as $\frac{\Delta p}{p}$.

This momentum deviation changes the ideal closed orbit of the particle $x_\beta(s)$ to $x(s) = x_\beta(s) + x_D(s)$ where:

$$x_D(s) = D(s)\frac{\Delta p}{p}. \tag{1.32}$$

Here $D(s)$ is the dispersion function which is another function determined by the focusing properties of the accelerator. The dispersion function can alter the orbit at the IPs significantly and therefore

the optics of the machine has to be configured in such a way as to suppress it. Usually this is achieved by adding a set of quadrupoles, called dispersion suppression section, to the matching section with the aim to cancel the dispersion at the Interaction Region (IR).

The relative momentum deviation $\frac{\Delta p}{p}$ also alters the strength of the focusing forces produced by the quadrupoles. Particles with larger momentum receive a smaller push than those with lower momentum. This is analogous to the optics where light beams of different wave lengths (momentum of photons) are focused differently by a lens , this effect is called chromaticity. The $\frac{\Delta p}{p}$ also causes a change of the tune ΔQ in accordance with Eq. (1.28). The chromaticity of the machine is then defined as [13]:

$$Q' = \frac{\Delta Q}{\Delta p/p} \rightarrow Q' = -\frac{1}{4\pi} \oint k(s)\beta(s)ds \tag{1.33}$$

As each of the particles in the beam have a slightly different $\frac{\Delta p}{p}$, the tune of a machine has a certain spread so that the operating point at the resonance diagram of Fig. (1.6) has a non-zero size. If the spread is too large, a large fraction of the particles in the beam will hit resonances and get lost.

The chromaticity is controlled by using sextupole magnets, which exhibit a controllable momentum dependent focusing when placed in dispersive locations. A sextupole magnet placed with a transverse missalignment, or traversed by the beam off-centre, acts as a sextupole plus a quadrupole whose strength is related to the strength of the sextupole and the magnitude of the missalignment. This feature will be used in Sec. 2.7 to correct quadrupole errors in at locations where no quadrupole correctors are available.

1.4 LHC accelerator complex and the HL-LHC

In the previous sections the basics of the transverse beam dynamics of circular accelerators have been introduced in a general accelerator-independent form, in the rest of the Introduction will be devoted to the Large Hadron Collider (LHC) and its High Luminosity Upgrade (HL–LHC) as the present thesis is focused on this machine.

The LHC, situated at the French-Swiss border near Geneva in Switzerland is the world largest particle accelerator, with a total circumference of about 27 km. It is part of the CERN's Accelerator Complex (Fig. 1.8), a chain of particle accelerators that progressively accelerate protons (and heavy ions) up to a 14 TeV centre-of-mass energy.

Specifically, a series of proton bunches is injected into the LHC from the Super-Proton-Synchrotron, at an energy of 450 GeV into two counter-rotating beam pipes. The beams are then accelerated by the LHC to up to 7 TeV per beam energy and cross at 4 IPs, colliding the proton bunches at centre of mass energy of up to 14 TeV.

The LHC contains two beam pipes to store, accelerate and collide the beams: Beam 1 (rotating clockwise) and Beam 2 (rotating counter-clockwise). The machine is divided in 8 sectors, each of them is composed of an arc (bending) section and a special purpose straight section (Fig. 1.9). In four of these straight sections the two beam pipes merge and the beams cross at interaction points surrounded by general purpose detectors of the ATLAS [14] and CMS [15] experiments at points 1 and 5, of ALICE [16], an experiment dedicated to the study of heavy ion collisions at point 2, and LHCb [17], an experiment intended to perform precise measurements of the CP violation and

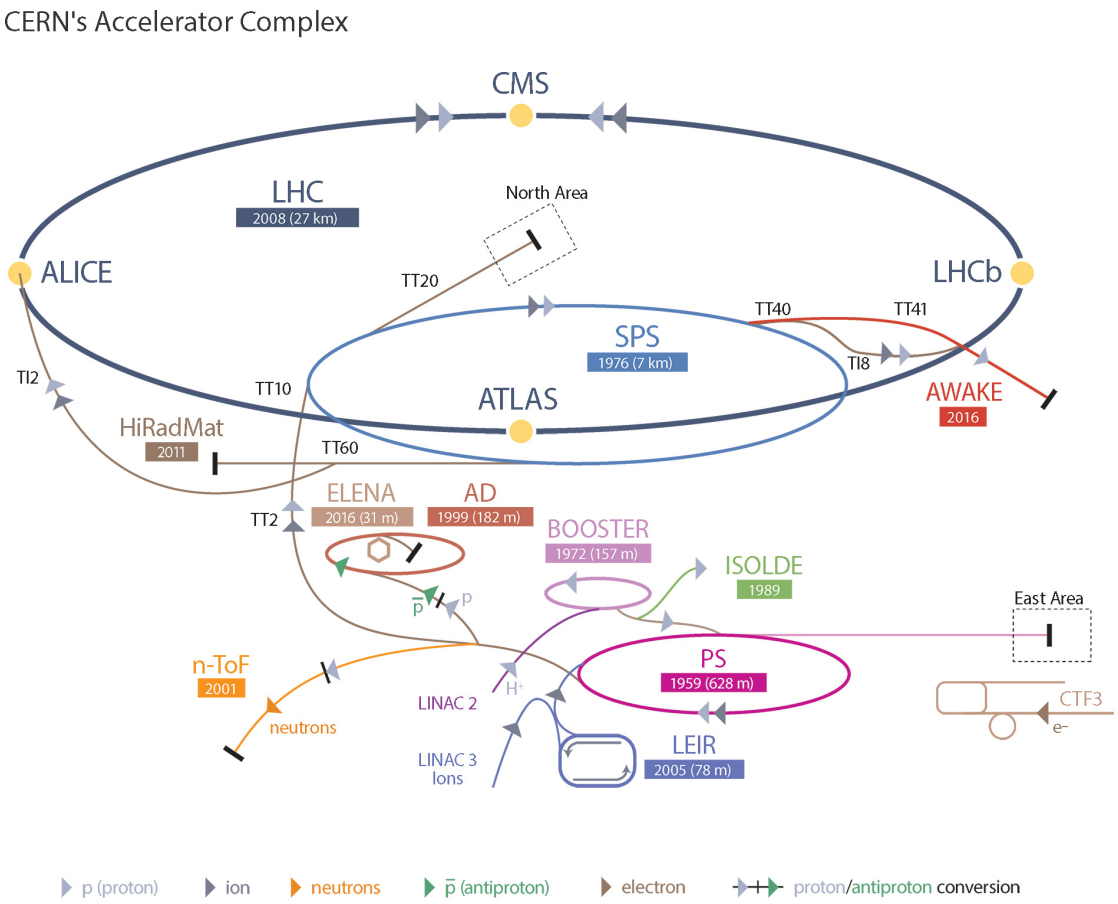

Figure 1.8: The CERN's Accelerator Complex. For the typical operation of the LHC a proton beam is produced by LINAC 2 and follows the chain: LINAC 2 → BOOSTER → PS → SPS → LHC.

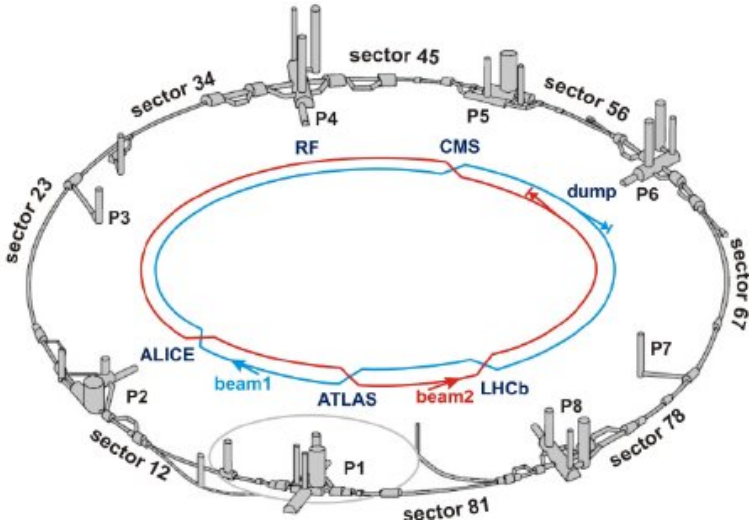

Figure 1.9: Schematic of the layout of the LHC showing its different sectors and experiments. Each of the 8 sectors are named after they limiting points, e.g. the sector between point 1 and point 2 is named sector 12.

B hadrons decays at point 8.

Each of the LHC arcs are 2.45 km long, having a total of 153 bending dipoles and 23 106.9 m long FODO cells. The quadrupoles in the FODO cells are powered by two power supplies only, one for the focusing quadrupoles and one for the defocusing ones and therefore can only be trimmed in groups.

The straight sections have a more heterogeneous architecture as their purpose differ heavily. In general they are composed of a matching section (containing the dispersion suppressor mentioned in Sec. 1.3.2) to accommodate the beam optics to the specific purpose of the section plus the specific equipment. The straight sections containing the IPs are composed of 16 matching section quadrupoles and a final focus triplet system composed of 8 quadrupoles. In general, the quadrupoles in the matching sections are individually powered and therefore can be trimmed individually.

Figure 1.10 shows the β-function in sector 5 at injection optics and optics squeezed to 30 cm β^*. The injection optics on the top plot have a very low β-function to accommodate for the larger beam sizes at injection. After the beams are accelerated, the beam size at the IP is reduced by strongly focusing the beam. This increases the β-function in the triplet region to several kilometres (and therefore the beam size) making the aperture of the triplet the main limiting factor to reach smaller β^*. Moreover, this very large β-function enhances greatly the magnetic errors in the triplet area, as it was explained in Section 1.3, making the optics corrections in this region of critical importance. The optics corrections in this regions will be addressed in Sec. 1.7.

After Run 3 of the LHC, there is little reason to keep running the LHC at its current luminosity output as it would take 10 years to halve the statistical error of a given measurement of the main experiments. This motivated the High-Luminosity LHC (HL-LHC) project [18], which aims to increase the integrated luminosity of the LHC by a factor of 10 and which is planned to be in operation by 2027.

Equation (1.25) defines the luminosity output of a particle collider and HL-LHC aims to improve

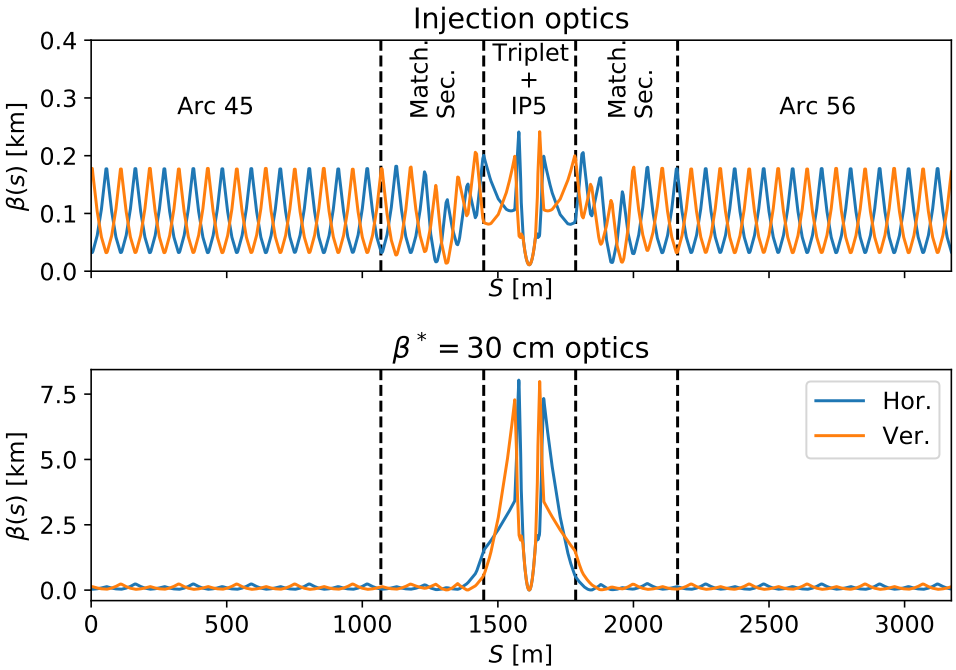

Figure 1.10: β-function of the LHC around IP5 at injection optics (Top) and an optics configuration to squeeze the β^* to 30 cm. Notice the different scale in the vertical axis. The matching section marked in the plot includes the dispersion suppressor.

Parameter	LHC	HL-LHC
N_b [10^{11}]	1.15	2.2
N_1 and N_2	2808	2748
Minimum β^* [m]	0.55	0.15
ϵ_n [μm]	3.75	2.5

Table 1.1: Comparison of the LHC and the HL-LHC parameters that affect the luminosity [18].

a number of the parameters in this formula. A comparison of some of the parameters of the HL-LHC with those of the LHC is given in Table 1.1. It should be noted though that many of these parameters have been already improved in the current LHC configuration.

The injection chain of the LHC has also undergone several improvements in the frame of the LHC Injector Upgrade (LIU) that will allow a large increase in the beams intensity in the HL-LHC, keeping the emittance at low values. The increase on the beams intensity will also require an extensive upgrade of the collimation system. More information on these upgrades can be found in [19].

1.4.1 The new quadrupole triplet of the HL-LHC

To achieve the reduction of the minimum β^* down to the value given in Table 1.1, the current LHC final focus quadrupole triplet is not suitable anymore as its aperture would be too small to accommodate the beam size at points where the maximum β-function in the ring has values of about 40 km in certain configurations of the optics.

Therefore, one of the main upgrades of the HL-LHC is its new quadrupole triplet. The new system is going to be installed at the IRs 1 and 5 and is composed of 6 quadrupoles per side of the IP

(instead of 4 per side in the LHC). These quadruples will also have a larger aperture of 150 mm (instead of 70 mm in the LHC) and will be longer. As the new quadrupoles have a larger aperture they have to produce a stronger magnetic field in order to maintain the same gradient as the quadrupoles of the old LHC triplet.

The NbTi technology used in the LHC superconducting magnets cannot reach the necessary field strengths and therefore will be replaced by the Nb_3Sn technology which can produce magnetic fields up to 50% stronger than the NbTi one. However, superconductors of these type exhibit the so called flux jumps that disturb the magnetic field produced by the magnet. A study of the effect of the flux jumps on the beam is one of the main results of this thesis and its results are presented in Chapter 3.

1.4.2 The ATS optics scheme

When pushing β^* to smaller values and therefore $\hat{\beta}$ to higher ones, a new challenge arises which is compensation of the chromatic effects produced by the triplet quadrupoles (Eq. (1.33)).

As the beam size gets smaller when the beam reaches its full energy, an aperture margin that allows to increase the β-function appears in the arcs. The Achromatic Telescopic Squeeze (ATS) optics scheme [20] modifies the matching sections around the main IPs to send a β-beating wave down the arcs. This wave makes the β-function peak at the sextupoles in the those arcs, enhancing their strength.

This optics scheme has been extensively tested at the LHC [21] and has become the operational optics scheme in Run II. In HL-LHC this will also be the operational optics scheme, but as the minimum β^* is planned to be smaller, the ATS enhanced arcs will get even larger β-functions. This has the collateral effect of enhancing local errors in the arcs also which will be studied in Section 2.7, as well as a successful technique to correct them.

1.5 The FCC-hh

The hadron-hadron Future Circular Collider (FCC) [22] is a project to build a circular hadron collider of about 100 km long circumference (Fig. 1.11) with a centre of mass energy of 100 TeV that has recently passed its conceptual design phase.

This accelerator will be a part of the CERN accelerator complex and the current LHC will become its injector. Being heavily based in the LHC, it will also have 4 interactions points and its optics configuration will be very similar to that of the LHC. This project requires the new superconductor technology mentioned in Section 1.4.1 in all of its main dipoles and quadrupoles. Therefore, the effect of flux jump in the FCC-hh can be critical and will be studied in Chapter 3.

1.6 Global optics measurements and corrections in the LHC

It was shown in section 1.3 how magnetic errors can alter the design optics in the way that can be dangerous for the machine performance and safety. Measuring and correcting these optics errors is therefore of critical importance.

From the point of view of optics corrections, the LHC has two significantly different areas:

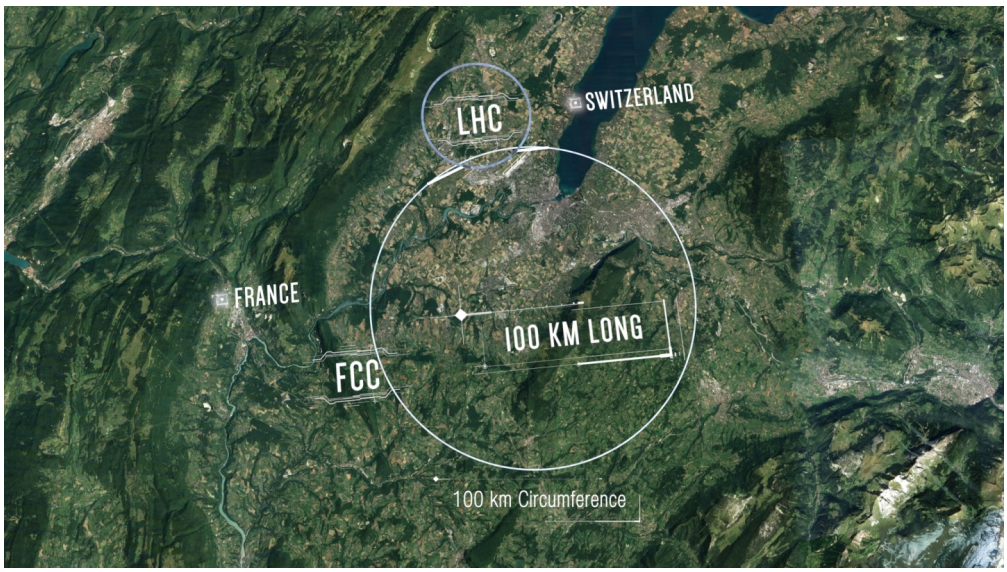

Figure 1.11: Schematic view of the future location of the FCC.

- The regions around the IPs with very large β-functions (at least in squeezed optics) which makes the optics errors to have very strong influence, but also where the quadrupoles are mostly individually powered, thus allowing for many degrees of freedom to find corrections for specific quadrupoles. This corrections are typically called local corrections and are implemented first, because most of the β-beating in the machine usually arises in these regions.
- The arcs and matching sections far from the IPs, where the β-function is typically much lower and the quadrupoles are mostly powered in large series. The corrections performed in these regions, called global corrections, aim to reduce the overall β-beating of the machine without addressing specific magnetic errors.

The way the optics corrections are performed in the LHC is explained in Sec. 1.7 for the local corrections and Sec. 1.6.2 for the global corrections.

1.6.1 Optics measurements in the LHC

To measure the optics parameters of the machine the main diagnostic device is the Beam Position Monitor (BPM). These monitors record the position of the beam as it passes through them turn-by-turn and therefore they can measure the betatron oscillations of the beam from which the optics parameters can be extracted. There are over 500 BPMs in the LHC per plane and per beam distributed around the machine.

However, LHC proper betatron oscillations of the beam are too small to be measured in the LHC. The beam therefore has to be excited using kicker dipoles in order to increase the amplitude of the oscillations. Historically such excitations have been performed in two ways, either using a fast single kick or an Alternating Current Dipole (AC-dipole).

The single kick excitation is the simplest, as it provides a fast dipolar kick rapidly displacing the beam into larger amplitudes. However, the beam naturally decoheres very rapidly (depending on the machine non-linear errors) and therefore its effective emittance and thus beam size grow, that requires to inject a new beam into the machine for each excitation, which makes this method slow

and impractical for its use at high energies.

The AC-dipole excites the beam by slowly ramping up an oscillating current dipole at a frequency close to the natural tune of the betatron oscillations. It stays at a fixed amplitude for many thousand turns, and then ramps down slowly. If the ramping up and down processes are done slowly enough, the beam emittance does not grow significantly [8]. This allows for many measurements to be performed sequentially and therefore this is the way the optics measurements are performed in the LHC.

The turn-by-turn BPM records then undergo a noise cleaning process, namely a Singular Value Decomposition (SVD) is applied to the matrix formed by all the data samples of all BPMs and only the largest few SVD modes are kept. This removes the uncorrelated signals of the BPMs which are associated mainly to the noise.

A specific harmonic analysis [23, 24] is then applied to the cleaned BPM signals from which different oscillations modes can be extracted.

The spectral line of the harmonic analysis that corresponds to the machine tune frequency contains the information of the betatron oscillations in its Fourier coefficient. For the ith BPM the complex Fourier coefficient at the tune frequency is given by

$$X_i = A_i \mathrm{e}^{i\phi_i}, \tag{1.34}$$

where A_i is the amplitude of this line and ϕ_i the phase of the line.

The β-function can be obtained at any BPM from this coefficient by using two main methods: β from phase and β from amplitude technique.

The β-function from the amplitude of the betatron oscillations is the most intuitive and simple among the β-function measurement techniques. Eq. (1.20) gives a relation between the amplitude of the betatron oscillations and the β-function. Denoting β_i the β-function at the ith BPM and $J = \epsilon/2$, called action, related to the strength of the AC-dipole kick, the following formula can be obtained:

$$A_i = \sqrt{2J\beta_i} \rightarrow \beta_i = \frac{A_i^2}{2J} \tag{1.35}$$

which gives a direct relation between the tune line amplitude and the β-function. If the AC-dipole is used to excite the beam, this is actually the "forced" β-function result of the excitation and it must be compensated to obtain the natural β-function [25]. The main problem with this method is that in the LHC the calibration of the BPMs is generally unknown, which amounts to an unknown calibration factor C_i in this relation,

$$\beta_i = \frac{A_i^2}{2JC_i^2} \tag{1.36}$$

In the absence of further knowledge of these factors for each BPM, this method shows a bias that makes it unpractical for corrections in the LHC. In the last few years though there has been a big effort to measure these factors in certain critical BPMs. A much more detailed description of this method and the measurement of the calibration factors can be found in [25, 26].

The β from phase technique uses, instead, the phase advance of the betatron oscillations to compute

the β-functions. The relation between the β-function and the phase advance between a set of any 3 BPMs (contiguous or not) is given by [27]:

$$\beta_i = \frac{\epsilon_{ijk}\cot\phi_{i,j} + \epsilon_{ikj}\cot\phi_{i,k}}{\epsilon_{ijk}\frac{M11(i,j)}{M12(i,j)} + \epsilon_{ikj}\frac{M11(i,k)}{M12(i,k)}} \tag{1.37}$$

where β_i is the β-function at the ith BPM, ϵ_{ijk} is the Levi-Civita tensor, $\phi_{nm} = \phi_m - \phi_n$ is the phase advance between the nth and the mth BPMs and $M11(i,j)$ and $M12(i,j)$ the (1, 1) and (1, 2) elements of the ideal phase space coordinates transfer matrix between the ith and the jth BPMs. This equation gives a relation between the turn-by-turn data, from which the tune line phase advance can be extracted, and the β-function. Once again, if the AC-dipole is used, this forced β function has to be processed in order to obtain the natural β-function [28].

Equation (1.37) though, is not sensitive to BPM calibration as the β from amplitude technique does. The cotangent function in the numerator is one of the drawbacks of the method: it diverges when the phase advance between one of the pairs of BPMs approaches $n\pi$.

Historically this method has been applied to contiguous triplets of BPMs (3-BPMs method), however, in the last few years, it has been proven that using several combinations of BPMs improves the precision and the knowledge of the uncertainties of the method significantly. Deeper description of this technique and its advancements can be found in [27, 29, 30].

This method requires a precise measurement of the phase advance between BPMs. From Eq. (1.17) it can be seen that the magnitude of the phase advance is roughly inversely proportional to the magnitude of the β-function. In the LHC interaction regions the β-function can reach values of tens of kilometres which makes the precision of the measurement of the phase advance in the region to be very poor. In Sec. 1.7 the techniques used to overcome this limitation will be described.

As the limitations of the phase advance method explained above affect only certain specific regions of the accelerator, it is the technique used to measure the β-function and assess the global optics quality in the LHC.

1.6.2 Global optics corrections in the LHC

Global optics corrections in the LHC are performed by correcting globally the betatron phase and dispersion using a response matrix [31].

The measured phase-advances of the betatron oscillations is used instead of the actual β from phase as it is independent of the BPM calibration and also independent of the ideal model of the machine.

Before the corrections are computed, it is of critical importance to clean any possible measurement artefact coming from faulty BPM measurements. The SVD denoising method described before also acts as a faulty BPM cleaning technique because it removes over-dominant spatial vectors from the SVD decomposition. This is not sufficient though, and the BPMs spectral results are also analysed and manually or automatically cleaned. Machine learning techniques have been used in the last few years to perform this automatic faulty BPM detection with great success [32, 33].

Then the task at hand is to compute and invert a matrix R_{resp} in the relation

$$\begin{pmatrix} \Delta\vec{\phi}_x \\ \Delta\vec{\phi}_y \\ \Delta\vec{ND}_x \\ \Delta Q_x \\ \Delta Q_y \end{pmatrix} = R_{resp} \times \begin{pmatrix} \Delta k_1 \\ \Delta k_2 \\ . \\ . \\ . \end{pmatrix} \tag{1.38}$$

where $\Delta\vec{\phi}_{x,y}$ are the horizontal and vertical phase advance deviations at every BPM, $\Delta\vec{ND}_x$ is the normalised horizontal dispersion ($ND(s) = D(s)/\beta(s)$) at every BPM, $\Delta Q_{x,y}$ are the horizontal and vertical tunes that are included so that they are kept constant by the correction and Δk_i are the variation of the strength of the knobs (combinations of quadrupoles) that are going to be used for correction.

The R_{resp} matrix is computed using a model of the LHC simulated with MAD-X [34] by changing the strength of each knob individually and recording the optics response. Then this matrix is inverted and applied to the measured optics to obtain a set of corrections:

$$\begin{pmatrix} \Delta k_1 \\ \Delta k_2 \\ . \\ . \\ . \end{pmatrix} = R^{-1}_{resp} \times \begin{pmatrix} \Delta\vec{\phi}_x \\ \Delta\vec{\phi}_y \\ \Delta\vec{ND}_x \\ \Delta Q_x \\ \Delta Q_y \end{pmatrix}_{meas} \tag{1.39}$$

This provides a set of knobs that can be applied to the measurement data directly.

1.6.3 Coupling corrections in the LHC

As it was described in Section 1.3.1 the betatron coupling between the two transverse planes can be dangerous for the machine stability and therefore must be corrected.

The coupling produces a minimum distance between horizontal and vertical tunes ΔQ_{min}. The most direct method of measuring this betatron coupling is to use a quadrupole adjustment to change the horizontal and vertical tunes towards the same value and observing this minimum distance. This gives a direct indication of the global coupling in the machine but does not give any indication of the location of individual sources of coupling. ΔQ_{min} is related to the strength of the coupling sources in the machine by the formula:

$$\Delta Q_{min} = \left| \frac{1}{2\pi} \int_0^L ds \sqrt{\beta_x \beta_y} k_s e^{i(\phi_x - \phi_y - 2\pi\Delta s/L)} \right|, \tag{1.40}$$

where k_s is the strength of the skew quadrupole force and Δ is the difference between the horizontal and vertical tunes. Betatron coupling exhibits a similar behaviour to the normal optics errors, as the strength of a coupling source depends on the β-functions at the position of the source. Therefore, coupling is also corrected locally close the IPs, and globally in the LHC arcs.

To find local sources of coupling the turn-by-turn data analysis of the previous section can also be used. As the betatron coupling manifests itself as a leakage of the quadrupolar forces of one

plane into the other, in the turn-by-turn data harmonic analysis of one of the planes this effect will appear as a Fourier coefficient at the tune frequency of the other plane. The relation between the magnitude of this secondary line and the main tune line can be used to compute the so called f_{1001} Resonance Driving Term (RDT) [35], a complex number whose magnitude stays constant in absence of coupling sources but exhibits abrupt jumps when these sources appear [36]. The f_{1001} RDT is related to the ΔQ_{min} by the formula [37]:

$$\Delta Q_{min} = \left| \frac{4\Delta}{2\pi r} \oint ds f_{1001} e^{-i(\phi_x - \phi_y) + is\Delta/r} \right|, \tag{1.41}$$

where r is the radius of the machine. In practice the integral is evaluated at the position of the BPMs only.

The betatron coupling is corrected by using purposely placed skew quadrupoles, that is, quadrupoles that are tilted by 45 degrees w.r.t. a normal focusing quadrupole and therefore are coupling sources used to counteract the effect of the unwanted ones.

The same approach as in the previous section can be used to correct the global coupling by using a response matrix over the real and imaginary parts of the f_{1001} RDT to compute the necessary strength of the skew quadrupoles in the arcs. This is, once again, an effective correction whose goal is to reduce the global coupling of the machine without addressing local sources individually.

1.7 Local optics Corrections in the LHC

The correction of the optics error sources in the triplet regions is of critical importance, as the β-functions in these regions can reach several km, enhancing said errors and making the machine unsafe to operate.

As different optics configurations change extensively the β-functions, increasing it in some locations and reducing it in others, different configurations enhance a different set of local errors and therefore the corrections have to be computed, or at least checked, for every target β^*. Specifically, the optics corrections are typically very different at injection optics as compared to the squeezed optics, but once computed for given configurations the corrections usually stay stable over years, though they can change as a result of change of the beam energy, after long shutdowns or change of configurations, or even for other yet unclear reasons as happened in the 2015 commissioning [38]. Therefore the optics corrections are checked yearly, after every shutdown.

The general procedure to find and correct local errors is as follows: Two beams are injected in the LHC consisting of one low intensity bunch per beam. These low intensity bunches called "probes" are used to perform corrections and experiments that would be dangerous for the machine with full physics beams. The probes are then ramped up to the required energy and the optics is set to the target β^*. The machine optics is then measured using the procedure described in Sec. 1.6.1.

The technique used to isolate and measure local errors in certain parts of the machine is called Segment-by-segment [31, 39]. This technique isolates regions (segments) of the accelerator that are likely to contain strong local error sources.

A model containing the design optics of this segment, generated using MAD-X [34], is extracted from the full accelerator model and treated like an individual beam line. The measured optics at

the starting BPM are used as initial conditions of the segment model, so that all errors coming from outside of the segment to be neglected. These segments are usually the areas around the IPs but, to obtain a precise local model, it must be ensured that the optics measurement in the initial BPM of the segment have a good precision. Therefore it is common to take the starting point in the dispersion suppressors where the β-function is smaller.

To the optics parameters measured on each BPM inside the segment an uncertainty is assigned. It depends on both the optics measurement uncertainty at that BPM itself and a propagation of the error from the initial point BPM of the segment, as the precision of the local model depends on this measurement. Results of a recent progress on the evaluation of these uncertainties can be found in [40].

The optics parameters measured across the segment can then be compared with the local model of the segment to obtain the deviations of the different optics parameters caused by errors in the region.

An effective model of the measured local optics can be found by matching the measured deviations w.r.t. the reference local model using a second model. The values of the variables of this second model are varied until it reproduces the measurement as closely as possible. As this model is configured to mimic the local optics deviations pattern in the segment, i.e. its an effective model of the segment, it can be used to compute corrections by just flipping the sign of the variables used to match these measured optics deviations.

As the direction in which the segments are traversed is arbitrary (in fact Beam 1 and 2 traverse them in opposite directions), the final BPM of the segment can be used as the initial one and the other way around. This provides a new set of local deviations in the segment called "back propagation", that are different from the "forward propagation", as the optics errors in the segment are in general not symmetric under the inversion of direction. This new set of deviations can be used to provide more constraints when generating the effective model.

1.7.1 Local phase correction

As it was described in Sec. 1.6.1, the phase advance can be used to measure the optics of the machine and this approach is BPM calibration and model independent. Historically this has been the observable used to find and correct local errors with great success. The first successful use of this technique took place in 2010 where a 1% error in the main warm quadrupoles in IR3 and IR7 was found [41]. Moreover, in 2012 a cable swap that caused a 100% β-beating was found using this technique [42].

Figure 1.12 shows an example of the Segment-by-segment technique applied to a segment of about 1 km around IP2 (from a measurement in an ion run) at $\beta^* = 50$ cm optics. The blue line shows the measured phase deviations w.r.t. the local model starting at $s = 0$. The plot demonstrates how in the region of the actual sources of errors, namely the triplet regions marked in grey, the phase measurement lies below the error bar of the measurement. The effect of the local error in the triplet is only visible downstream, where the β-functions are much smaller and therefore the relative uncertainty of the phase is much better.

The orange line on Fig. 1.12 shows an effective model of the errors in the segment. The change of

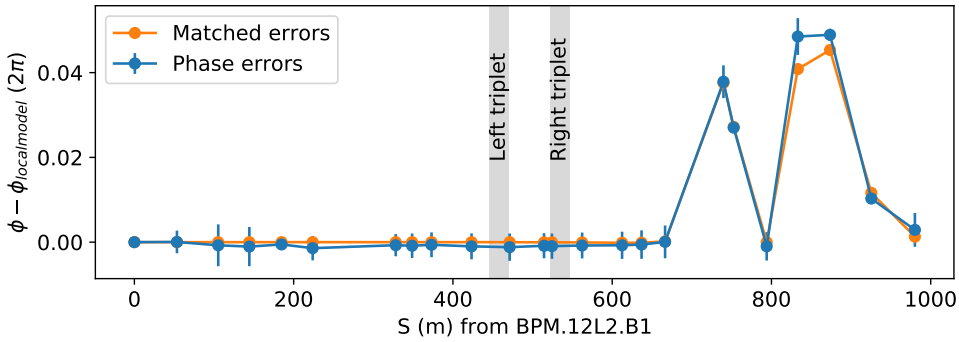

Figure 1.12: Example of a local phase match to compute local errors. The blue line shows the measured local phase deviation from the model of the segment. The orange line is a simulated set of trims that matches the measured deviations.

the strengths of the quadrupoles found to generate this effective model can be used as corrections by flipping their sign, which would cancel out the phase deviations.

As the quadrupoles of the triplet are shared by the two beams, the matching of the effective model has to be performed simultaneously for the phase deviation of both planes on both beams, i.e. for four data sets like the one plotted in Fig. 1.12.

1.7.2 β^* measurements and corrections

During the optics commissioning of 2015, a loss in luminosity of about 5% was found even after seemingly successful local phase corrections in the main IRs. Later it was found that this was due to a shift of the beam waist, i.e. the point with the minimum β-function close to the IP was not centred in the IP itself [38]. This not only spoils the performance of the accelerator by reducing the delivered luminosity, it also produces a luminosity imbalance between ATLAS and CMS which causes that one of the experiments records more events than the other.

Figure 1.13 shows an example of such waist displacement. In an optics drift, the β-function describes a parabola given by Eq. (1.26), the blue line shows the behaviour of an ideal β-function across the IP drift, where the minimum of the β-function is at the IP, the position of the beam waist. The green line however, has a waist that is away from the IP, which causes the β^* to be larger at the IP itself, producing a larger beam size at the IP and therefore lowering the luminosity.

In Sec. 2.5 it will be demonstrated that the phase advance is sensitive to the minimum of the β-function, but it is blind to the actual waist location. The local optics corrections using the phase advance were therefore ineffective against this beam waist displacements.

For larger β^* the parabola in Fig. 1.13 is wider and therefore a small displacement of the waist is not that prominent. However for smaller β^*, this parabola becomes very sharp and therefore a small waist displacement has a very large impact on the luminosity. In fact, in the most recent runs of the LHC and the future HL-LHC the waist displacements are the main cause of loss of luminosity if not properly corrected.

To address this issue, the Segment-by-segment technique described before can be enhanced by including additional measurements of the optics functions around the IP. This can be, equivalently, the β-functions in the quadrupoles or BPMs closest to the IPs or the value of the β^* and the waist

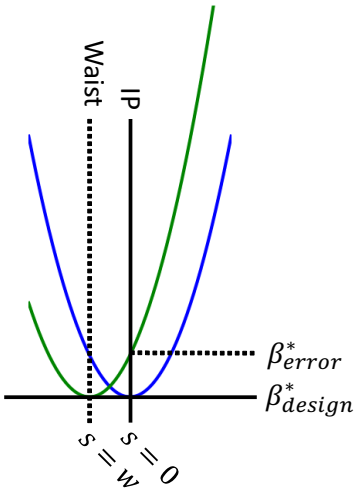

Figure 1.13: Plot of the parabolic behaviour of the β-function in the IP. The curve in blue is the ideal β-function with the position of its minimum at the IP, $\beta(IP) = \beta^*_{ideal}$. The curve in green is the β-function parabola affected by optics errors causing the minimum of β to be displaced to a non-zero waist position $w \neq 0$. In the latter case $\beta^* = \beta^*_{error}$ is larger than the design one.

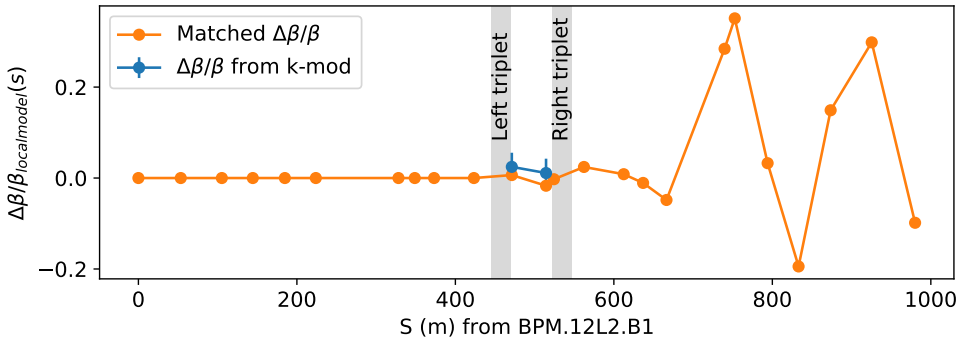

Figure 1.14: Example of the use of a K-modulation measurement matching to correct waist displacements. The blue line shows the β-beating measurements of K-modulation w.r.t. the local model of the segment. The orange line shows a simulated set of trims that matches the measured deviation.

displacement. This adds new constraints to the effective model matching problem, at least 8 per IP (horizontal and vertical, β^* and waist of Beam 1 and 2), of a different nature than the phase advance, that makes the manual matching to become a very difficult task. An automatic matching routine will be presented in Sec. 2.1 that can import these new constraints and find a solution that satisfies the phase advance deviation and β^* constraints automatically.

In recent runs of the LHC, K-modulation (described in the next section) has been the tool used to provide this information accurately, however it does not seem to be precise enough for HL-LHC (Sec. 2.4). Figure 1.14 shows the Segment-by-segment technique applied to the measurement of the β-function from K-modulations in the BPMs closest to the IP. The blue line shows the β-beating w.r.t. the local model of the segment of the K-modulation measurement. The orange line shows the matched β-beating of the model computed to serve as effective model.

The β from the amplitude method described in Sec. 1.6.1 is another candidate to give precise β-functions in this region where the phase advance measurement is not useful. However, as it was explained, they are affected by the BPM calibration factors which are in principle unknown even though there have been recent advancements in measuring these factors in the IRs [25, 26].

The phase advance from DOROS BPMs to measure the β-function at the waist and luminosity scans to measure the waist position are other two techniques proposed as alternatives to the K-modulation at HL-LHC, they will be described in Sec. 2.5 and Sec. 2.6.

1.7.3 K-modulation

During Run 2 of the LHC, the main technique used to measure and correct β^* has been the K-modulation. This technique consists in changing the strength of individual quadrupoles and recording the tune response to this change. The relation between the change in strength of the quadrupole and the tune response is proportional to the average β-function across the quadrupole ($\beta_{AV_{x,y}}$) [4]:

$$\begin{aligned} \beta_{AV_{x,y}} &= \pm \left[\cot\left(2\pi Q_{x,y}\right)\left(1-\cos\left(2\pi\Delta Q_{x,y}\right)\right)+\sin\left(2\pi\Delta Q_{x,y}\right)\right]\frac{2}{\Delta k L} \\ &\approx \pm 4\pi\frac{\Delta Q_{x,y}}{\Delta k L}, \end{aligned} \tag{1.42}$$

where ΔK is the strength change of the quadrupole, L its length and $\Delta Q_{x,y}$ the induced change of tune in the machine.

Specifically, in the LHC, the most prominent use of this technique has been the modulation of quadrupoles closest to the IP in order to obtain a precise measurement of their $\beta_{AV_{x,y}}$ and propagate it to the IP, obtaining the β^* [43].

The exact procedure in the LHC begins with the modulation of the quadrupole from which the tunes and strength change are recorded. Figure 1.15 shows one of the K-modulations performed in the first quadrupole of the left side of IP1. The top plot shows the modulation function running over time in the current of the quadrupole, it is a sinusoidal function that allows to scan smoothly all the available space before the horizontal and vertical tunes approach too much and hit the coupling resonance. The bottom plot shows the response of the tunes in Beam 1. As this quadrupole is

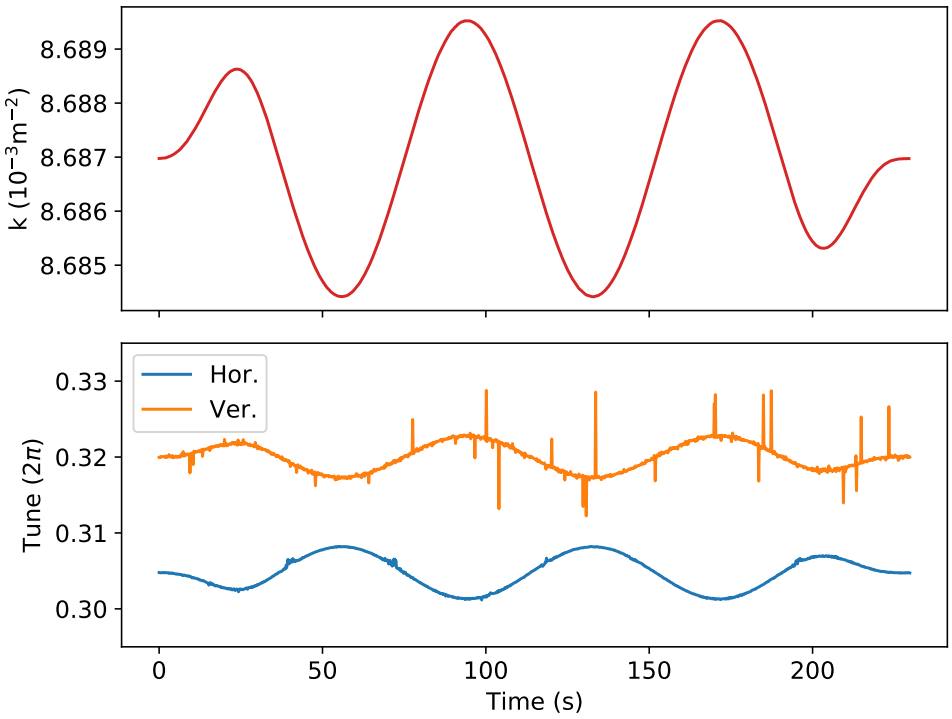

Figure 1.15: Example of a K-modulation of the first quadrupole of the left of IP1. On the top plot the change on the strength of the quadrupole is shown. The bottom plot shows the response of the horizontal and vertical tunes of Beam 1.

shared by Beam 1 and 2, the tunes of Beam 2 also change.

After having performed the modulation, the four relations between the quadrupole strength k and $Q_{x,y}$ of Beams 1 and 2 are accumulated into equally sized time bins to obtain error bars on the measurements. Figure 1.16 shows this process for the same modulation as in Fig 1.15 but plotting the value of Q_x versus the magnet strength. This data is manually or automatically cleaned for outliers. Then, a linear fit over the points is computed to obtain the slope, i.e. $\Delta Q_{x,y}/\Delta K$, from which $\beta_{AV_{x,y}}$ for Beam 1 and 2 can be obtained using Eq. (1.42). The values of the resulting β^* are computed from the β_{AV} by using numerical optimisation methods [43].

The speed of this method is limited mainly by the speed at which the power supplies can change the current in the quadrupoles. As it can be also checked in Fig 1.15, modulation of a single quadrupole takes about 4 minutes, and must typically be repeated for the 4 quadrupoles in IP1 and IP5 and the two quadrupoles around IP2 in heavy ion collision runs.

The precision on the resulting β^* depends strongly on the quality of the measurement of the tunes. Several techniques are used to try and improve the tune measurement, one of which is the outlier cleaning mentioned before. Also, to improve the precision of the measurement, one can increase the amplitude of the modulation which would decrease the uncertainty on the slope of the Q/K relation, however, as the modulation strength increases the horizontal and vertical tunes approach and the ΔQ_{min} produced by betatron coupling mentioned in Sec. 1.3 alters the tune measurements. In Sec. 2.4 an attempt to improve this situation using the tune feedback will be explained.

There is also a inherent noise in the tunes of the machine, mainly produced by the jitter of the

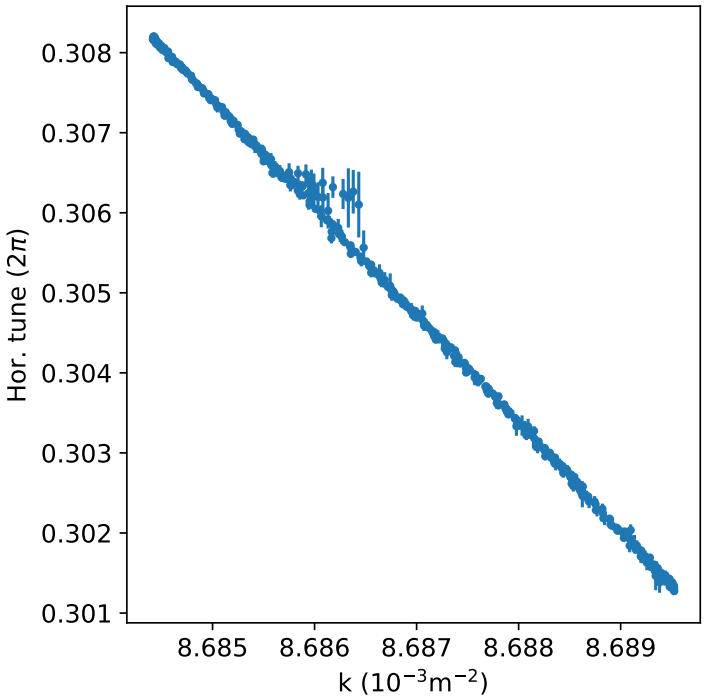

Figure 1.16: Relation between the change on the modulated quadrupole strength and the response of the horizontal tune.

power supplies that power the quadrupoles. As explained before, quadrupoles in locations with large β-functions have a larger impact on the tune. Therefore, at low β^* configurations, the main contributors to the tune noise are the triplet quadrupoles. In Section 2.4.1 some advancements made in the HL-LHC circuit design that will allow the reduction of the tune noise in HL-LHC are discussed.

Chapter 2

Local optics corrections in the HL–LHC

During the LHC Run 2, the optics corrections have brought the global r.m.s. β-beating in the machine to the 2% level and the r.m.s. β^*-beating down to the 1% level [42, 38, 44]. The target for HL-LHC is to keep the optics quality at least of on the same level as has been achieved in the LHC. However, the continuous effort to reduce the beam sizes at the interaction points is starting to bring up the limitations of current optics measurements and correction methods. For HL-LHC this is viewed as one of the main challenges from the optics correction point of view [45]. A failure to control local optics in strongly squeezed configurations can lead to reduced luminosity and to a luminosity imbalance between ATLAS [14] and CMS [15] (and ALICE [16] in case of ion physics). Accurate optics control is also fundamental to ensure the machine safety.

K-modulation explained in Section 1.7.3 has been the tool used to measure β^* and waist shifts during LHC Run 2, which has been essential to achieve an unprecedented performance of the machine during the run. Recent measurements during experimental studies at low-β^* and flat optics (different horizontal and vertical β^*) have revealed significant limitations in β^* measurements for these optics regimes. Also, theoretical studies for HL-LHC [43, 46] show that K-modulation will not reach the precision requirements to ensure the expected performance of the machine. Therefore, for the future of the LHC it will be essential to count on alternative methods for β^* control to complement or replace K-modulation, one of which will be demonstrated theoretically and experimentally in this chapter, using a combination of phase advance measurements across the IR (Sec. 2.5) and luminosity scans with waist shifts (Sec. 2.6).

The Achromatic Telescopic Squeeze (ATS) scheme [20] has become operational in the LHC and it is the baseline for HL-LHC. This optics scheme uses the arcs around the low-β^* insertions, namely arcs 81/12 and arcs 45/56, to aid the matching section quadrupoles to match the optics in the interaction regions and correct the chromatic effects by allowing an increase of the β-function in these arcs, peaking at lattice sextupoles. As a downside, this increase of the β-function in the arcs also enhances the effects from magnetic or alignment errors and affects the optics quality. The lack of individually powered quadrupoles in the arcs makes these errors very challenging to correct.

In this chapter of the thesis are presented the theoretical framework and experimental proof-of-principles on two techniques to improve the performance of optics local corrections in Run 3 and in HL-LHC: the calculation of the β_w from phase advance and the determination of the waist position using luminosity scans.

Additionally, this thesis presents a way of correcting the enhanced local errors in the arcs caused

by strong optics squeeze using the ATS scheme using orbit bumps in sextupoles to produce a quadrupolar fields via feed-down. The first experimental results of this technique, performed during machine development studies in the LHC are also presented here.

In Section 2.1 the need and implementation of an automatic local-optics correction tool are discussed together with performance results from measurements and simulations. In Section 2.4 the issues found experimentally in K-modulation measurements together with possible mitigation techniques are presented. In Section 2.5 an alternative to K-modulation to measure the minimum β-function in the interaction regions using phase-advance is presented. In Section 2.6 a complementary method to find the location of the beam waist by displacing it and measuring luminosity is also presented. In Section 2.7 the large β-beating produced by local errors in the high-beta ATS arcs observed in the LHC and expected for HL-LHC are shown and the implemented and foreseen solutions are discussed.

2.1 Automatic local optics corrections

Traditionally, the betatron phase-advance has been the most robust optics observable as it is independent of Beam Position Monitor (BPM) calibration and tilt errors and it does not rely on a model of the machine. As it was presented in Sec. 1.7, local phase errors in the IRs have been successfully corrected using the Segment-by-segment technique [31, 39]. The measured phase-advance in chosen segments of the accelerator can be compared to a model of the segment using MAD-X [34], whose initial conditions are set from measurements at the initial point of the segment. In this way, only quadrupolar errors within the segment affect the phase beating between measurement and propagated model. The model of the segment is matched to the local phase deviations by trimming the quadrupoles in the region. By swapping the sign of these trims an effective correction is obtained.

The effective model described in Sec. 1.7 was historically computed manually, by trying different settings of the quadrupoles in the region. This was very time consuming and not reproducible. In order to overcome the limitations of the manually computed local corrections, an automatic matching routine is presented this thesis. This routine generates these effective models, and therefore local corrections, automatically.

The automatic matching routine addresses the matching problem as an optimisation problem. The variables or degrees of freedom of the problem are the strengths of the quadrupoles in the segment. The target or constraints are the difference between the phase advance deviation from the local model (blue line in Fig. 1.12) and the effective model phase advance deviations (orange line in Fig. 1.12). By minimising this difference, using the LMDIF routine (a version of the Levenberg-Marquardt algorithm) included in MAD-X, an effective model is found. The automatic tool fulfils the following requirements:

- As the two beams traverse a common set of quadrupoles in the triplets region, a common correction must be found for both beams.

- The tool must be able to include the measurement data of the β-function obtained by the K-modulation at the IP which must be included as a constraint to avoid significant waist shifts.

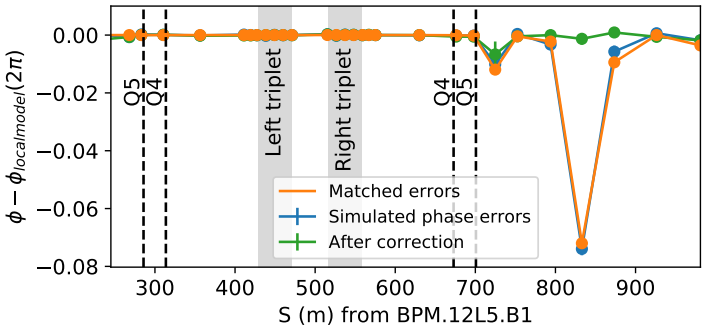

Figure 2.1: Example of a simulation of the HL-LHC with quadrupolar errors in the triplet and Q4-5. The blue line shows the deviation of the phase-advance from the design model of the segment. The orange line is the suggested effective correction and the green the effect of the correction.

- For local coupling correction not only both beams must be matched simultaneously, but such matching must also be achieved for the real and imaginary parts of the f_{1001} (see Sec. 1.6.3) resonance driving term.

- The tool must also allow the simultaneous automatic matching of forward and back propagations. (see Sec. 1.7) of the segments with a double number of constraints.

In addition, apart from fulfilling said requirements, an automatic routine improves the accuracy and reproducibility of the corrections when compared with those computed manually. Moreover, in view of HL-LHC where β^* levelling will be used [47] which will require to commission up to 50 different optics [48], computing local corrections of every one of them would be a extremely hard task to perform manually. The automatic tool is much faster in performing the corrections for each optics.

This algorithm has been extensively tested in HL-LHC simulations and put in practice in LHC optics commissioning and dedicated experiments [49, 50].

In Fig. 2.1 an example of the behavior of the automatic matching tool on the HL-LHC lattice is shown. The triplet quadrupoles (see layout on top of Fig. 2.2) and the two matching quadrupoles (Q4-5, displayed in the vertical lines of Fig. 2.1) in each side of the interaction point (IP) are given random 10^{-3} relative gradient error and the triplet circuits are used as variables to compensate the errors. The target solution is constrained by the measured deviation of phase-advance and β-functions from K-modulation for both beams. The blue line shows the simulated deviation of the phase-advance from the local model of the segment and in orange the suggested match performed by MAD-X optimisation. The green line shows the local errors remaining after applying the suggested matched values with its sign reversed.

The same technique can be used to correct local coupling by targeting the f_{1001} resonance driving term [39] as shown in Fig. 2.3. These local coupling errors are caused by random tilts of the triplet quadrupoles and Q4-5, producing coupling via feed-down. The coupling is corrected using the 2 skew quadrupoles in the IR (Fig. 2.2 top).

The importance of a good local coupling correction was brought to view in the ions run of 2018, where a human error caused the swap of the left and right corrector strengths given by this technique

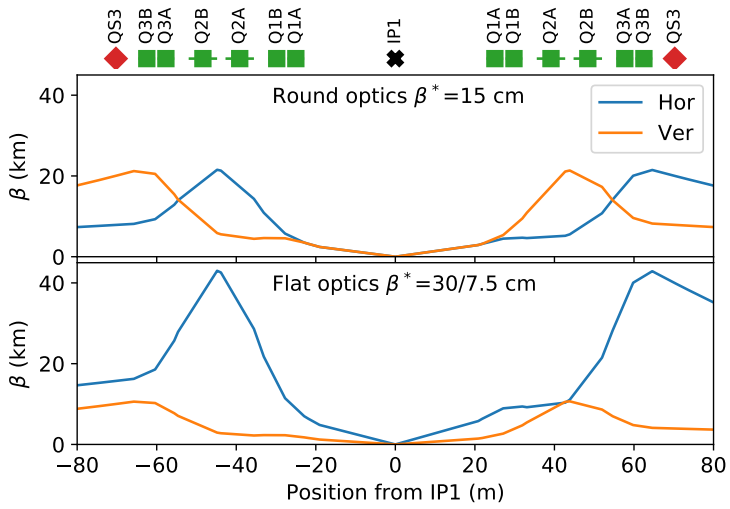

Figure 2.2: Schematic of the quadrupoles layout and β-function in the triplet region of HL-LHC around IP1 for round and flat optics.

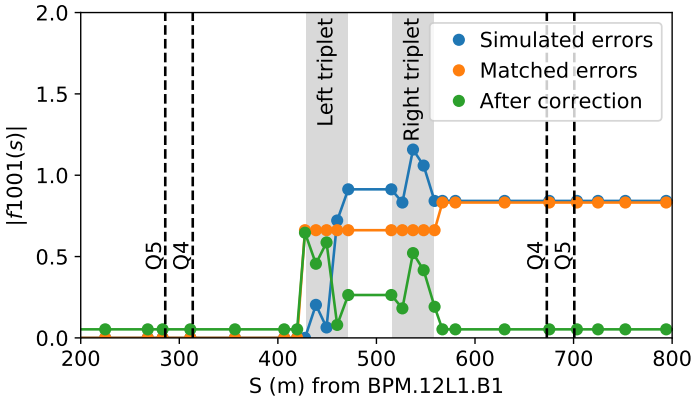

Figure 2.3: Example of a simulation of HL-LHC with tilt errors in the triplet and Q4-5 quadrupoles. The effect of these errors in the $|f_{1001}|$ is shown in blue. The suggested effective correction is shown in orange, but it should be noted that the matching routine matches the real and imaginary parts of the f_{1001} resonance driving term. The effect of the correction is shown in green.

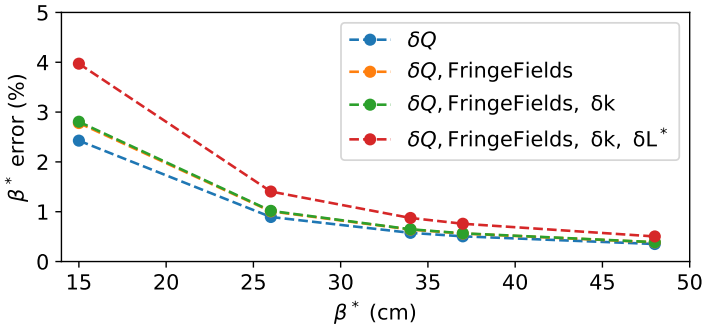

Figure 2.4: Simulation of the evolution of the β^* error from K-modulation with the design β^*. The effect of a tune uncertainty of $2.5 \cdot 10^{-5}$ is shown in the blue line. The orange line (partially covered by the green line) also considers the modulating quadrupole fringe fields. In the green and and red lines a 10^{-3} relative uncertainty in the field of the modulating quadrupole and a 2 mm uncertainty in the longitudinal position of the quadrupole have been respectively added.

and produced a 50% loss of luminosity in ALICE [51].

2.2 β^* corrections performance in the HL-LHC

To assess the performance of this technique in the HL-LHC, we performed Monte-Carlo simulations of the expected field and alignments errors in the interaction region quadrupoles, and applied the automatic correction described above to each of the simulation seeds.

Specifically, each quadrupole of the triplet and Q4-5 is given a random 10^{-3} relative quadrupolar error from a Gaussian distribution and a ± 2 mm longitudinal misalignment, the magnet alignment tolerance expected in the HL-LHC. Sorting (see Sec. 2.4.1) is applied to the two parts of the Q2 quadrupoles with the aim to avoid big relative field imbalances between them.

The resulting phase-advance deviations in the IP1 and IP5 segments are also disturbed with Gaussian noise to simulate the measurement noise. This noise is assumed to be 6 mrad r.m.s. at a BPM with β=171 m and scaled to the rest with the $\sqrt{\beta}$ at their location.

To simulate the K-modulation measurement, the matching algorithm is also provided with the value of the β^* with an uncertainty of 4%, corresponding to a tune uncertainty of $2.5{\cdot}10^{-5}$ as shown in Fig 2.4. This value of the tune uncertainty is an optimistic estimation of the expected value that assumes an upgrade of the arcs power supplies that is not in the HL-LHC baseline, as detailed in [46]. However, the target of the algorithm is to correct down to this β^* uncertainty level, therefore this assumption does not bias the results.

Figure 2.5 shows the remaining β^*-beating in IP1 and IP5, after applying the automatic correction in each seed. The standard deviation of the resulting distribution is σ=3.8%, very close to the given uncertainty of K-modulation, which indicates that the automatic matching routine successfully corrects the β^*-beating down to the uncertainty of the β^* measurement.

Figure 2.6 shows the relative difference between the error in each quadrupole of the triplet and the correction found by the matching routine. The correction strength stays in general on the level of the magnetic errors (10^{-3}) but raises to about $5 \cdot 10^{-3}$ in r.m.s. in the Q1s. We interpreted this increase of strength as a compensation for the 2 mm misalignment and Q4 and Q5 errors.

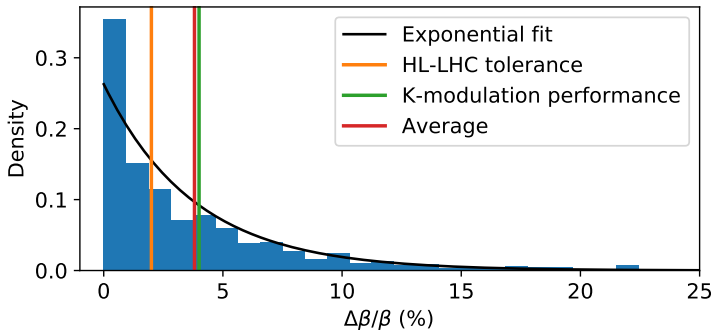

Figure 2.5: Remaining β-beating in IP1 and IP5 in the horizontal and vertical planes for 100 simulation of triplet and Q4-5 errors after the automatic local corrections, for a precision in K-modulation compatible with 4% precision in the measurement of β-beating. The density on the vertical axis refers to the number of samples in the bin over the total number of samples. The standard deviation of the distribution is 3.8%, very close to the precision in K-modulation.

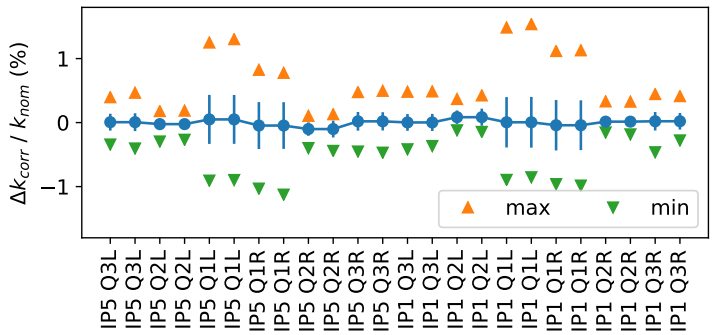

Figure 2.6: Average, standard deviation, maximum and minimum of the relative difference between the value of the magnetic errors of each seed and the strength of the correction implemented at each triplet quadrupole. Small values indicate that the value of the correction applied to a magnet is close to the actual error in that magnet.

2.3 Triplet tilt tolerances in the HL-LHC

A tilted quadrupole interacts with the beam as a straight quadrupole plus a skew quadrupolar component. This skew component will have an effect in the f_{1001} resonance driving term given by [52]:

$$f(s)_{1001} = \frac{-1}{4(1 - e^{2\pi i(Q_x - Q_y)})} \sum_l kL_l \sqrt{\beta_x^l \beta_y^l} e^{i(\Delta\phi_x^{sl} - \Delta\phi_y^{sl})} \tag{2.1}$$

where kL_l is the l^{th} skew quadrupole integrated strength, $\beta_{x,y}^l$ are the β-functions at the position of the l^{th} skew quadrupole, $\Delta\phi_{x,y}^{sl}$ are the phase-advances between the measurement point and the l^{th} skew quadrupole and $Q_{x,y}$ are the horizontal and vertical tunes. It can be seen how due to the large β-function across the HL-LHC triplet shown in Fig. 2.2, tilts of the triplet quadrupoles have the potential to be massive contributors to the magnitude of the f_{1001} term and therefore, to the coupling in the region and in the whole machine if not properly compensated locally. In HL-LHC, a skew quadrupole corrector will be installed in each side of IP1 and IP5 (Fig. 2.2 top schematic) to cancel out the local coupling produced by the triplet.

In order to define the required strength of these correctors, we performed automatic corrections of 500 simulation of the HL-LHC triplet expected tilts. On each seed, all the quadrupoles of the triplet and Q4-5 were given a random tilt within ±1 mrad and ±2 mrad (uniformly distributed). Also, a random choice among 60 seeds of sextupolar to dodecapolar normal and skew multipolar errors (b3, a3, b4, a4, b5, a5, b6 and a6) was given to each seed. The simulations were performed at β^*=30/7.5 cm flat optics (worst case scenario) with a crossing angle of 250 μrad.

Early estimates of the field errors of the quadrupoles of the HL-LHC triplet showed an a2 multipolar error of about 2 to 3 units [53]. This will produce the same effect as the tilt of the quadrupoles, inducing betatron coupling. However, performing a MAD-X simulation it can be verified that, if θ is the tilt in radians and a2 the field error in units, then a2 $\approx 2\theta$. Therefore, a tilt of 2 mrad corresponds to about 40 units of a2 field error which makes the effect of the field error negligible and it is consequently ignored in this study.

Figure 2.7 shows the resulting strengths of the skew quadrupoles as calculated by the automatic matching routine for each of the 500 seeds. The measurable traditionally used to quantify the global coupling is the ΔQ_{min} i.e. the minimum difference between the horizontal and vertical tunes produced by coupling [37]. For these simulations, after the local coupling corrections, the uncorrected coupling that leaks from the IR produces a ΔQ_{min} below 10^{-3} for all seeds.

The solid lines of Fig. 2.7 show the original design strength of the HL-LHC skew quadrupole correctors: 10^{-3}m^{-2}. Having such a large margin available, if the tilt is guaranteed to stay within ±1 mrad, which can be assured using the remote alignment system [54], the design strength for the correctors can be reduced to $0.7 \cdot 10^{-3}\text{m}^{-2}$ (dashed lines) while still allowing a factor 2 margin in case one of the correctors stops functioning. The resulting strengths of the right and left correctors in each seed show a tendency to lay across the diagonal, namely, to set both correctors to a similar strength.

Quadrupoles can also present local tilts along their length (*waviness*) as illustrated in Fig. 2.8. Monte-Carlo simulations of this effect have also been performed, applying local tilts to 10 thick

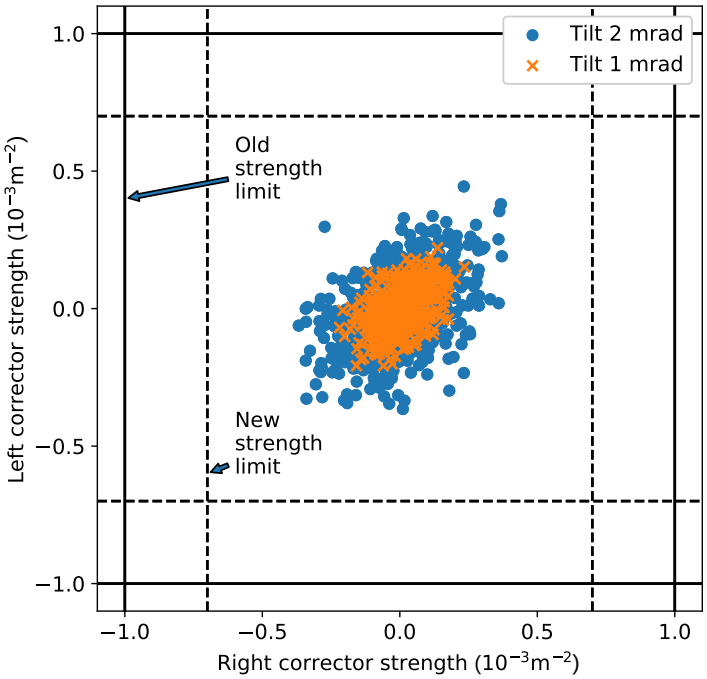

Figure 2.7: Required strength of the skew quadrupole correctors in IR1 to cancel the coupling produced by 500 seeds of random tilts of ±1 mrad and ±2 mrad in Q4-5 and the triplet quadrupoles. The solid lines show the old specification for the strength limit of the correctors and the dashed lines the new specification set by this work.

slices of each quadrupole of the triplet, concluding that up to ±5 mrad uniformly distributed waviness has a negligible effect when compared with the average tilt of the magnet. This means that a ±5 mrad waviness is tolerated if the average tilt is controlled within ±1 mrad.

In conclusion, these simulation results show that the automatic matching routine is able to correct local optics to the β^* measurement accuracy. Therefore, the limiting factor for HL-LHC to deliver the design luminosity and to keep the luminosity imbalance within tolerable levels, is the accuracy of the measurement of the β^*. In following sections we will describe the problems of currently used techniques and possible alternatives for HL-LHC. The matching routine also succeeded defining the required strength of the skew quadrupole correctors in IR1 and IR5, allowing a reduction of these correctors strengths, reducing the construction cost of HL-LHC.

2.4 K-modulation issues

K-modulation has been the technique used to measure and control the LHC β^* during Run 2 [38]. However, for low-β^* optics, this technique is starting to approach its main limitation: the precision of the measurement reduces with the growth of noise in tune measurements, and this noise increases mainly with the β function growth in the main triplets quadrupoles.

For instance, in Table 2.1 the average and r.m.s. of beam waist measurements performed at β^*=30 cm (the operational optics of 2018) is presented, showing a large spread over several measurements. During studies of flat optics with β^*=60/15 cm, this technique showed systematic unreliable measurements of the β^* since K-modulation is validated against phase measurements

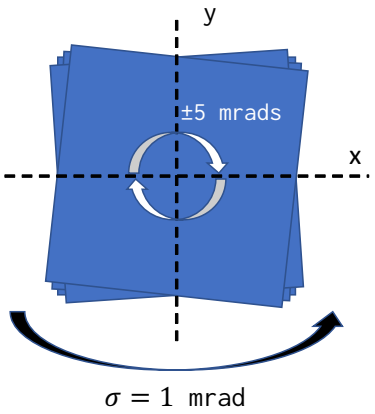

Figure 2.8: Illustration of the simulated *waviness* of one of the quadrupoles of the triplet. The quadrupole is divided in 10 slices with ±5 mrad rotation each, but the average rotation of the whole triplet is ±1 mrad.

with the AC dipole as explored in the following.

Taking into account the presence of a beam waist, the formula that describes the β-function across the optics drift around the IP, Eq. (1.26), changes to

$$\beta(s) = \beta_w + \frac{(s-w)^2}{\beta_w}, \tag{2.2}$$

with $\beta(0)$=β^* the β-function at the IP and w the waist position w.r.t the IP i.e. the point where $\beta(w) = \beta_w$, the minimum β-function in the drift.

Then the phase-advance between the beginning and the end of this optics drift is equal to

$$\phi_{IP} = \arctan\left(\frac{L^* - w}{\beta_w}\right) + \arctan\left(\frac{L^* + w}{\beta_w}\right), \tag{2.3}$$

being L^* the distance between the BPM and the IP, assuming that the BPM is upstream of the first triplet quadrupole when moving from the IP. As K-modulation provides the β_w and waist position, this ϕ_{IP} can be compared with the ϕ_{IP} measured using BPM turn-by-turn data of beam excitations with the AC dipole.

Table 2.2 shows K-modulation measurements of Beam 1 performed at β^*=60/15 cm optics for the vertical plane of IP5 in 2017 [49] and for the horizontal plane of IP1 in 2018. In both cases, the design β^* is 60 cm. The measurements show a not too large error and, in principle, should be trusted.

One of the results of this thesis, however, is the use of Eq. (2.3) to verify the results of K-modulation against the measurement of the phase advance using the AC dipole. Therefore, Table 2.2 also shows the deviation of ϕ_{IP} w.r.t. the model for both K-modulation computed using the formula above and from standard BPM measurements on beam excitations with the AC dipole. The phase measured from K-modulation is not compatible with that measured by BPMs for these 3 cases. The reason for this disagreement is not clear, but shows that K-modulation can give unreliable results in certain conditions.

Waist [cm]	from K-mod	from lumi. scan
Beam 1	-5 ± 3	-8.1 ± 1.1
Beam 2	4 ± 2	0.3 ± 0.3

Table 2.1: Comparison of the average over 5 measurements of the vertical waist displacements measured by K-modulation and the waist obtained using the luminosity scans.

	β^* [m]	Waist [m]	$\Delta\phi_{K-mod}$ $[2\pi 10^{-4}]$	$\Delta\phi_{kicks}$ $[2\pi 10^{-4}]$
2017 No corr.	1.45 ± 0.05	0.72 ± 0.03	-104 ± 8	-4 ± 13
2017 Corr.	1.17 ± 0.06	0.57 ± 0.03	-79 ± 10	-4 ± 12
2018 No corr.	0.83 ± 0.03	0.32 ± 0.03	-26 ± 4	-6 ± 7

Table 2.2: K-modulation measurements before (No Corr.) and after (Corr.) corrections of the β^*, waist and deviation w.r.t. the model of the ϕ_{IP} both from K-modulation ($\Delta\phi_{K-mod}$, Eq. (2.3)) and from excited beam BPM recordings ($\Delta\phi_{kicks}$) at flat optics β^*=60/15 cm. The problem appeared in IP5 in the vertical plane in 2017 and in the horizontal plane of IP1 in 2018, both on Beam 1. The design β^* is 60 cm in the vertical plane of IP5 and the horizontal plane of IP1 (the flat plane is swapped in IP1 and IP5).

One option to increase the accuracy of K-modulation could be to increase the strength of the modulation allowing larger tune changes. The limit of the change in the tune produced by K-modulation is set to be $\frac{1}{3}(Q_x - Q_y) = 10^{-2}$ [43] at injection tunes, to avoid hitting the coupling stop-band. In principle, the LHC tune feedback system [55] could be used to compensate the change on the tune removing this limit and allowing for stronger modulations. In Fig. 2.9, an attempt to perform K-modulation with the tune feedback active is shown. It should be noted that the modulation of the tunes is not totally removed, it remains an oscillation of about 10^{-3}. Also in the vertical tune of Beam 2 a delay time in the reaction of the system can be observed. These technical difficulties would make this approach unfeasible with the current system. Moreover, Fig. 2.10 shows a simulation of K-modulation with tune feedback using the arcs tuning quadrupoles correctors (MQTs) to keep a constant tune. It shows the difference in the tune change from Q1 and the tune change inferred from the feedback quadrupoles (MQTs) versus the Q1 tune change, demonstrating how the cross talk between the β-beating wave produced by the modulation of Q1 and the MQTs dominates over the error caused by the tune uncertainty for modulations higher than 10^{-2}. Therefore, K-modulation with the tune feedback presents significant difficulties both on the technical and analytical sides and it is discarded for the future.

Due to the first unreliable observations of K-modulation during Run 2 and the failure to operate it with the tune feedback to increase its accuracy, it will be essential to have alternative techniques to K-modulation for the Run 3 of the LHC and in view of HL-LHC where the β^* will be even lower.

2.4.1 HL-LHC circuit redesign

In Sec. 1.7.3 it was shown how the measurements precision of K-modulation depend heavily on the precision of the tune measurement and therefore the tune noise and in which way the triplet quadupoles are the main source of tune noise at low β^*. To achieve the precision of K-modulation shown in Fig. 2.4, a study on the design of the power supply layout and circuit design of the

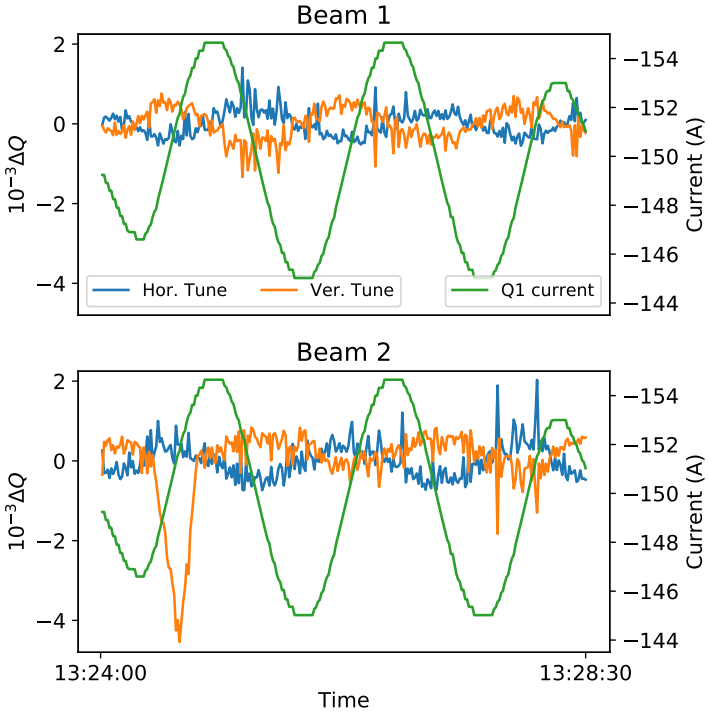

Figure 2.9: K-modulation performed during ATS optics MD studies in 2016 with the tune feedback system enabled. A residual oscillation of about 10^{-3} remains uncompensated. Also the system reacted too late compensating the vertical tune in Beam 2, as can be seen in the start of the orange line in the bottom plot.

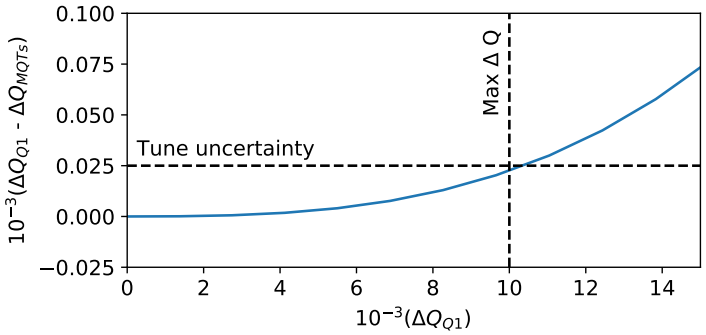

Figure 2.10: Simulation of a K-modulation using the tune feedback. Here ΔQ_{Q1} is the change of tune produced by the trim of the Q1 and ΔQ_{MQT} the change of tune produced by the arcs tuning quadrupoles to compensate the Q1 effect. The horizontal line shows the tune measurement uncertainty of $2.5 \cdot 10^{-5}$. When the curve is above this line the cross-talk between Q1 and arcs tuning quadrupoles is dominating the error of the K-modulation measurement. The vertical line shows the maximum allowed change of tune in the absence of tune feedback.

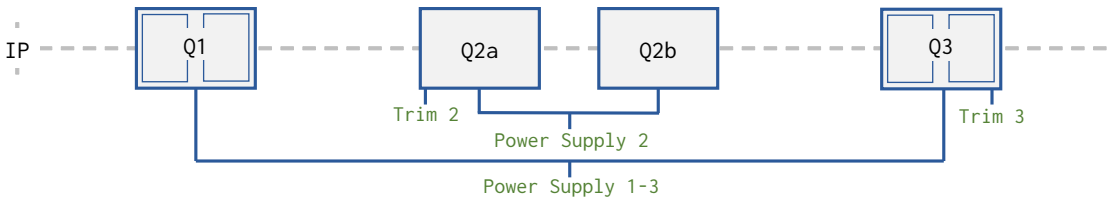

Figure 2.11: Diagram of the 2-power supply circuit configuration of the HL-LHC triplet

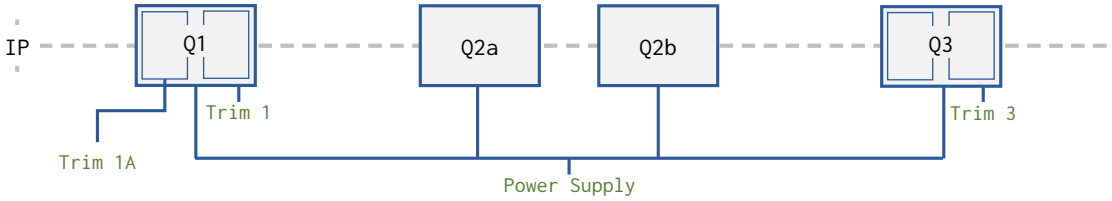

Figure 2.12: Diagram of the single power supply circuit configuration of the HL-LHC triplet, without the Q2a trim and with the trim in Q1a purposed for K-modulation.

HL-LHC triplet was made.

Figure 2.11 shows a diagram of the power supply circuit initially designed for the HL-LHC. It consisted of two main power supplies, one powering Q1 and Q3 and another one powering Q2. A smaller correction trim was available in the first half of Q2 (Q2a) and on Q3.

The current ripple of these main power supplies is the main source of tune noise. Therefore, it is desirable that the effect this ripple produces on the tune cancels out as much as possible. Figure 2.12 shows the second proposal for the power supply circuit of the triplet. It consisted of only one main power supply, a trim in Q1 a trim in Q2a and a trim in Q3. Having only one main power supply means only one source of noise among the whole triplet, allowing for compensation between the noises of Q1-3 and Q2.

As the Q1-3 quadrupoles and the Q2 have opposite polarities, it was suspected that having a single power supply would allow for the tune noise produced to cancel out. Performing Monte-Carlo simulations in MAD-X, assigning 0.1 parts per million noise on 1000 seeds to the HL-LHC triplet in IR1 and IR5 in the two different proposed power supply configurations, we proved that the new power supply layout reduced the impact of the current ripple on the tune noise a factor 2 [56].

To save resources on the construction of this new circuit, we also studied if the trim of Q2a is actually necessary. This trim was designed to avoid strong imbalances between the focusing strength of Q2a and Q2b that could not be compensated with a common power supply. These imbalances can be mitigated by applying sorting in the Q2 quadrupoles, i.e. by measuring the field of each of the Q2 halves before their installation and pairing together as part of the same Q2 those with the most similar measured field. In Sec. 2.2 the corrections are performed without the Q2a trim and simulating the sorting of Q2, proving that the trim in Q2a is not necessary to correct the optics. This trim has been therefore, removed from the circuit specification [56].

Finally, to achieve the expected results of K-modulation in HL-LHC, we proposed the addition of a trim in the first half of Q1 (Q1a) alone. The trim of Q1 as a whole can also be used to extrapolate its average β-function to the β^*, but the independent uncertainties of the two quadrupoles together

makes this measurement a factor 2 less precise. The trim of Q1a is purposed exclusively to perform K-modulation and it was designed following to match the speed and amplitude of the K-modulation measurements in the LHC.

In summary, this study strongly influenced the design of the HL-LHC triplet, allowing for a factor 2 tune noise reduction, the removal of the trim on Q2a with the consequential save in resources and another factor 2 improvement in K-modulation measurements precision using an independent trim on Q1a.

2.5 β_w from phase-advance

The need to squeeze the beam to very low-β^* pushes the β-function in the IR region to very large values and therefore, the betatron phase-advance becomes so small that is barely measurable with the standard BPM resolution in the LHC. Nevertheless, an expression to obtain the β_w from the ϕ_{IP} can be derived and rely on BPMs with higher precision in the measurement of the phase-advance. Expanding Eq. (2.3) around $w = 0$ up to the second order in w one obtains:

$$\phi_{IP} = 2\arctan\left(\frac{L^*}{\beta_w}\right) - \frac{2\beta_w L^{*3}}{(\beta_w^2 + L^{*2})^2}\left(\frac{w^2}{L^{*2}}\right) + O\left(\frac{w^4}{L^{*4}}\right) \ . \tag{2.4}$$

This expansion is valid if

$$w \ll L^* \ . \tag{2.5}$$

This condition is fulfilled in the LHC where L^* is of the order of tens of meters and typical waist shifts are of several centimetres. As it can be seen from Eq. (2.4) to the lowest order the phase advance ϕ_{IP} behaves as the square of the waist position. This formula can be considered as an equation for β_w. Solving it up to the second order in w/L^* the following approximate solution can be obtained

$$\beta_w \approx \frac{L^*}{\tan\left(\frac{\phi_{IP}}{2}\right)}\left[1 - \sin^2\left(\frac{\phi_{IP}}{2}\right)\left(\frac{w^2}{L^{*2}}\right) + O\left(\frac{w^4}{L^{*4}}\right)\right] \ . \tag{2.6}$$

In Fig. 2.13 the behaviour of ϕ_{IP} is shown versus β_w for a $\pm 50\%$ range from 15 cm and versus the waist position for a range of ± 25 cm. The effect of the waist displacement on ϕ_{IP} is four orders of magnitude lower than that of the β_w, becoming smaller for lower β_w.

Ignoring the influence of the waist displacement we obtain a simpler formula:

$$\beta_w \approx \frac{L^*}{\tan\left(\frac{\phi_{IP}}{2}\right)} \ . \tag{2.7}$$

This approximation produces a maximum error in β_w for the ranges of β_w and waist shown in Fig. 2.13 of about 0.01%.

Defining $\sigma(\beta_w)$ and $\sigma(\phi_{IP})$ as the uncertainties of the measurements of β_w and ϕ_{IP} respectively, we obtain:

$$\sigma(\beta_w) \approx \frac{L^*}{|\cos(\phi_{IP}) - 1|}\sigma(\phi_{IP}), \tag{2.8}$$

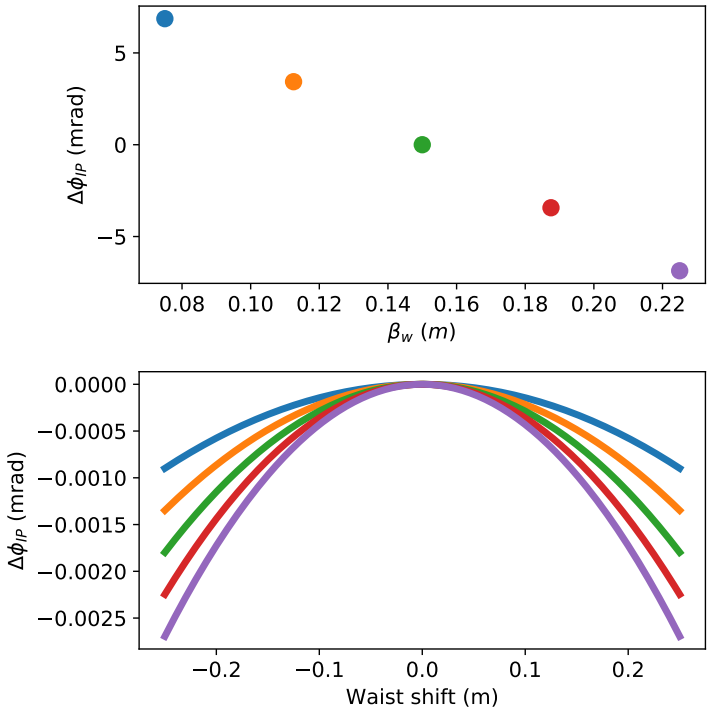

Figure 2.13: Behaviour of the phase-advance change across the IP optics drift with changing β_w (top) and changing waist shift (bottom). As the change with waist shift depends significantly on the β_w the phase deviation with changing waist shift is shown for the different β_w in the upper plot, with corresponding colors.

or in relative terms to β_w:

$$\frac{\sigma(\beta_w)}{\beta_w} = \frac{\sigma(\phi_{IP})}{|\sin\phi_{IP}|} \tag{2.9}$$

This ϕ_{IP} is typically close to π. For instance, in the case of β^*=50 cm ion optics the design $\sin(\phi_{IP})$ is about $5{\cdot}10^{-2}$. To obtain a 2% precision in $\sigma(\beta_w)/\beta_w$ a precision of $\approx 2\cdot10^{-2}\cdot5\cdot10^{-2} = 10^{-3}$ rad in the measurement of the phase is necessary.

2.5.1 The DOROS BPM system

The Diode ORbit and OScillation (DOROS) BPM system [57] is installed in the LHC tertiary collimators jaws and next to the IPs. This opens the possibility of measuring the β_w from phase measurements coming from this system using Eq. (2.7). It provides better phase resolution than standard BPMs and can be triggered together with them. This system has been used to obtain more accurate measurements of the betatron coupling [58].

In order to experimentally validate the studies presented in Sec 2.5, the DOROS BPM system was triggered during the ion run commissioning of 2018 in the LHC, with 50 cm β^* optics. A total of 6 acquisitions of the standard BPM system and 8 acquisitions of the DOROS system were triggered. Using these acquisitions, a standard deviation on the phase advance across the IR of 0.3 mrad was found using the DOROS system and 1.1 mrad using the standard BPM system, about a factor 4 larger. Applying Eq. (2.7) on this measurement of the phase advance results β_w=0.56±0.01 for the normal LHC BPM system and β_w=0.544±0.003 for the DOROS BPM system. The slight difference between these values might be due to a small drift of the optics during the measurement, but this remains to be confirmed in future experiments.

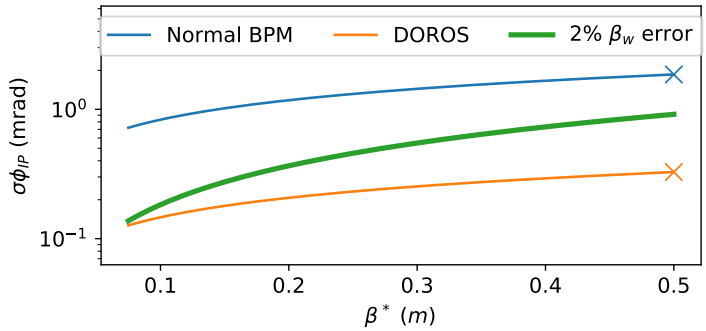

Figure 2.14: Expected measurement error of the standard and DOROS BPM systems taking as reference a measurement at 50 cm β^*. The green line shows the required phase measurement error to achieve a 2% error in β_w.

In Fig. 2.14 the previous measurement of the precision of the phase advance across the IR is extrapolated to smaller β^* showing how the DOROS system provides a β_w measurement below the required error for 2% precision for all the optics in the range from 50 cm to 7.5 cm β_w, positioning the phase-advance measurement with DOROS BPMs as a good alternative to K-modulation to measure β_w. However, as it was shown before, it does not give information about the actual waist shift which can strongly impact the β^*. In the next section, the use of luminosity scans to measure the waist shift is proposed.

2.6 Luminosity scans

An alternative technique to measure waist shifts is to design a set of quadrupole trims that displace the beam waist. Applying such knobs step by step, the beam waist changes linearly and β^* quadratically as shown in Fig. 2.15. By monitoring the luminosity the position of the beam waist can be interpolated.

Luminosity waist scans have been performed in other colliders as SuperKEKB [59, 60], however the particularities of the LHC make this technique significantly more challenging. In the LHC machine protection constraints force us to keep the β-beating in the machine within safe values during the scans, which poses a strong constraint on the design of the waist shift knobs and their operational range. The luminosity changes for the design waist shift of about 10 cm are in the order of about 1%, significantly smaller than in other colliders, challenging the data acquisition and the analysis accuracy as described below.

A generalization of Eq. (1.25), without assuming identical bunch sizes in Beam 1 and Beam 2 anymore, the luminosity measured at each IP is the following:

$$\mathcal{L} = \frac{N_b f N_1 N_2 S}{4\pi \sqrt{\frac{\epsilon_{x1}\beta^*_{x1}+\epsilon_{x2}\beta^*_{x2}}{2}} \sqrt{\frac{\epsilon_{y1}\beta^*_{y1}+\epsilon_{y2}\beta^*_{y2}}{2}}}, \tag{2.10}$$

where $\epsilon_{x1,y1,x2,y2}$ are the emittances in each plane. S, the luminosity reduction factor, that can be

approximated (ignoring the hourglass effect) as [10]:

$$S = \frac{1}{\sqrt{1 + \left(\frac{\sigma_s}{\sigma_x}\frac{\theta}{2}\right)^2}} = \frac{1}{\sqrt{1+\phi_p^2}}, \tag{2.11}$$

where θ is the crossing angle at the IP, σ_s the longitudinal beam size and ϕ_p is the so-called Piwinski angle.

For the case of a waist knob designed to displace the horizontal waist of Beam 1, assuming all emittances ϵ are equal and using Eq. 2.2 for the horizontal β-function on Beam 1, the horizontal beam size changes as:

$$\sigma_x(s) = \sqrt{\frac{\epsilon\beta^*_{x1}(s) + \epsilon\beta^*_{x2}}{2}} = \sqrt{\frac{\epsilon(\beta_w + \frac{(s-w)^2}{\beta_w} + \beta^*_{x2})}{2}} \tag{2.12}$$

and normalising to the luminosity at the waist $\mathcal{L}_w = \mathcal{L}(w)$, the dependency of the luminosity on the β^* goes as:

$$\frac{\mathcal{L}(s)}{\mathcal{L}_w} = \frac{1}{\sqrt{1 + \frac{(\frac{s-w}{\beta_w})^2}{1+\frac{\beta_{x2}}{\beta_w}}}} \frac{\sqrt{1 + \frac{\frac{\phi_p^2}{\sqrt{2}}}{1+\frac{\beta^*_{x2}}{\beta_w}}}}{\sqrt{1 + \frac{\frac{\phi_p^2}{\sqrt{2}}}{1+\frac{\beta^*_{x2}}{\beta_w}+\left(\frac{s-w}{\beta_w}\right)^2}}} \tag{2.13}$$

which simplifies to:

$$\frac{\mathcal{L}(s)}{\mathcal{L}_w} = \sqrt{\frac{1 + \frac{\phi_p^2}{\sqrt{2}} + \frac{\beta^*_{x2}}{\beta_w}}{1 + \frac{\phi_p^2}{\sqrt{2}} + \frac{\beta^*_{x2}}{\beta_w} + \left(\frac{s-w}{\beta_w}\right)^2}}, \tag{2.14}$$

with s being the value of the waist displacement knob, w the actual waist present in the machine in Beam 1, β_w the beta on the waist of Beam 1 and β^*_{x2} the β^* of Beam 2.

The full luminosity equation can then be expanded for small $\frac{(s-w)}{\beta_w}$ as:

$$\frac{\mathcal{L}(s)}{\mathcal{L}_w} = 1 - \frac{(s-w)^2}{2\beta_w^2\left(1 + \frac{\phi_p^2}{\sqrt{2}} + \frac{\beta^*_{x2}}{\beta_w}\right)} + O\left(\left(\frac{s-w}{\beta_w}\right)^4\right) \tag{2.15}$$

The r.h.s. of this equation has the shape of a parabola and the values of the waist position w and the denominator can be extracted from a fit of the luminosity measurement against several values of the waist scan knob s. The denominator contains the information of the β_w, but the presence of the Piwinski angle means that a very precise measurement of the crossing angles and longitudinal beam profile is required to obtain a good measurement of the β_w. The typical resolution of both σ_s and the crossing angle is about 10% [61] and therefore this method cannot be used to obtain a precise measurement of the β_w. To obtain a precise measurement of the β_w the phase-advance from DOROS BPMs can be used as described in Sec. 2.5.

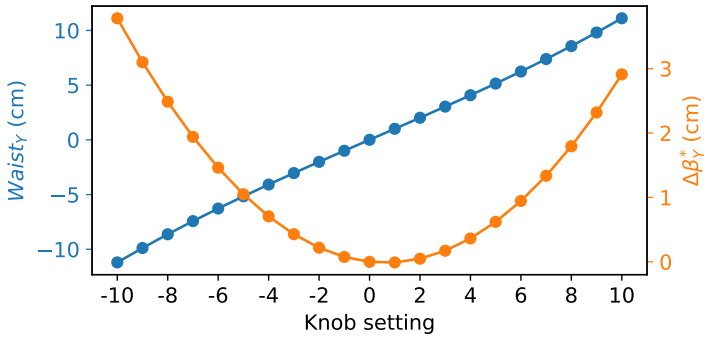

Figure 2.15: Simulated effect on the design model with β^*=30 cm optics of one of the waist displacement knobs experimentally tested in the LHC. The blue line represents the waist displacement and is almost completely linear with the knob value. The orange line shows the β^* following the parabola of Eq. (2.2) as the waist is displaced. The minimum of the parabola is not at the zero knob setting because the design optics includes a small waist.

2.6.1 Experimental validation of the luminosity scans

Waist scans have been successfully performed in the LHC during a MD session [62] that took place the 16*th* of September of 2018 with nominal optics, β^*=30 cm. Using MAD-X, two knobs were designed to shift the vertical waist of Beam 1 (Fig 2.15) and 2 at IP1.

The luminosity measurements in ATLAS is obtained mainly using the LUCID-2 Cherenkov detector [63], but this measurement is complemented by other detectors and algorithms. A detailed explanation on the determination of the luminosity produced at ATLAS can be found in [64].

In Fig. 2.16, the instantaneous luminosity acquisition from ATLAS for the first of these scans is shown. The periods when luminosity optimization was being performed (dips in the signals) or when the knobs were being trimmed were discarded from the analysis and are shown greyed out. There is a decay in the raw luminosity signal (blue line) caused by the beam burn-off produced by the collisions. This means that in Eq. (2.10) the terms $N_{1,2}$ are time-dependent. To remove this time dependency, the luminosity is divided by the measured $N_1(t)N_2(t)$ during the experiment, resulting in the orange line of Fig. 2.16. After this operation, the signal still has a noticeable decreasing trend, which can be attributed to emittance blowup during the experiment. As the points with the same knob settings should have the same luminosity value, additional effects like this emittance blowup can be removed by fitting a line over measurements with the same settings and rescaling the luminosity value to the found fit. In this case a line was fitted over two measurements when the knob waist was set to zero.

After postprocessing the data as described, the parameters of Eq. (2.15) can be fitted to the scaled luminosity versus knob setting. In Fig. 2.17, the scaled luminosity versus waist knob setting from -9 to 9 cm is shown, together with the parabolic fit. The measured vertical waist shift is -8.1 ± 1.1 cm in Beam 1 and 0.3 ± 0.3 cm in Beam 2 as shown in Fig. 2.18. Table 2.1 shows a comparison between the average and r.m.s. over 5 measurements of the waist position using K-modulation performed during 2018 and the results of the luminosity scans. It should be noted that the luminosity scans measurements have a significantly lower uncertainty. These first experimental results are promising, but to allow their use in operation the luminosity scans will have to be streamlined and their reproducibility over time must be confirmed with further scans.

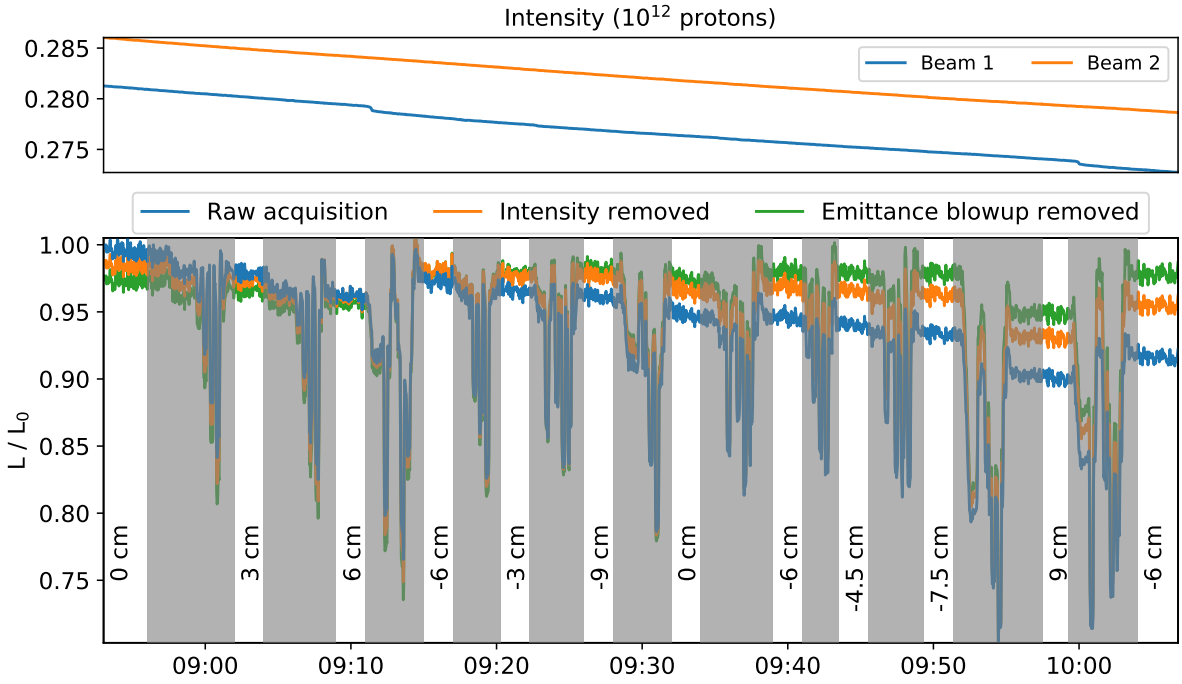

Figure 2.16: Instantaneous luminosity (relative to the first raw measurement) recorded by ATLAS during the first waist scan. In blue the raw luminosity as given by ATLAS and the orange line is normalised to the beams intensity. The green line has the emittance blowup decay removed and is the one used to fit the beam waist parabola. The parts removed from the analysis are greyed out.

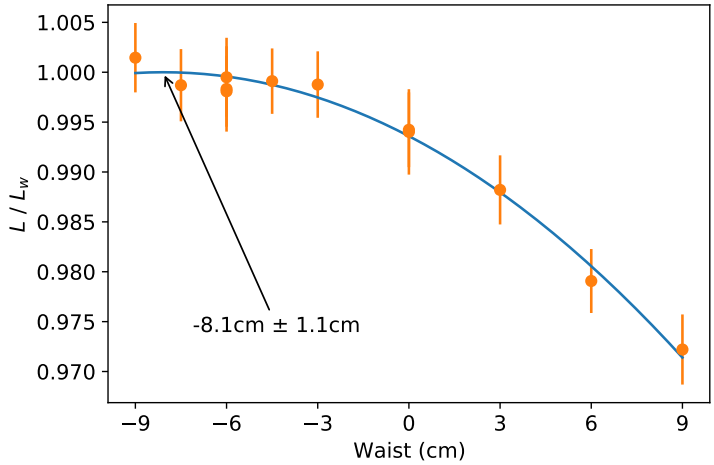

Figure 2.17: Luminosity scan of Beam 1 on the vertical plane.

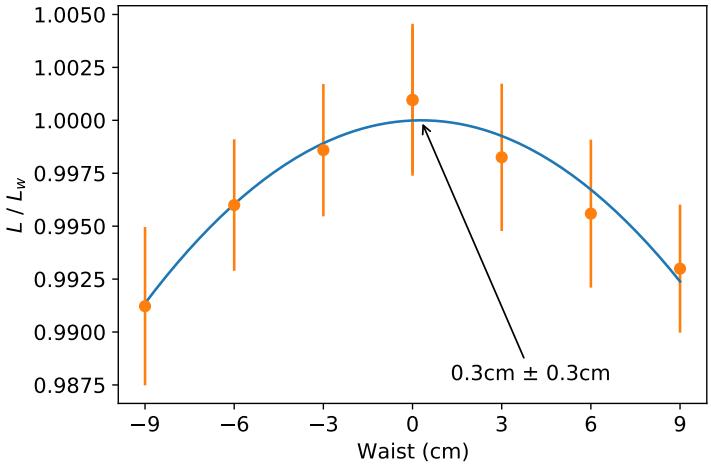

Figure 2.18: Luminosity scan of Beam 2 on the vertical plane.

Altogether, these are the first successful waist measurement using luminosity scans in the LHC, a machine with strong machine protection constraints. These results open the gate to complement K-modulation with a combination of IP phase advance measurements and luminosity scans, allowing a more precise determination of the β^*, which as was described before, will be of crucial importance to guarantee the performance of the HL-LHC.

2.7 Local arc corrections with orbit bumps

Number of experimental tests were performed with flat optics i.e. different horizontal and vertical β^* of 60/15 cm [65, 49, 50]. The ambitious optics configurations are achieved using the ATS scheme. The ATS scheme will also be used in the HL-LHC where it is expected to reach a β^*=30/7.5 cm in flat optics [47].

During the 2017 Machine Development (MD) session on flat optics with β^*=60/15cm [49], it was not possible to bring the β-beating in arc 45 below 24% after local and global corrections, as shown in Fig. 2.19, highlighting in grey the problematic arc. 20% peak β-beating is considered the upper limit to safely operate the LHC and in 2016 with β^*=40 cm the rms β-beating in the machine was brought down to the 2% r.m.s. level [38].

Using the Segment-by-segment technique on arc 45, this error was identified as a local error in this arc enhanced by the high design β-function of the ATS optics scheme. The peak β-beating produced by a gradient error in arc 45 might be enhanced up to a factor 4 when comparing 30 cm and flat 60/15 cm optics, as shown in Fig. 2.20 (top).

In that region of the accelerator, there are no individually-powered quadrupoles to correct the error, which explains the difficulties found in 2017 to correct arc 45 using global corrections. However, it is possible to produce quadrupolar fields via feed-down from sextupoles by traversing them with an non-zero orbit.

In Fig. 2.21 the results from Segment-by-segment of the phase deviation from the local model of arc 45 under 60/15 cm flat optics that was measured on 2017 is shown in blue. A solution to match this phase measurement was found to be a 5.2 mm horizontal orbit bump with maximum in the

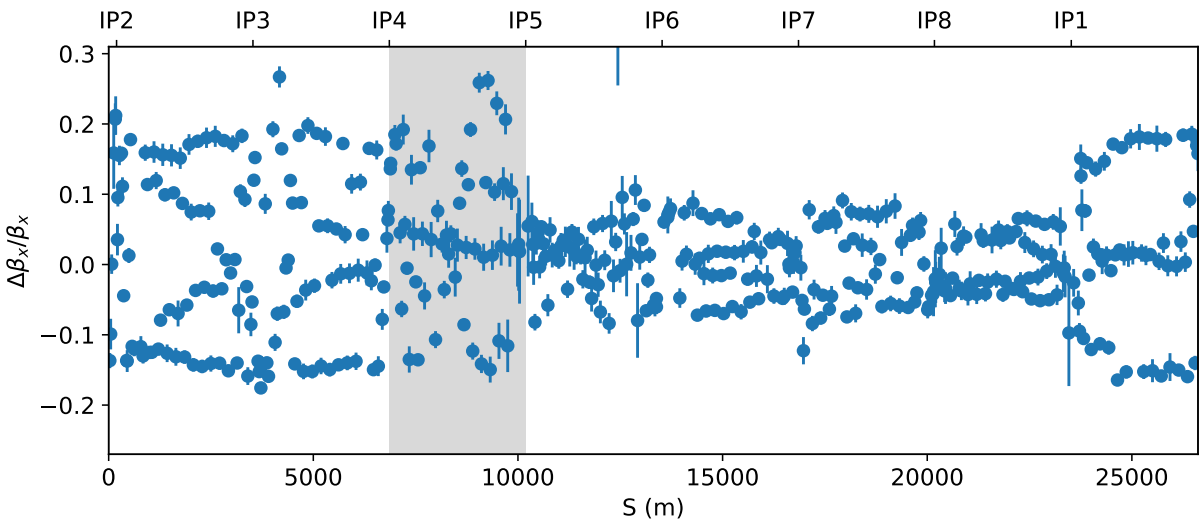

Figure 2.19: Horizontal β-beating measurement at flat 60/15 cm optics with local and global corrections applied, performed during the 2017 flat optics MD. The grey area shows the arc 45. In this area the corrections were unable to bring the β-beating below 24%.

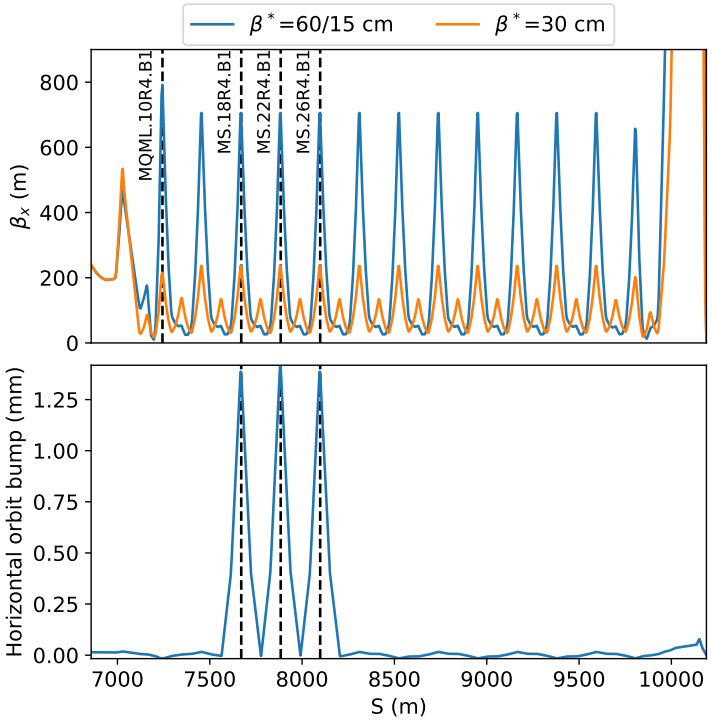

Figure 2.20: The top plot shows the design horizontal β-function from IP4 to IP5 for β^*=60/15 cm flat optics and for β^*=30 cm, the nominal 2018 optics. The ATS optics scheme increases the β-function in this arc by a factor of 4. The bottom plot shows the horizontal orbit bump implemented in the sextupoles to correct the optics via feed-down.

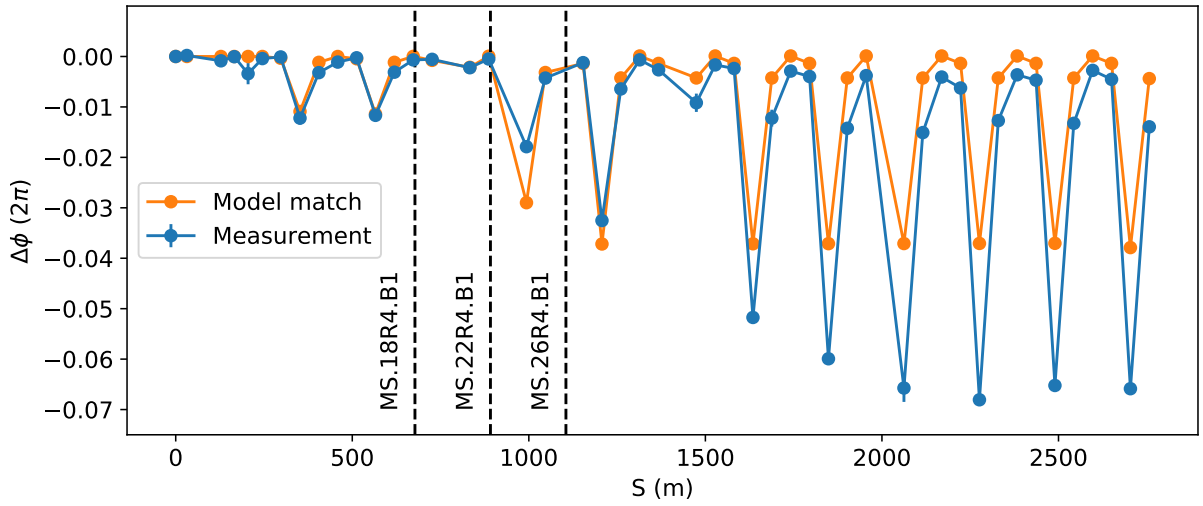

Figure 2.21: Horizontal betatron phase-advance deviation from the local model in arc 45. In blue the measurement and in orange the effect of the local correction with orbit bumps in sextupoles are shown. The sextupoles where the bump reaches its peak are indicated.

Magnet	Circuit	Trim [10^{-6}]
MQML.10R4.B1	RQ10.R4B1	20 m^{-2}
MCBH.16R4.B1	RCBH16.R4B1	8 rad
MCBH.20R4.B1	RCBH20.R4B1	16 rad
MCBH.24R4.B1	RCBH24.R4B1	16 rad
MCBH.28R4.B1	RCBH28.R4B1	8 rad

Table 2.3: Trim settings implemented to correct arc 45 at β^*=60/15 cm. It combines a trim on the Q10 on the right side of IR4 (MQML.10R4.B1) with an orbit bump created using the dipoles shown in the table (MCBH) that peaks in the main sextupoles MS.18R4.B1, MS.22R4.B1 and MS.26R4.B1 reaching 1.5 mm.

MS.26R4.B1 sextupole. To avoid this large bump, the correction was spread to the MS.18R4.B1 and MS.22R4.B1 sextupoles and a trim of the MQML.10R4.B1 individually-powered quadrupole, as shown in Fig. 2.20. The effect of the trim on the local model is shown in Fig. 2.21 in the orange line. Predictions from simulations showed that this fit corrected the error without large orbits or quadrupolar trims. In Table 2.3 the orbit correction and trim of MQML.10R4.B1 used to produce the knob are shown.

The effect of this correction on the global β-beating can be seen in Fig. 2.22. The large β-beating peak in arc 45 was reduced to the 5% level and the overall β-beating in the machine was also reduced by about 10%.

Orbit bumps have also been used in the same region to correct the spurious dispersion driven by the crossing scheme at the IPs [20]. This dispersion correction method is likely to conflict with the correction method presented here and therefore future continuation of these studies must take into account the interplay between these two correction methods.

2.8 Summary

Local corrections in the LHC interaction regions have traditionally been a manual tedious task. A new automatic local correction algorithm and tool have been developed to boost the correction

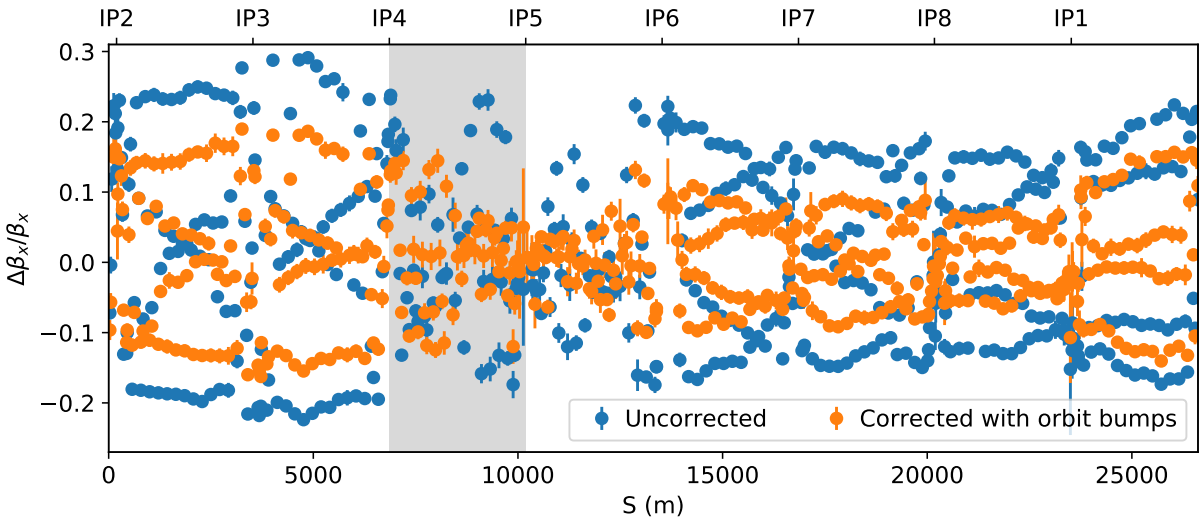

Figure 2.22: Measurement of the effect on the horizontal β-beating of Beam 1 of the correction with orbit bumps in sextupoles performed during the flat optics MD that took place in 2018. The previous global corrections calculated during 2017 were removed. The grey area is the region of the accelerator targeted by the correction. The 24% peak in arc 45 was reduced to about 5% and the overall β-beating around the machine was reduced about 10%.

quality and speed.

This algorithm has been used to perform Monte-Carlo simulations with the expected field and alignment errors of HL-LHC. It has been proven that the algorithm is able to correct down to the β^* measurement uncertainty level for both beams. This shows that the factor constraining the performance of the HL-LHC from the optics point of view is the accuracy of the measurement of the β^*. The automatic matching routine has also been used to establish a tolerance of ± 1 mrad on the maximum allowed tilts in the HL-LHC triplet quadrupoles and a waviness up to ± 5 mrad. This study also allowed a reduction of the integrated strength of the skew quadrupoles in IR1 and IR5, reducing the cost of the HL-LHC.

K-modulation has shown unreliable β^* measurements during Run 2, which further challenges the accuracy of this technique in HL-LHC with even lower β^*. An improvement of this technique using the LHC tune feedback system has been explored in experiments and simulations, but has been ruled out due to technical limitations and the cross-talk between the Q1 beta-beating and the arc tune quadrupoles.

The phase-advance across the IP has been proven, with a phase uncertainty of 0.3 mrad (for $\beta^* = 50\ cm$ optics), to allow a measurement of the β_w using the DOROS BPM system, but blind to waist displacements. Luminosity scans with waist shifts have been tested experimentally proving that they can be used to measure the waist position with good precision. This is the first time these scans are performed successfully in a machine like the LHC, where the safety of the machine is a concern limiting the waist shift range. These two techniques combined provide accurate measurements of the β_w and the waist position, resulting in the only approach to guarantee the HL-LHC performance and keep the imbalance between IP1 and IP5 within tolerable levels. HL-LHC will therefore require a totally different IR optics commissioning strategy than currently in the LHC.

It has been shown experimentally that the ATS optics scheme enhances local magnetic errors in the arcs, where local corrections are needed. The lack of individually powered correctors in those regions makes conventional local corrections with quadrupoles not viable. It has been shown experimentally that these local errors in the arcs can be corrected with orbit bumps in sextupoles via feed-down. This kind of corrections will be critical in HL-LHC that will operate with more ambitious ATS optics schemes and could cause local optics errors in the arcs to render the machine unsafe to operate.

In summary, the general HL-LHC optics correction strategy will need the new techniques experimentally demonstrated in this chapter which will significantly modify the traditional LHC commissioning flow as luminosity measurements will be required in intermediate stages.

Chapter 3

Flux jumps in future colliders

The challenge of reducing the beam size at the interaction points has a very strong impact on the aperture requirements of the final focus system of colliders. For HL–LHC, it is expected to have a β^* of down to 7.5 cm in certain configurations [18, 47]. To achieve this, the β-function across the triplet region rises above 40 km which corresponds to a r.m.s. beam size of about 3 mm, with the crossing angles producing an orbit in the region of about 15 mm.

To accommodate such beam sizes and orbits, the current LHC triplet quadrupoles with 70 mm aperture will be replaced with a new triplet with 150 mm aperture [66]. To keep the required magnetic gradient seen by the beam, this new quadrupole package is longer than the one in the LHC and uses Nb_3Sn superconductor technology, which allows to increase the magnetic gradient by about 50% [67]. This technology is also going to be used in operation from LHC Run 3 by replacing 4 dispersion suppressor dipoles with shorter ones that use the Nb_3Sn technology, to allow for the installation of additional collimators. The new technology is also expected to be used in all main dipoles and quadrupoles of the Future hadron-hadron Circular Collider (FCC-hh) [22].

Type I superconductors present superconductivity until they are subject to a magnetic field limit H_c, a point where the superconductivity is drastically destroyed. Nb_3Sn is a type II superconductor, and the superconductivity is not lost at a single critical magnetic field H_{c1}, but the material goes through a mixed state where the superconductivity is maintained until the magnetic field reaches a second critical magnetic field H_{c2} allowing for a significantly higher peak magnetic field. In this mixed state, the material does not show a complete Meissner effect [68] and the magnetic field penetrates the bulk of the material. In this region, small spots of normal-conducting material start to form and the supercurrents circle around them forming vortexes that induce a quantized unit of magnetic flux. These local vortexes are called *fluxoids*. The dynamics of fluxoids in the material can cause local heating, starting a chain reaction called *flux jump* and either the material is capable of dissipating the heat as it spreads or the superconductivity is broken producing a *quench* of the magnet. During the flux jump, the magnetic flux through the magnet is disturbed, affecting the magnetic field seen by the beam.

In this chapter the potential effect of these flux jumps on emittance (and orbit) will be studied based on magnetic measurement values. The results presented here ignore the effect of the presence of a transverse damper [69].

In Section 3.1, recent measurements of the flux jumps on the magnetic field of short prototypes of the 11 T dipole and of the HL–LHC triplets are presented with focus on flux jump duration and

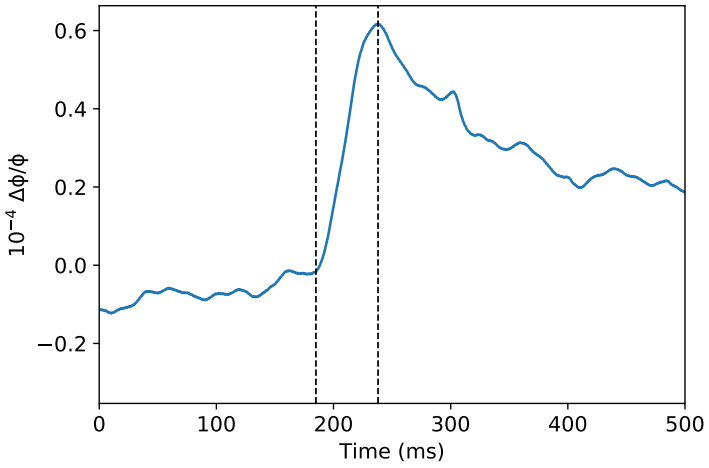

Figure 3.1: Strongest flux jump observed during the measurement of relative magnetic flux error in an 11 T dipole model. The dashed lines limit the fast rise up time of the flux jump.

magnitude. In Section 3.2 the mathematical approach used in this study to perform simulations of the effect of the flux jumps is presented. In Section 3.3, these simulations are discussed for the HL-LHC triplet with its possible impact on the luminosity of the machine. Section 3.4 shows that the flux jumps of the 11 T dipoles will have a negligible impact on performance. In Section 3.5 a similar analysis is performed for the FCC-hh main dipoles.

3.1 Flux jump measurements

Flux jumps measurements have been performed at CERN on prototypes of the 11 Tesla dipoles and of the MQXF quadrupoles [70, 71].

The effect of the flux jumps on the magnetic field as seen by the beam can be separated in two parts: the flux jump causing a change of inductance of the magnet [71] and thus directly the magnetic field, and the reaction of the feedback current-regulation loop of the power supply to the change of inductance, which can also be seen as a change of voltage across the magnet.

3.1.1 Error in the magnetic field

The effect of the flux jumps on the field itself has been measured on the MBHSP109 prototype of the 11 T dipole [70]. These measurements were performed by ramping the magnet at the nominal ramp rate (10 A/s) and by measuring both the current error (ΔI) and the magnetic flux error inside the magnet ($\Delta\phi/\phi$), both relative to their nominal values along the current ramp. The difference between these two values ($\Delta\phi/\phi$ - ΔI/I) measures the error in magnetic flux without the component coming from the error on the current. This measurement showed that the flux jumps happen mainly during the first half of the energy ramp of the magnet, between 2 and 3 kA (corresponding to about 1.2 to 1.8 TeV of beam energy) at a rate of about 4.4 flux jumps per second (at the nominal ramp rate). In Fig. 3.1, the relative magnetic flux error is shown for the strongest flux jump observed during the measurement. This displays the typical signature of a flux jump, consisting in a fast rise of the magnetic flux with a slower recovery towards the nominal value.

A statistical analysis is performed for the 145 flux jumps that are clearly distinguishable from the noise, Fig. 3.2. For each flux jump the rise time and the change of magnetic flux are recorded.

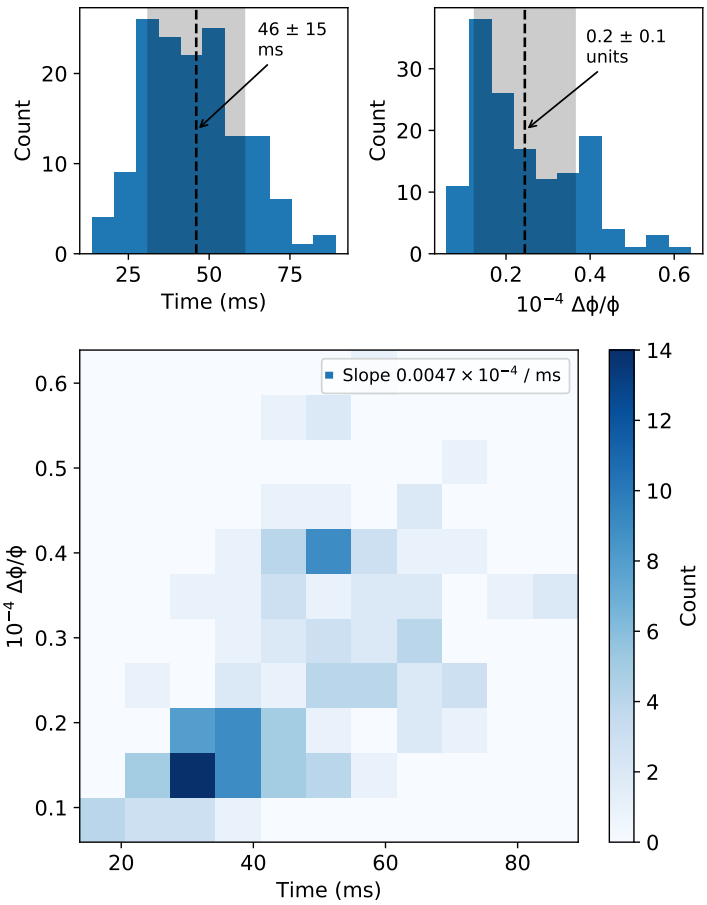

Figure 3.2: Statistics of 145 manually selected flux jumps during the measurement of the magnetic flux error in the MBHSP109 model of the 11 T dipole. The top left plot shows the distribution of the rise times of the selected flux jumps. The top right plot shows the distribution of the magnetic flux change that the flux jumps produce. In the bottom plot the distribution of magnetic flux error versus rise time is shown.

The average rise time of the flux jumps is 46 ± 15 ms, or 506 ± 165 turns at the LHC revolution frequency and the average relative error in flux is $(0.2 \pm 0.1) \cdot 10^{-4}$. There is an approximately linear relation between the length of the flux jumps and the relative flux error it produces, with a slope of 0.0047×10^{-4}/ms, suggesting that the slope of the flux variation is more or less constant.

3.1.2 Reaction of the feedback regulation loop

Power converters supply particle accelerator magnets with very high-precision current thanks to a dedicated feedback regulation loop. Such feedback loop is often composed of nested ones: the external one regulates the current and the internal one controls the voltage. Both loops react to flux jumps hence introducing an additional error in the current and therefore in the magnetic field.

The internal regulation loop measures the voltage across a set of magnets and reacts to the voltage changes produced by the flux jumps, introducing an additional error in the current and therefore in the magnetic field. Measurements of the voltage across the MQXFS4b model of the HL–LHC triplet quadrupoles have been performed and a simplified model of the effect able to match this measurement (by matching simulated and measured voltage spectra) has been developed. Such a model allows to predict the reaction of a simulated HL–LHC triplet power converter, ignoring the effect of the trim circuits. A realistic configuration of the feedback regulation loop, whose

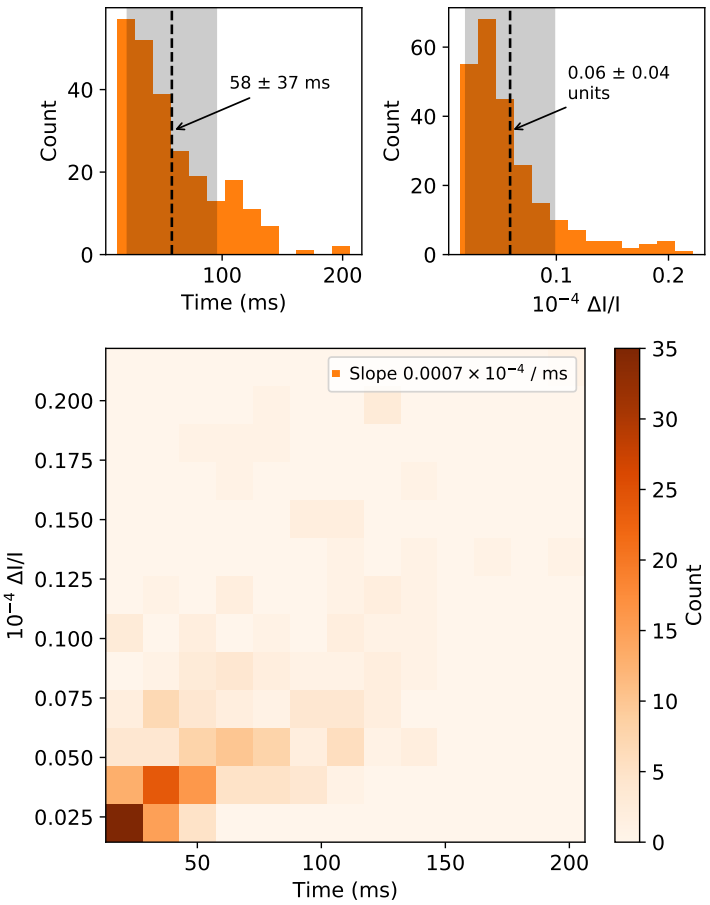

Figure 3.3: Statistics of the simulation of the current error produced by the regulation loop. The top left plot shows the distribution of the rise time of the current error. The top right plot shows the distribution of the total magnitude of the current error. In the bottom plot, the distribution of the length of the current errors versus the current error magnitude is shown.

bandwidth is limited to a few hertz, has been assumed for this study. Further details of these measurements and simulations are given in [71] and [72]. These measurements, and therefore the simulation results, should be considered conservative as they were performed at a ramp rate of 51 A/s, while the nominal ramp rate for HL-LHC triplet quadrupole magnets is 14.6 A/s and the flux jumps are likely to happen more often for faster current changes.

Figure 3.3 shows a manual selection of 244 flux jumps (again, those visible above the noise level) as produced by the *inductance jump model* presented in [71]. As before, the rise time of the error and the total error in current produced during the jump are considered. The figure demonstrates how this effect is in general slower than the magnetic field jump, at 58 ± 37 ms in length or 638 ± 407 turns at the LHC revolution frequency. This effect is in general a factor 4 weaker than the direct effect of the magnetic flux, at $(0.06 \pm 0.04) \cdot 10^{-4}$. As the heat map also shows in this case, there is an approximately linear relation between the current error and the duration of the flux jump.

The conservative limit of the error bars presented in this section (instead of the average value) will be used in subsequent simulations, for both the duration and the strength of the jumps. The reference values used for the flux jump effect on the field itself will therefore be $0.3 \cdot 10^{-4}$ of field error and 31 ms of rise time. For the reaction of the regulation loop, $0.1 \cdot 10^{-4}$ relative field error

and 21 ms of rise time will be used.

Additionally, flux jumps size is assumed equal for dipole and quadrupole magnets for now. Future measurements on the actual magnets (instead of prototypes) will define the correct values.

3.2 Emittance growth

As the beam traverses the triplet quadrupoles off-center due to crossing angle and separation bumps, the beam perceives both a dipolar kick (via feed-down) and a quadrupolar disturbance, i.e. a quadrupolar deformation of the phase space.

3.2.1 Dipolar effect

The dipolar case can be evaluated by computing the single-particle emittance change across the dipoles or quadrupoles producing flux jumps. If Δy and $\Delta y'$ are the offsets w.r.t. the closed orbit, the geometric emittance growth compared with the reference particle can be written, from the expression of the beam ellipse in Eq. (1.19), as:

$$\Delta\epsilon_{\text{geom}} = \gamma(s)\Delta y^2 + 2\alpha(s)\Delta y\Delta y' + \beta(s)\Delta y'^2, \tag{3.1}$$

where α, β and γ are the Twiss parameters and s the longitudinal position.

In the case of a dipole magnet and given the relative magnitude of the change of the magnetic field produced by the flux jumps studied in 3.1, an absolute change $\Delta\theta$ of its bending angle can be obtained. If a quadrupole is traversed with an closed orbit x_{co} in the case of an error ΔkL of its integrated field a dipole effect is produced via feed-down and the equivalent bending angle is $\Delta\theta = x_{co}\Delta kL$.

In the simplest case of a flux-jump in a single magnet, the resulting geometric emittance growth is:

$$\Delta\epsilon_{geom} = \beta_d\Delta\theta^2, \tag{3.2}$$

where β_d is the β-function in the magnet.

The normalised one-turn rise relative emittance growth is then $\Delta\epsilon_1/\epsilon = \gamma_{rel}\Delta\epsilon_{\text{geom}}/\epsilon$, the design normalised emittance. And again for the simplest case of a single magnet field error, the normalised one-turn rise emittance growth results in

$$\frac{\Delta\epsilon_1}{\epsilon} = \frac{\beta_d\Delta\theta^2\gamma_{rel}}{\epsilon}. \tag{3.3}$$

For more complex cases where the error appears in several magnets simultaneously, MAD-X [34] can be used to compute the difference in orbit and divergence from the nominal model.

The flux jump evolution with time, as can be seen in Fig. 3.1, resembles a linear ramp with a slower decay. A simplified model of the flux jumps used here is shown in Fig. 3.4.

To compute the emittance growth after a certain number of turns we follow the derivations for the motion during an AC-dipole excitation described in [8]. Considering that the amplitude of the AC-dipole increases step-wise every N turns, the periods with constant amplitude can be labelled

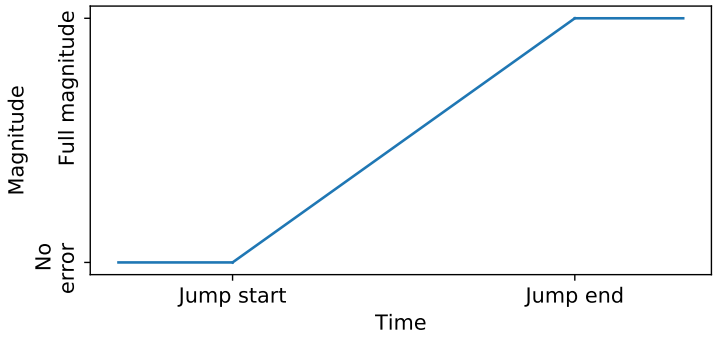

Figure 3.4: Simplified flux jump event shape. It is modelled as a linear ramp towards the full amplitude of the jump. The duration of the ramp is on average 46 ms (506 turns in the LHC) for the flux jump on the magnetic field itself and 58 ms (638 turns in the LHC) for the reaction of the regulation loop.

as n and the turn-by-turn motion is described as:

$$\hat{x}(T) - i\hat{p}_x(T) = z^{(n)} e^{i2\pi Q_x T} + \delta_-^{(n)} e^{i2\pi Q_D T} - \delta_+^{(n)} e^{-i2\pi Q_D T} \tag{3.4}$$

where $\hat{x}$ and $\hat{p}$ are the linear normalised coordinates related to those introduced in Eq.(1.15) and Eq.(1.16) by:

$$\begin{pmatrix} \hat{x} \\ \hat{p_x} \end{pmatrix} = \begin{pmatrix} \frac{1}{\sqrt{\beta}} & 0 \\ \frac{\alpha}{\sqrt{\beta}} & \sqrt{\beta} \end{pmatrix} \begin{pmatrix} x \\ x' \end{pmatrix}, \tag{3.5}$$

T is the turn number, $z^{(n)}$ is a complex quantity that contains the amplitude and phase of the natural oscillations and $\delta_\pm^{(n)}$ describes the motion induced by the modulation of the AC-dipole. In [8] a modulation with tune Q_D is assumed on top of the linear increase of the kick. In our simpler case the modulation tune is zero, $Q_D = 0$ the quantity $\delta_\pm = \delta_\pm^{(n+1)} - \delta_\pm^{(n)}$ is equal to

$$\delta_\pm = \pm \frac{\sqrt{\Delta\epsilon_1}}{4\sin(\pi Q)}\ , \tag{3.6}$$

with Q the betatron tune. The continuity condition on the particle position between the contiguous periods n and $n+1$ can be imposed as:

$$z^{(n)} e^{i2\pi QN(n+1)} = z^{(n+1)} e^{i2\pi QN(n+1)} + \delta_- - \delta_+, \tag{3.7}$$

from which the following relation between $z^{(n+1)}$ and $z^{(n)}$ can be obtained

$$z^{(n+1)} = z^{(n)} + 2\delta_+ e^{-i2\pi QN(n+1)}, \tag{3.8}$$

Summing successive terms of this equation we obtain:

$$z^{(n+1)} = z^{(0)} + 2\delta_+ \sum_{j=0}^{n} e^{-i2\pi QN(n+1)}. \tag{3.9}$$

Assuming $z^{(0)} = 0$, the oscillation amplitude in the normalized coordinate after a linear ramp of N turns according to Eq. (8) in [8] becomes

$$|z^{(N)}| = 2\delta_+ \frac{\sin(\pi Q N)}{N \sin(\pi Q)} \ . \tag{3.10}$$

Therefore the total relative emittance change after a rise time of N turns is given by

$$\frac{\Delta\epsilon(N)}{\epsilon} = \frac{M\ \overline{\Delta\epsilon_1/\epsilon}\sin^2(N\pi Q)}{4N^2\sin^4(\pi Q)}, \tag{3.11}$$

where $\overline{\Delta\epsilon_1/\epsilon}$ is the average relative one-turn emittance growth over M magnets. For the sake of simplicity, all the quadrupoles of the triplet will be assumed equally likely to produce a flux jump. This formula oscillates with the number of turns and to stay in the worst-case scenario an envelope of the function can be used:

$$\frac{\Delta\epsilon(N)}{\epsilon} \leq \frac{M\ \overline{\Delta\epsilon_1/\epsilon}}{4N^2\sin^4(\pi Q)} \ . \tag{3.12}$$

The model of the flux jumps used here (Fig. 3.4) neglects the effect of the slower recovery of the field which is significantly more adiabatic.

3.2.2 Quadrupolar effect

The fast current change in the quadrupoles also induces a quadrupolar deformation of the phase space that will also lead to emittance growth. This quadrupole effect can be written as a mismatch of the α-function after a quadrupolar kick. Using the definition of $\hat{p}_x$ in linearly normalised coordinates given by Eq. (3.5):

$$\hat{p}_x = \beta x' + \alpha x \ , \tag{3.13}$$

the quadrupole kick in $\hat{p}_x$ can be written as:

$$\Delta\hat{p}_x = \beta_k \Delta x' = \beta_k \Delta k L\, x \ , \tag{3.14}$$

with β_k being the β-function at the quadrupole and ΔkL the integrated quadrupolar error. This can then be written as a transformation of the α-function:

$$\begin{aligned} \hat{p}_x &\rightarrow \hat{p}_x + \Delta\hat{p}_x = \beta x' + x(\alpha + \beta_k \Delta k L) \ , \\ \alpha &\rightarrow \alpha + \beta_k \Delta k L \ . \end{aligned} \tag{3.15}$$

The emittance growth after an optics mismatch follows the equation [7]:

$$1 + \frac{\Delta\epsilon}{\epsilon} = \frac{1}{2}\left[\frac{\beta_n}{\beta_k} + \frac{\beta_k}{\beta_n} + \left(\frac{\alpha_k}{\beta_k} - \frac{\alpha_n}{\beta_n}\right)^2 \beta_n\beta_k\right] \ , \tag{3.16}$$

with β_n, α_n the design β and α functions and β_k, α_k the perturbed β and α functions. In this case we only transform the α-function so $\beta_k = \beta_n$ and $\alpha_k = \alpha_n + \beta_k \Delta k L$. Then, simplifying the equation and writing it in relative emittance growth terms:

$$\frac{\Delta\epsilon}{\epsilon} = \frac{(\beta_k \Delta k L)^2}{2} \ . \tag{3.17}$$

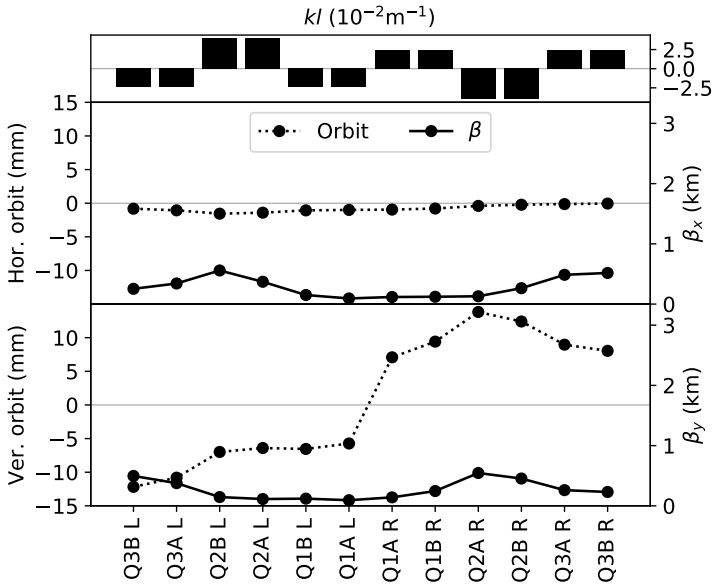

Figure 3.5: Integrated quadrupolar strength (kl), orbit and β-functions across the triplet of IR1 with injection optics.

This value is about $\frac{\Delta\epsilon}{\epsilon} \approx 7.5 \cdot 10^{-6}$ for the quadrupole with highest β-function (3324 m) at β^*=1 m, two orders of magnitude below the effect produced by the dipolar kick for the HL–LHC triplet and thus will be ignored. The β_k^2 term is likely to enhance the effect of the quadrupolar deformation of the beam shape in future machines, if the flux jumps are present in regimes where the β-function in the quadrupoles reaches some tens of kilometres.

In conclusion, in this section a general theoretical framework that allows to compute the effect of flux jumps on the beam emittance has been developed. A formula has been derived that relates the change of the bending angle produced by a one turn rise flux jump to the emittance growth, both in dipoles and in the dipole effect of quadrupoles via feed-down. This relation has also been obtained for the effect produced in the focusing strength of quadrupoles, but has been found to be significantly weaker than the dipole effect, at least for the HL-LHC parameters. Finally, a general formula that relates then one turn rise flux-jumps to a linear rise model over several turns has been derived, providing a full theoretical model of flux-jumps effect on the emittance. In the following sections, this framework will be applied to the HL-LHC triplet, the LHC 11 T dipoles and the FCC-hh main dipoles, as they use or are going to use the Nb_3Sn technology.

3.3 The HL–LHC triplet

As the combined ramp and squeeze steps for HL–LHC are not yet defined in detail, in this study a baseline scenario of injection optics (β^*=6 m) at 450 GeV beam energy and a worst-case scenario of β^*=1 m optics at 3200 GeV are assumed. For reference, in Fig. 3.5 and Fig. 3.6 the β-functions and orbit across the triplet magnets of IR1 for the two considered scenarios are shown. The HL–LHC triplets in IR1 and IR5 are identical with the crossing angles in opposite planes. Here, a vertical crossing in IP1 is considered. Having horizontal crossing in IP1 and vertical in IP5 is under consideration for HL–LHC [73].

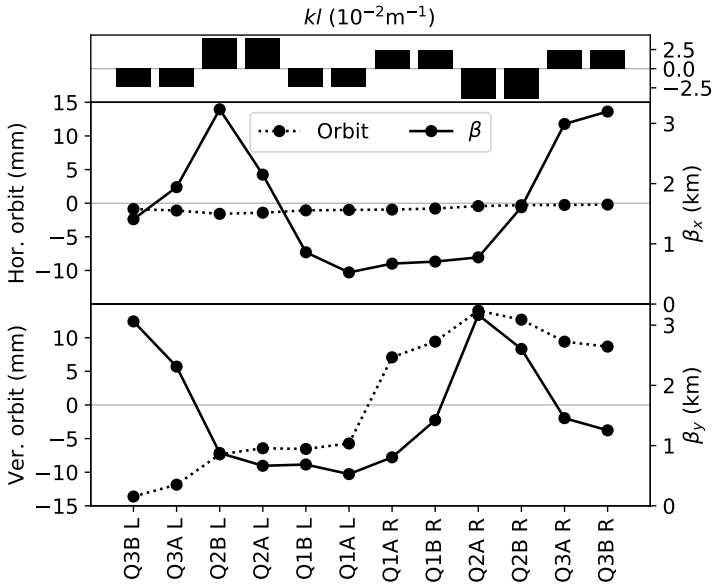

Figure 3.6: Integrated quadrupolar strength (kl), orbit and β-functions across the triplet of IR1 with β^*=1m optics.

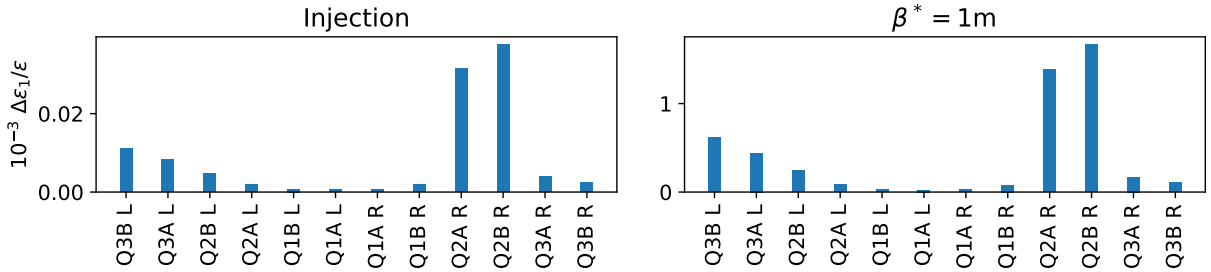

Figure 3.7: Relative emittance growth produced by one-turn relative change of $0.3 \cdot 10^{-4}$ in the magnetic field of the quadrupoles of the HL-LHC triplet at injection (left) and 1 m optics (right) optics. Notice the difference on the vertical axis scale. The values follow the expected dependency on orbit and β-function.

3.3.1 Effect on the emittance

For a one-turn flux jump, MAD-X simulations of the effect of a field disturbance of every magnet in the triplet is used to compute the beam position change and thus the normalised one-turn emittance growth $\Delta\epsilon_1/\epsilon$ relative to the normalised emittance of the HL-LHC at injection $\epsilon = \epsilon_{\text{HL-LHC}} = 1.7\ \mu m$ [73].

The one-turn emittance growth produced by a flux jump of $0.3 \cdot 10^{-4}$ of the nominal field of each of the magnets of the triplet is shown in Fig. 3.7, with the expected dependency on the β-function and orbit in the quadrupoles.

Similarly, the impact of the reaction of the regulation loop on the emittance can be calculated. As already discussed, only the reaction of the main circuit of the triplet is considered here as it is unclear how the flux jumps will affect the different circuits of the triplet.

In Fig. 3.8 the relative emittance growth produced by a one-turn change of $0.1 \cdot 10^{-4}$ on the magnetic field of the triplets at the left and right of IP1 is shown. This effect is significantly smaller than

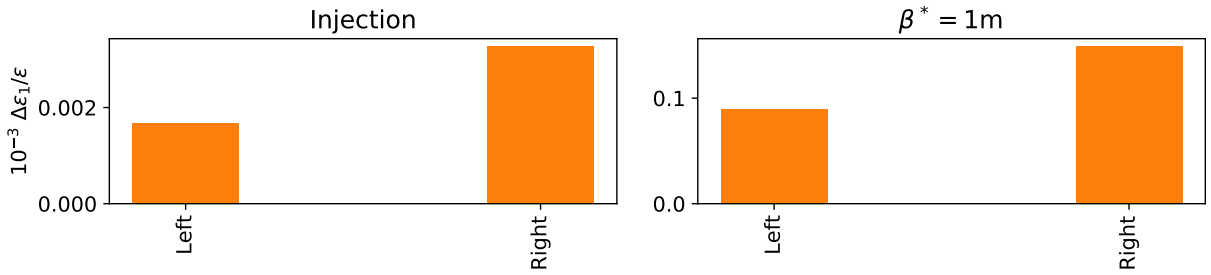

Figure 3.8: Relative emittance growth produced by one-turn flux jumps causing a reaction of the regulation loop of the main circuit of each triplet at injection (left) and 1 m optics (right) optics, causing a relative strength change of $0.1 \cdot 10^{-4}$. Notice the difference on the vertical axis scale. It should be noted how this effect is significantly smaller than that produced by the flux jump in the field itself.

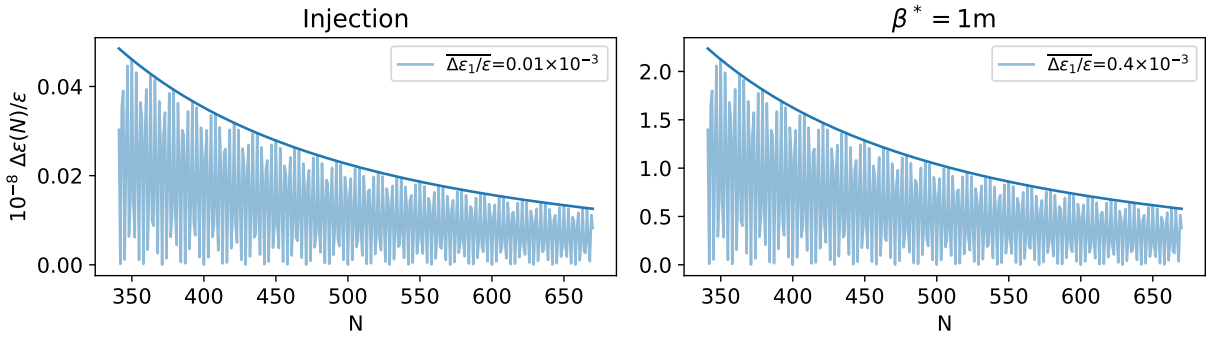

Figure 3.9: Decay of the emittance growth with the length in turns (N) of the flux jumps effect on the magnetic flux itself, with an initial $\overline{\Delta\epsilon_1/\epsilon}$ of $8.8 \cdot 10^{-6}$ for injection and $4 \cdot 10^{-4}$ for β^*=1 m (average of the values in Fig. 3.7). The clearer line shows the oscillating decay as shown on Eq. (3.11) and the darker line shows the pessimistic envelope described in Eq. (3.12).

that produced by the flux jump on the magnetic field of each individual quadrupole, as already shown in the measurements.

Figure 3.9 shows the results of Eqs. (3.11) and (3.12) for the emittance growth produced by the flux jumps in the magnetic flux itself for a range of rise times of 46 ± 15 ms (341 to 670 turns) taken from the measurements shown in Fig. 3.2.

Same results for the reaction of the regulation loop are shown in Fig. 3.10 for a range of rise times 58 ± 37 ms (231 to 1044 turns) as was presented in Fig 3.3.

For the worst-case scenario i.e. the shortest flux jumps using Eq. (3.12), an upper bound of the emittance blowup caused in a 20 minutes ramp can be given. Table 3.1 and Table 3.2 show the number of flux jumps needed to produce a 1% emittance growth and the emittance growth that would be produced after a 20 minutes ramp at a flux jump rate of 4.4 events/s, for the flux jumps effect in the magnetic field itself and for the reaction of the regulation loop respectively. These results make the assumption that the flux jumps are equally likely and behave in the same way during the whole ramp, which is again pessimistic.

Even after these pessimistic assumptions, the worst-case emittance growth during the ramp is about a 0.1‰ assuming that IR1 and IR5 are equivalent, producing emittance growths in the vertical and horizontal planes respectively.

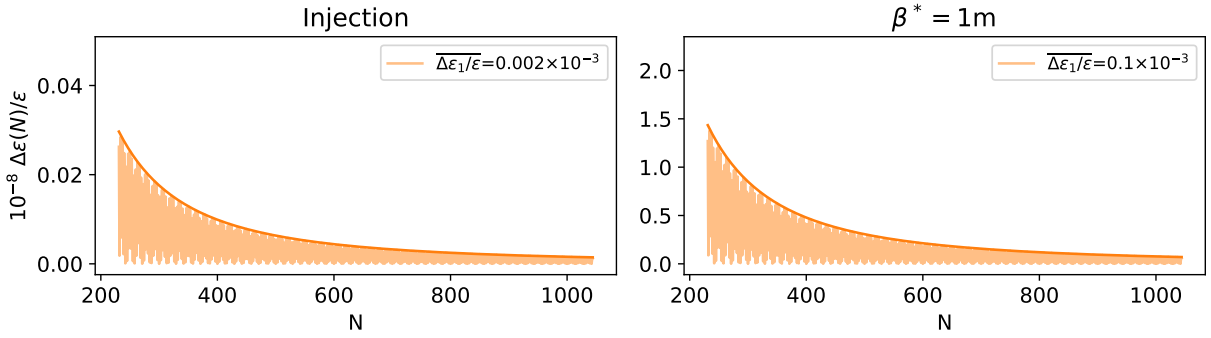

Figure 3.10: Same results as in Fig. 3.9 but for the reaction of the regulation loop. In this case the initial $\overline{\Delta\epsilon_1/\epsilon}$ (average of the values in Fig. 3.8) is $2.5 \cdot 10^{-6}$ for injection and $1.2 \cdot 10^{-4}$ for β^*=1 m, factor 4 lower than for the previous effect. The larger spread of lengths causes the worst-case scenario of this effect to be about 60% of the direct effect on the magnetic flux.

Optics	**Plane**	**N. of events for 1% $\Delta\epsilon/\epsilon$ [10^5]**	**$\Delta\epsilon/\epsilon$ in 20 min at 4.4 jumps/s [‰]**
Injection	Hor.	14238	0.00004
	Ver.	206	0.00256
β^*=1 m	Hor.	324	0.00163
	Ver.	4	0.11815

Table 3.1: Number of flux jumps in the magnetic field needed to get a 1% emittance blowup and emittance growth in 20 minutes (approximate duration of an energy ramp) at a rate of 4.4 jumps/s rate for injection optics and β^*=1 m.

Optics	**Plane**	**N. of events for 1% $\Delta\epsilon/\epsilon$ [10^5]**	**$\Delta\epsilon/\epsilon$ in 20 min at 4.4 jumps/s [‰]**
Injection	Hor.	26685	0.00002
	Ver.	337	0.00157
β^*=1 m	Hor.	574	0.00092
	Ver.	7	0.07572

Table 3.2: Number of reactions of the regulation loop to the flux jumps needed to get a 1% emittance blowup and emittance growth in 20 minutes (approximate duration of an energy ramp) at a 4.4 events/s rate for injection optics and β^*=1 m.

Optics	Magnet	Optics sensitivity $[\sigma/10^{-4}]$	Jump-induced rms orbit $[10^{-3}\sigma]$
Injection	Q1	< 0.01	< 2
	Q2	0.01	2
	Q3	< 0.01	< 2
	Q1–Q3	0.01	2
β^*=15 cm	Q1	0.06	12
	Q2	0.28	56
	Q3	0.18	36
	Q1–Q3	0.48	96
β^*=1 m	Q1	0.02	4
	Q2	0.11	22
	Q3	0.06	12
	Q1–Q3	0.11	22

Table 3.3: R.m.s. closed orbit variation at HL–LHC TCPs under the effect of the expected flux jumps for each half quadrupole composing the triplet (Q1; Q2; Q3) and for a whole triplet (Q1–Q3) computed in units of beam sigma. The optics sensitivity in units of beam sigma per unit of magnetic field change is also reported.

In view of these results, it is safe to assume that the flux jumps will not have a harming effect on the emittance of HL-LHC.

3.3.2 Effect on the orbit and tune noise

Flux jumps in the HL-LHC triplet will produce a dipolar kick as seen before and therefore will affect the beam orbit. The main concern is the orbit variation at the Primary Collimators (TCPs) which could trigger a beam dump by the machine protection system, and therefore a considerable loss of precious time for physics. Given the slow dynamics of the flux jump with respect to the revolution frequency, a fair approximation is to assume that a flux jump induces a *closed orbit* variation as if it would be generated by a constant kick equal to the magnitude of the flux jump. Different machine optics have a different sensitivity to kicks generated in the triplet, where the β functions vary considerably along the cycle. The two extreme cases considered here are the injection optics and a fully squeezed round optics (15 cm β^*), together with the intermediate value of 1 m β^* corresponding to the end of the ramp and squeeze scheme. For all optics it is assumed a 295 μrad half crossing angle horizontal in IP1 and vertical in IP5. Table 3.3 lists the biggest (with respect to plane and IP) orbit variation at the TCPs under a field error (in units of 10^{-4}) of each half-quadrupole in the triplet and for a whole triplet (Q1-Q3). The values are given in beam sigma for the nominal normalised emittance of 2 5μm at 450 GeV (for the injection optics) and 7 TeV (for the 1 m and 15 cm β^* optics). This, multiplied by expected amplitude of the flux jumps of 0.2 units of 10^{-4}, gives the expected flux-jump-induced orbit variation at the TCPs, also reported in Table 3.3. Flux jumps are expected to appear more likely at low energy, i.e. for injection-like optics, and they should stop once reached the top energy, i.e. once the optics has normally reached 1 m β^*. For those two optics, and similarly for any intermediate one, the impact of a single flux jump in any triplet half quadrupole is unlikely to give an orbit jump at the primary collimators able to trigger a beam dump by the machine protection system. The worst case scenario when two flux jumps of 0.2 unit amplitude occurs at the same time on the two halves of Q2 would correspond to an orbit jump at the collimators of about 4% of beam sigma. For comparison, in the unrealistic case where

	Injection	$\beta^* = 1\ m$
$< \lvert\Delta Q\rvert >[10^{-5}]$	1.3	7.8

Table 3.4: Average absolute tune error produced produced by flux jumps in each quadrupole of IR1 and IR5.

Optics	**Optics sensitivity** $[\sigma/10^{-4}]$	**Jump-induced rms orbit** $[10^{-3}\sigma]$
Injection	0.02	4
β^***=15 cm**	0.07	14
β^***=1 m**	0.07	14

Table 3.5: R.m.s. closed orbit variation at HL–LHC TCPs under the effect of the expected flux jumps at the 11 T dipoles computed in units of beam sigma. The optics sensitivity in units of beam sigma per unit of magnetic field change is also reported.

a 0.2 unit flux jump occurs at the fully squeezed 15 cm β^* optics on a Q2 half magnet, the r.m.s. orbit variation at the primary collimators would be of 5.6% of beam sigma. Such a fluctuation is considered to produce noticeable beam losses at collimators, but still unlikely to trigger a beam dump. Therefore, the orbit variation induced by a flux jumps is expected to be harmless.

As for the tune noise, the average absolute effect per quadrupole can be calculated from Eq. (1.28) as:

$$< |\Delta Q| >= \frac{1}{4\pi M} \sum_{i=1}^{M} |\beta_i \Delta k_i L_i|, \tag{3.18}$$

where β_i is the β-function at the i$^{\text{th}}$ quadrupole, $\Delta k_i L_i$ the integrated quadrupolar field error at the i$^{\text{th}}$ quadrupole and M the number of quadrupoles producing errors. Assuming as before a $\Delta k/k$ of $0.3 \cdot 10^{-4}$, relative to the design strength of the quadrupoles, the effect for injection and β^*=1 m optics for the tune of both planes is shown in Table 3.4. These number on the order of 10^{-5} are on the level of the tune noise produced by the power supply current stability [74] and therefore they will have no harmful effect in the HL-LHC.

3.4 The 11 T dipoles

During Long Shutdown 2 of the LHC, 4 dipoles (2 per side) using the Nb_3Sn technology are planned to be installed in the dispersion suppression collimators in IR7 and to be used operationally during Run 3.

The effect of flux jumps in the dipolar field on the emittance as a one-turn kick is described by Eq. (3.3). The β-function across these dipoles does not change with different optics configurations, staying about 30 m. At 3.2 TeV energy, this one-turn emittance growth is $\Delta\epsilon_1/\epsilon = 3 \cdot 10^{-4}$ one order of magnitude lower than the effect of the HL-LHC triplet, together with the fact that there are only four 11 T dipoles per beam against 12 triplet quadrupoles in HL-LHC. Therefore, it can be concluded that the effect of flux jumps in the 11 T dipoles in the emittance will also be negligible.

As for the orbit noise, an analysis similar to the one in the case of the triplet magnets can be carried out. Table 3.5 lists the optics sensitivity and expected closed orbit variation at the primary collimators under the effect of the expected flux jumps in the 11 T dipoles. As for the triplet

case, the probability of inducing a beam dump with such an orbit oscillation is considered to be negligible, even for the fully squeezed optics case.

3.5 Flux jumps in the FCC-hh

The theory developed in Sec. 3.2 has also been applied to the FCC-hh (Future Circular hadron-hadron Collider) [22] as it will use the Nb_3Sn magnet technology in all the 4672 main bending dipoles. As the nominal dipole current in the FCC-hh will be 11.2 kA [22], the 2-3 kA region (where most of the flux jump activity happens) will correspond in the FCC-hh to a beam energy of about 8.9-13.4 TeV. Therefore, similarly to the case studied for the HL–LHC, this region of high flux jump activity appears in the early energy ramp.

Studying the FCC dipoles the same way as in the previous section, it is found that at injection optics and energy (3.3 TeV) the average one-turn emittance growth per dipole is about $4.6 \cdot 10^{-4}$ relative to the FCC design normalised emittance of 2.2 μm. This effect is greatly amplified by the large amount of dipoles producing flux jumps (4672 compared with 12 quadrupoles in the HL–LHC) and the smaller revolution frequency of the FCC which will cause the flux jumps to take less turns to rise to their full amplitude (92 turns for a 30 ms long flux jump).

The result of Eq. (3.12) at injection energy and optics raises to $\Delta\epsilon_{\max}/\epsilon = 1.3 \cdot 10^{-4}$, being 75 flux jumps per individual dipole enough to produce a 1% emittance growth. Assuming the same event rate (4.4 events/s) and ramp length of HL–LHC (20 minutes), the flux jumps during the FCC energy ramp could cause about a 70% emittance growth. To these results will have to be added the effect of any quadrupole being traversed with a non-zero orbit, as described in previous sections.

Nevertheless, to achieve the high field density needed in the FCC magnets, the use of Artificial Pinning Centers (APC) is expected. By introducing ZrO_3 particles (the APCs) into the Nb_3Sn strands, the Nb_3Sn grain size is effectively reduced, allowing for almost a factor 2 increase on the magnet critical current density. APCs have been observed to suppress the effect of flux jumps at low fields due to reduced low-field magnetizations, as a result of shift in pinning force curve peak to higher fields [75, 76].

In summary, in FCC-hh the effect of the flux jumps is likely to have an important impact on the emittance of the beam during the energy ramp. Nevertheless, FCC-hh is going to present a much stronger synchrotron radiation damping than LHC, thus, the interplay between the flux jumps emittance growth and the radiation damping, together with the effect of APCs, should be carefully studied in the future. Also, in view of these results, the impact on all beam parameters of the flux jumps in both dipoles and quadrupoles should be carefully assessed for FCC-hh.

3.6 Summary

The effect of the flux jumps in the HL–LHC triplet quadrupoles and 11 T dipoles has been studied. Measurements of the flux jump effect in the magnetic flux of the prototype of the 11 T dipole have shown a relative magnetic flux error of $(0.2 \pm 0.1) \cdot 10^{-4}$ with a rise time of 46 ± 15 seconds (corresponding to 506 ± 165 turns) and have been extrapolated to the HL-LHC triplet. Even in the pessimistic scenario, up to $4 \cdot 10^5$ flux jumps per quadrupole would be required to produce a 1% emittance growth. At a rate of 4.4 flux jumps per second, in a ramp of 20 minutes the emittance

growth will be below 0.1‰. The reaction of the regulation loop has been found weaker than the effect on the magnetic flux itself. Therefore, the flux jumps effect on emittance and orbit should not be considered harmful in the HL-LHC. The 11 T dipoles that are planned to be installed in the LHC during Long Shutdown 2 will also use the Nb_3Sn technology. The effect of flux jumps in these dipoles on emittance is much smaller than the effect of the HL-LHC triplet quadrupoles, due to the small horizontal β-function in the region, and can therefore be neglected too. For the same reason, also the effect on closed orbit variation and consequent possibility of causing a beam dump can be neglected.

However, for the FCC-hh main dipoles this effect cannot be neglected as the large number of main dipoles with Nb_3Sn technology and the lower revolution frequency are likely to increase the effect of flux jumps to produce about a 70% emittance growth during the energy ramp, ignoring the flux jumps in the quadrupoles and the effect of the radiation damping.

Therefore, flux jumps in the magnets using Nb_3Sn technology are not a concern for LHC and HL–LHC, but their effect should be carefully taken into account for future high-energy colliders.

Chapter 4

OMC software development

A significant part of the results in this thesis has required the implementation of new features and improvements in the Optics Measurements and Corrections (OMC) software suite [77, 78, 79].

Though this set of tools are used by the OMC team mainly to measure and correct the optics of the LHC, it has also been applied to other machines. The analysis tools are collected under a repository (Beta-Beat.src [80]) which contains several different stand-alone codes with a total of about 48000 lines of code [79]. The developments within this thesis have focused on the following codes:

- Drive [81] / SUSSIX [23]: a historically used tool for harmonic analysis of the turn-by-turn data. SUSSIX is a FORTRAN [82] program that implements the Laskar [83] method that will be introduced in Sec. 4.2. Drive is a wrapper of SUSSIX in C++ [84] whose task is to read the turn-by-turn data, run SUSSIX for each BPM and write the output.
- Harpy: An alternative to Drive/SUSSIX written in Python [85] (see Sec. 4.2).
- GetLLM: A collection of Python routines that takes the harmonic analysis output and reconstructs the optics of the machine, providing the phase advances, β-functions, coupling, etc., at each BPM.
- Segment-by-segment: Another Python script tasked with computing the local optics deviations of the observables provided by GetLLM, as described in Sec. 1.7.
- Segment-by-segment match: The automatic matching routine implemented in Python. Takes the local deviations computed by Segment-by-segment and computes an effective model of the segments as described in Sec. 2.1.
- correct.py: Performs the global corrections described in Sec. 1.6.1.

Together with many other smaller routines, these programs import turn-by-turn data acquired in the machine and produce optics functions and its corresponding corrections. Figure 4.1 shows a diagram of the data flow across these tools.

These tools are usually not run manually in the console, but instead a Java [86] Graphical User Interface (GUI) is used to handle the different inputs and outputs of the Python programs. This GUI is used in the CERN Control Center (CCC) to perform on-line analysis of the machine optics and allows plotting of the outputs of the different programs of Beta-Beat.src. Once the optics

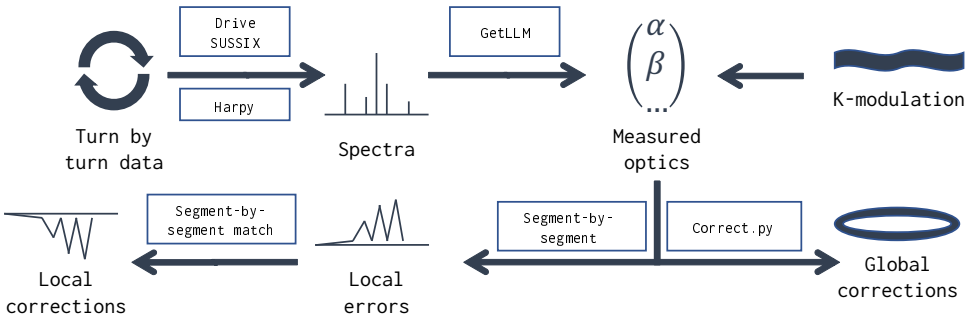

Figure 4.1: Diagram of the Beta-Beat.src analysis tools.

analysis is done and the corrections have been computed, the GUI can upload corrected settings to the machine directly.

During the studies presented here, I leaded a thorough process of refactoring of these tools. The data reading, cleaning and harmonic analysis scripts which were spread between Java and Python, have become a single Python module "hole in one" which eases and speeds up the analysis until this point. To achieve this, the BPM turn-by-turn data, in Self Describing Data Set (SDDS) [87] format, have to be loaded directly in Python. These files are provided by the LHC control system and consist of a plain text header that describes the structure of the data and a binary blob containing the data itself. The loading of these SDDS files was performed in Java directly, which then transformed the files into plain text format as input of Drive. With the development of Harpy, this transformation was no longer necessary and I developed a SDDS loader in Python. This allows for the turn-by-turn data to be passed directly from the loader to Harpy, making the analysis faster and easier to maintain.

GetLLM, the Python tool used to obtain the optics functions from the harmonic analysis of the turn-by-turn data, requires a model of the machine to compute the optics. These models contain the design optics of the machine at each interesting point (typically BPMs) and are calculated using MAD-X. The input files required to compute the models define the accelerator layout and the magnets strengths and therefore are updated frequently. The process of configuring and running these input files was done in the Java GUI. The addition of new models to the GUI was very cumbersome and led to significant errors and delays when human mistakes where made during these model changes. Therefore, we redeveloped this model creation system in Python using an inheritance model. This system allows to make the minimum possible changes needed to add in each new model, inheriting general properties of the accelerator. The "accelerator classes" developed to achieve this, have become the input of most of the analysis scripts, making them able to run on any accelerator (not only different LHC runs) by just implementing this class which contains very basic, usually constant, information about the accelerator.

Another important development we introduced during these studies is the use of the Pandas [88] library. This library is becoming the standard in data analysis in Python and makes the manipulation of data organised in tables (dataframes) much easier. The input and output of most of the programs of the Beta-Beat.src repository follow the output file format of MAD-X, the Table File System (TFS) files [89]. A shortened example of a Twiss table provided by MAD-X is as follows:

```
@ DATE              %08s "08/03/18"
```

```
@ TIME             %08s "14.36.25"
* NAME                          S              BETX              ALFX
$ %s                          %le               %le               %le
 "BPMYB.5L2.B1"            28.288        148.0431582       1.991695361
 "BPMYB.4L2.B1"            48.858        80.30065845        1.30157152
 "BPMWI.4L2.B1"            73.3255       82.88352533      -0.4945766312
 "BPMSX.4L2.B1"           123.4825       170.2734272       -1.247750499
 "BPMS.2L2.B1"             161.394       63.60892316       -1.309565306
 "BPMSW.1L2.B1"            171.328       56.92591778        2.164793505
```

This format fits almost perfectly the data structure provided by the Pandas dataframes. A TFS file reader was therefore developed to load these files into Pandas. This has allowed a reduction of many hundreds of lines on the Beta-Beat.src tools, as column-wise or row-wise operations, many statistical functions and plotting functionalities are provided out of the box and do not have to be programmed manually.

To ensure that the results of the analysis were unchanged during these modifications, we put in place an automatic regression testing routine. On every upload to the repository, this routine copies a specific version of the software which is known to work. Both versions of the software are put through a battery of tests which compares automatically the results of both versions. If any change is identified, the user is notified. This kind of tests are of great importance when making code improvements that are not intended to change the results (refactoring) as the developer is ensured that the code will be tested automatically in case any errors are made. This system detected several bugs introduced involuntarily by different developers during the length of these studies.

In the next sections, two projects we developed during the frame of these studies are introduced.

4.1 The automatic local matching GUI

A GUI has been developed to ease the use of the automatic matching tool described in Sec. 2.1. This GUI is written in Python which allows a direct communication with the rest of the OMC analysis tools which are also mainly programmed in Python. This is among the first Python GUIs used in the CCC at the time of its development. Nowadays, there is a significant effort to make Python usage at the control centre to be at least on par with Java.

This tool has to take as input in a typical correction of the LHC local optics of each of the main IRs: the phase deviations at each BPM for the two planes and the two beams and the measurement of the β^* (typically from K-modulation) in said IR also for both planes and both beams. All of this has to be computed twice if back-propagation is used. This variety of measurement data is hard to handle and to evaluate manually and the Segment-by-segment matching GUI aids visually to try and test during these analyses. Figure 4.2 shows a screenshot of the main view of the GUI. The GUI allows to add an arbitrary number of "matchers" to the analysis, which establish a set of constraints and variables. All matcher constraints are evaluated simultaneously. The available matcher types are:

- Phase: matches the local phase deviations of the segment measured at every BPM inside said segment using as variables all quadrupolar knobs found in the segment.

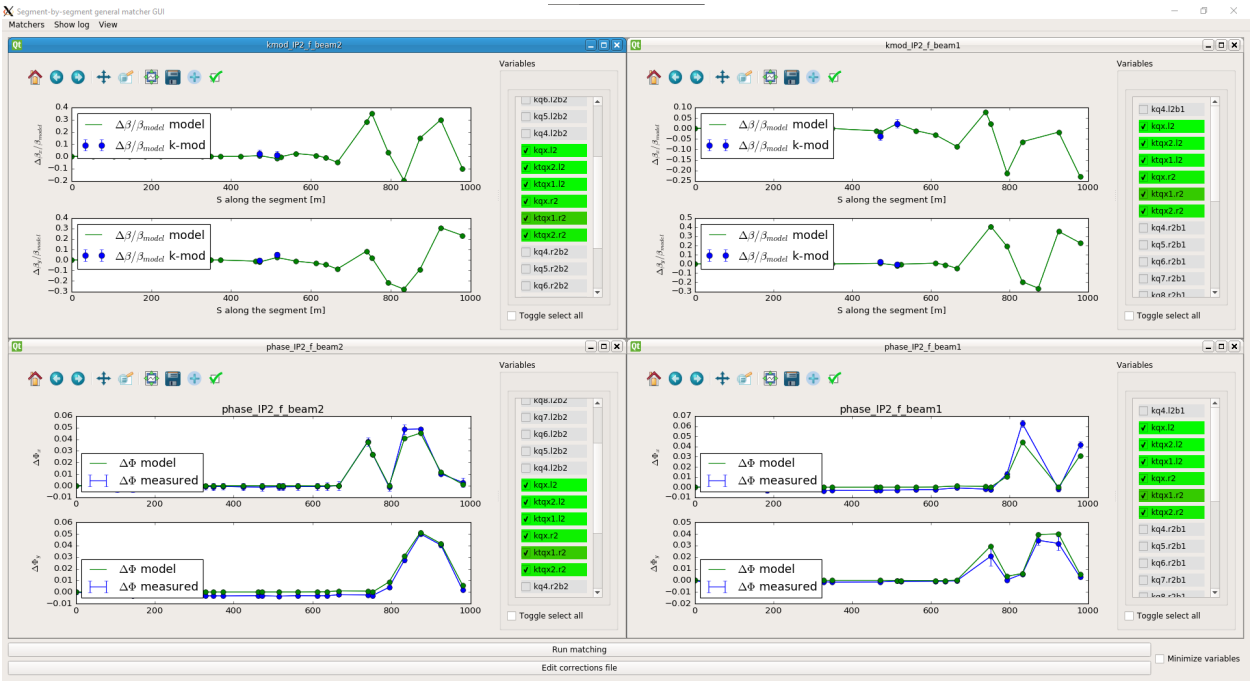

Figure 4.2: Screenshot of the Segment-by-segment matching GUI.

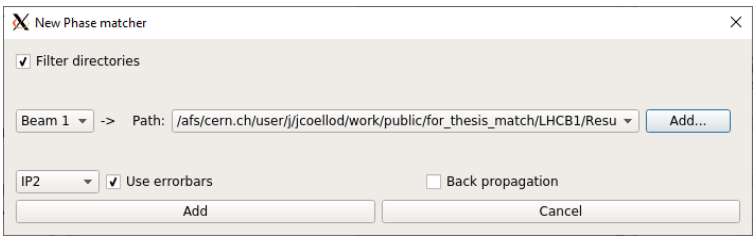

Figure 4.3: Screenshot of the matcher configuration screen of the Segment-by-segment matching GUI.

- β from amplitude: matches the β-beating w.r.t. the local model of the segment on the BPMs where there is calibration data available. It uses as variables all the quadrupolar knobs in the segment.
- β from K-modulation: same as β from amplitude but using the β-beating at the BPMs closest to the IP measured by K-modulation.
- Coupling: matches the real and imaginary parts of the f_{1001} resonance driving term at every BPM in the segment using all skew quadrupoles available in the segment, typically the two inner triplet skew quadrupole correctors.

All of these matchers can be configured to either take into account the errorbars of the measurements or not. If they are taken into account, a weight of $1/\sigma$ will be set to every BPM. The matchers can also be configured to do the backwards propagation described in Sec. 1.7. Figure 4.3 shows the configuration window for one of these matchers.

Once all the necessary matchers have been added, the GUI displays the measurements of the corresponding deviations in several plots. A checkbox for every available variable will be shown so the user can activate and deactivate them easily. Once the MAD-X matching routine is done, the GUI colours the variables checkboxes according to how strong the computed trims are. These

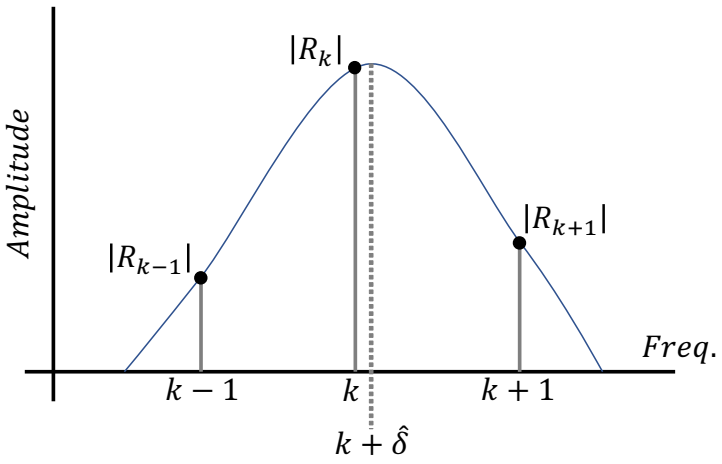

Figure 4.4: Diagram showing the position of the largest DFT coefficients and the actual peak of the DTFT.

found trims are then available in a text file to be put into the machine.

4.2 Harpy: turn-by-turn harmonic analysis in Python.

As it was mentioned in Sec. 1.6.1 the turn-by-turn data spectra is obtained using a specialised harmonic analysis tool. This tool has historically been SUSSIX, developed in 1998 to be used initially at the SPS and the LEP. This tool implements in FORTRAN a version of the Laskar algorithm. The Laskar algorithm target is to reconstruct the largest frequencies contained in a signal following an iterative method: The largest coefficient of the Discrete Fourier Transform (DFT) of the signal is taken. As the input signal has a finite number of samples, the DFT is a sampled grid over the continuous Discrete-Time Fourier Transform (DTFT) of the signal. The peak value of the DTFT contains the most precise location of the main frequency of the signal and it is located between the peak of the DFT and its two closest neighbours. SUSSIX uses the Newton method to find the frequency, ν, with largest amplitude. Amplitude and phase of the peak of the DTFT are computed at this frequency and stored in a complex variable $\hat{R}$. From this coefficient and frequency ν a pure signal $x(t)$ is constructed as:

$$x(t) = \hat{R}e^{2\pi i\nu t} \ . \tag{4.1}$$

This pure signal is then subtracted from the original to obtain a new signal. This new signal is taken as the new input of the Laskar method. This process iterates until all the main frequencies and coefficients of the signal are found. This set of coefficients and frequencies is used to reconstruct the linear and non-linear optics of accelerators.

The development of SUSSIX programmed in FORTRAN, was basically halted due to the program complexity, as any new features costed great effort. A new analysis tool, Harpy, has been developed to overcome the development complications of SUSSIX. This tool implements the Laskar method in Python [85] instead.

Python programs tend to run significantly slower than lower level languages like C++ or FORTRAN. However, Harpy manages to achieve processing times equal or even faster than SUSSIX by implementing the search of the peak of the DTFT using an interpolation function [90] which

gives the position ($\hat{\delta}$) w.r.t. the frequency of the largest DFT peak where the frequency peak of the DTFT is situated (Fig. 4.4):

$$\hat{\delta} = \frac{\tan(\pi/N)}{\pi/N} \operatorname{Real}\left(\frac{R_{k-1} - R_{k+1}}{2R_k - R_{k-1} - R_{k+1}}\right), \tag{4.2}$$

where R_k is the coefficient of the DFT with maximum amplitude, $R_{k\pm1}$ are the coefficients contiguous to the largest one and N is the number of samples.

The implementation of the Laskar method in this new harmonic analysis tool, takes few more than 15 lines of code in Python. The core function of the tool in Python (with Numpy [91]) is presented here:

```
def laskar_method(samples, num_harmonics):
    n = len(samples)
    coefficients, frequencies = [], []
    for i in range(num_harmonics):
        # Compute this harmonic frequency and coefficient:
        dft_data = np.fft.fft(samples)
        # Call the Jacobsen interpolation function:
        frequency = jacobsen(dft_data, (0, len(dft_data)))
        # Compute the Fourier coefficient at that frequency
        # (in a separate function):
        coefficient = _compute_coef(samples, frequency * n) / n

        # Store frequency and amplitude:
        coefficients.append(coefficient)
        frequencies.append(frequency)

        # Subtract the found pure tune from the signal:
        new_signal = \
            coefficient * np.exp(PI2I * frequency * np.arange(n))
        samples = samples - new_signal

    coefficients, frequencies = zip(*sorted(
        zip(coefficients, frequencies),
        key=lambda t: np.abs(t[0]),
        reverse=True,
    ))
    return frequencies, coefficients
```

This simplicity makes the harmonic analysis much easier to understand and eases the development of new features. The development of this new tool allowed a deeper general understanding of the harmonic analysis tools which has already triggered new studies like those in Ref. [24].

4.3 Summary

To perform the studies presented in this thesis, that relied on many Monte-Carlo simulations (Sections 2.2, 2.3, 2.4.1) and large statistical analysis, usable and reliable software tools are of critical importance.

During these studies there has been a significant effort on improving the tools used to measure and correct the optics of accelerators. Many of the parts of the analysis that were done directly in the operational Java tools have been moved to the Python side. This has allowed a much more flexible interaction between the different pieces of this collection of tools, making the analysis of the data also easier for the rest of the users, as the amount of users of Python in the community greatly exceeds the users of other languages.

At the end of the studies presented in this memory, the full set of computations from turn-by-turn data to local and global corrections can be performed exclusively in Python. The control system of the LHC, the LHC Software Architecture (LSA), can only be accessed, at the time of writing the present thesis, through a Java interface. Therefore, the direct communication with the machine in Python is not yet possible and thus we still rely on Java GUIs to acquire turn-by-turn data and perform K-modulations. In the future this could be solved by using bridge libraries like JPype [92].

A new Python GUI, among the first to be used in the CCC, has been developed. This GUI allows for online automatic calculation of local corrections in the LHC. The tool shows the results of the automatic local matching, allowing the users to quickly and easily add and remove constraints and variables. This tool has been used operationally many times during the Run 2 of the LHC.

A variant of the Laskar method has been also implemented in Python. This has allowed to start abandoning the old FORTRAN program that served the same purpose and start using a new tool that can be developed with the available human expertise, unlocking the development of this part of the analysis. This new implementation also achieves a similar or better performance than the old one, thanks to the use of a fast interpolation method.

Finally, I would like to highlight the importance of software quality in Physics. This is often neglected in the field as the analysis tools are developed with the single purpose of achieving a very specific task as fast as possible, ending up in many occasions with a disjoint set of programs. If no effort is put into the quality of these programs, future users typically see them as black boxes which very heavily hinders their development.

The availability of simple and reliable tools not only makes the analysis simpler, but also motivates new developments. Specifically, the progress presented in this chapter triggered many later improvements, some of which were motivated just by refactoring and rewriting of previous codes that were too hard to understand and which developers were unwilling to change.

Chapter 5

Summary of main results and Outlook

The studies presented in this thesis had a strong impact on the design of the future HL-LHC and will define its commissioning strategy. An automatic local optics matching routine has been developed, capable of computing automatically optics corrections for strong localised sources of errors thus replacing manual optics matching. When correcting the local optics of LHC interaction regions, the routine is capable of using for both beams and both planes the measured phase deviations and the β^* from K-modulation. This tool can also be used to correct the localised sources of betatron coupling produced in the interaction regions, taking into account the real and imaginary parts of the f_{1001} resonance driving term.

The automatic matching routine has been used to perform Monte-Carlo simulations of the HL-LHC expected field error in the new triplet quadrupoles, demonstrating how the algorithm is able to correct the β^* down to the K-modulation uncertainty level. These studies show that in achieving the project performance of HL-LHC and avoiding intolerable luminosity imbalances between ATLAS and CMS, the limiting factor (from the beam optics point of view) is the precision of the measurement of the β^*.

In the thesis the potential of K-modulation, the currently used technique to measure β^*, has been explored. K-modulation has shown erratic results during Run 2 of the LHC, and it is not expected to reach the required precision in HL-LHC in its current form. Some improvements made to approach the required precision level have been explored, mainly with the redesign of the HL-LHC triplet powering circuit, allowing for better compensation of the tune noise, adding a new trim in the first half of Q1 which improves the precision of K-modulation a factor 2, and removing the superfluous trim in one of the halves of Q2 which will help save resources in the construction of HL-LHC. The possibility of using the tune feedback system to compensate the tune changes during the modulations allowing for larger modulation amplitudes also has been explored. It has been demonstrated experimentally that the tune feedback system is not yet ready for this, presenting technical issues that make this approach unfeasible. With all this, K-modulation is still factor 2 away from the precision necessary to keep the luminosity imbalance between ATLAS and CMS below 5%.

Monte-Carlo simulations of the betatron coupling produced by the HL-LHC quadrupole tilts and its corrections using the skew quadrupoles in the interaction regions have also been performed. This allowed to prove that, as far as the average tilt of the triplet is within $\pm$1mrad, there is a large strength margin in this correctors and therefore their strength can be reduced by a factor of 2, while still keeping a factor 2 margin in strength in case one of the skew quadrupoles breaks.

As an alternative to K-modulation, two new complementary techniques have been theoretically and experimentally explored.

The first of them consists in using the phase-advance across the IP to compute the β-function at the beam waist. However, it has also been demonstrated that this technique is blind to the position of the beam waist. It has been shown that the normal BPM electronics are not precise enough in the measurement of the phase-advance to be a feasible alternative to K-modulation. However, the BPMs closest to the IPs are equipped with the DOROS electronics, which has been experimentally proved to provide a measurement of the phase-advance across the IP a factor 3 better in the LHC. The measurement of the DOROS system has been theoretically extrapolated to squeezed HL-LHC optics configurations and still provide a measurement of the β-function at the beam waist accurate enough to control the luminosity imbalance to the required levels.

The idea of the second explored technique is to measure the position of the beam waist with luminosity scans using beam waist shifts. The theoretical framework of the behaviour of the luminosity under changing beam waist has been developed, showing how this technique can be used to measure the position of the beam waist but that it is blind to the value of the β-function at the waist itself. This technique has been experimentally used in the LHC to measure the beam waist, the first use of this type of scans in a machine with safety concerns. After an extensive data processing, documented in the thesis, the luminosity scans provided a more precise measurement of the waist position than the latest results of K-modulation for the same optics configuration. This conclusion is based in one single luminosity scan per beam and therefore this experiment must be repeated in the future to gain statistics.

These two techniques together provide a full alternative to K-modulation, but will require modifications in the LHC commissioning flow, as the luminosity scans can only be performed with intense enough beams to precisely measure the luminosity and therefore the machine should be safe to operate with such beams before these measurements are performed.

An exceptionally high β-beating in one of the LHC arcs, that seemed uncorrectable using the traditional optics correction techniques, was observed during a machine development test in the LHC with flat optics using the ATS optics scheme. In this thesis it has been proven that the source of this high β-beating is a localised error in the arc, enhanced by the large β-function in the arcs produced by the ATS optics scheme. This new type of error could not be corrected with quadrupole magnets because of the lack of individually powered correctors in the region. As an alternative, a knob was designed, which produces an orbit bump across the arc sextupoles and therefore produces a quadrupolar effect via feed-down. The knob has been experimentally tested with success in the LHC. In the HL-LHC the ATS optics scheme is going to be used in an even more pushed configuration and therefore it is likely that this new type of corrections are going to be necessary.

The new HL-LHC triplet is going to use the Nb_3Sn superconductor technology allowing for an increase of the magnetic field strength of about 50%. Measurements of the magnetic field in prototypes of the new quadruples have shown that these new technology is susceptible to flux-jumps, which can cause sudden changes of the magnet current and therefore on the field seen by the beam. In this thesis a statistical analysis of these measurements has been performed and

concrete values of the magnitude and length of these events have been obtained. Both the effect of the flux jump in the current itself and the reaction of the current regulation loop have been studied, concluding that the effect of the flux jump in the current dominates. Results of the theoretical analysis of the effect of this change of current on the beam emittance, orbit and tune are presented. Assuming always conservative error bars in the measurements of the flux jumps in the prototypes, it has been found that the emittance would only grow about 0.1‰ in the typical ramp of the HL-LHC. The effects on the orbit and noise have also been found to be negligible.

For the FCC-hh though, as all the dipoles are projected to use the Nb_3Sn technology, flux jumps can cause about a 70% increase of emittance during the typical energy ramp. Therefore, flux jumps have been proven not to be a concern in current or near future colliders, but can become a serious problem in future accelerators when the Nb_3Sn technology is more widely used.

In order to meet the necessity to perform the large volume of simulations of the thesis studies many of the software tools used by the Optics Measurements and Corrections team of the LHC have been intensively refactored and many improvements and new features have been added. The use of the Pandas library has been introduced to the team, reducing the length and complexity of many of the programs. An automatic regression testing system has also been developed, which has prevented the introduction of many errors during Run 2.

The full analysis of the turn-by-turn data to obtain a measurement of the optics, that used to be spread among Java, FORTRAN/C++ and Python, can now be fully performed in Python, allowing faster analysis and more automatic analysis. This includes the generation of models of different machines from Python, using a generic class structure that makes porting the tools to other LHC runs or even other accelerators significantly easier.

A new GUI written in Python has been developed to ease the use of the automatic matching routine. This GUI is among the first Python GUIs to be used operationally in the CERN Control Centre. It allows to rapidly produce and test different local corrections and has been extensively used during LHC Run 2.

A new implementation of the Laskar method written in Python, Harpy, has been developed. This new implementation is significantly simpler than the old FORTRAN/C++ program, which has opened the door to later studies that improve the harmonic analysis performance and accuracy. It can achieve a performance similar or better to the old FORTRAN program by using fast interpolation methods.

5.1 Closing remarks and future work

The results presented in this thesis address the challenges that have risen over time in order to control the beam optics and emittance in the LHC and those expected in the HL–LHC as the β^* are pushed to lower values. As it has been shown, the control of these parameters is critical to guarantee the safety and performance of the particle accelerator. Future colliders are expected to push the β^* even lower and therefore the results presented here will be of increasing importance over time.

The new techniques, β_w from phase-advance across the IP and luminosity scans, are the only available complement to K-modulation, which has been shown here to not be accurate enough to

ensure future colliders performance. Also, the orbit bumps in sextupoles are the only feasible way of correcting arc local errors. Therefore it is of critical importance that these methods are further explored in future studies and that they are streamlined to make them leap from experimental techniques to fully operational tools, integrated with the automatic local optics correction tool also described here.

The effects of the flux jumps presented in this thesis are the result of the first measurements of this effect on prototypes of LHC magnets using the Nb_3Sn technology, but the theoretical framework has been provided to extrapolate these results to measurements on the final production magnets. Therefore, this investigation must be updated in the future when more flux jump data is available.

The software developments shown here have also kick-started the effort to improve the quality of the tools used to perform optics measurements and corrections and have triggered new studies. This effort still continues and will prevent future errors in such important analyses for the performance of accelerators.

In summary, this thesis sets the path for local optics control in current and future particle colliders, demonstrating the challenges and providing solutions in this area and sets the theoretical framework and first results on the effects of flux jumps, while demonstrating the importance of software quality in this branch of science.

Abbreviations

AC-dipole	Alternating Current Dipole.
ALICE	A Large Ion Collider Experiment.
APC	Artificial Pinning Centers.
ATLAS	A Toroidal LHC ApparatuS.
ATS	Achromatic Telescopic Squeeze.
BPM	Beam Position Monitor.
CCC	CERN Control Center.
CERN	European Organization for Nuclear Research.
CMS	Compact Muon Solenoid.
DFT	Discrete Fourier Transform.
DOROS	Diode ORbit and OScillation.
DTFT	Discrete-Time Fourier Transform.
FCC	Future Circular Collider.
GUI	Graphical User Interface.
HL-LHC	High Luminosity LHC.
IP	Interaction Point.
IR	Interaction Region.
LEP	Large Electron–Positron.
LHC	Large Hadron Collider.
LHCb	Large Hadron Collider beauty.
LSA	LHC Software Architecture.
MD	Machine Development.
OMC	Optics Measurements and Corrections.
RDT	Resonance Driving Term.

SDDS	Self Describing Data Set.
SPS	Super Proton Synchrotron.
SVD	Singular Value Decomposition.
TCPs	Primary Collimators.
TFS	Table File System.

Bibliography

[1] J. D. Cockcroft and E. T. S. Walton, *Disintegration of lithium by swift protons*, Nature **129** (1932), pp. 649–649. url: https://doi.org/10.1038/129649a0, doi:10.1038/129649a0.

[2] J. Coello de Portugal, R. Tomás, and M. Hofer, *New local optics measurements and correction techniques for the lhc and its luminosity upgrade*, Phys. Rev. Accel. Beams **23** (2020), p. 041001. url: https://link.aps.org/doi/10.1103/PhysRevAccelBeams.23.041001, doi:10.1103/PhysRevAccelBeams.23.041001.

[3] J. Coello de Portugal, R. Tomás, L. Fiscarelli, D. Gamba, and M. Martino, *Impact of flux jumps in future colliders*, Phys. Rev. Accel. Beams **23** (2020), p. 011001. url: https://link.aps.org/doi/10.1103/PhysRevAccelBeams.23.011001, doi:10.1103/PhysRevAccelBeams.23.011001.

[4] M. G. Minty and F. Zimmermann, *Measurement and Control of Charged Particle Beams*, Springer-Verlag Berlin Heidelberg, 1 ed., 2003.

[5] E. J. N. Wilson, *An introduction to particle accelerators*, Oxford Univ. Press, Oxford, 2001. url: http://cds.cern.ch/record/513326, doi:10.1093/acprof:oso/9780198508298.001.0001.

[6] S. Y. Lee, *Accelerator physics; 3rd ed.*, World Scientific, Singapore, 2012. url: https://cds.cern.ch/record/1425444.

[7] P. Bryant, *Beam Transfer Lines*, in CAS - CERN Accelerator School : 5th General Accelerator Physics Course, vol. 1, Jyväskylä, Finland, Sep 1992, CERN, CERN, pp. 239–258. url: https://cds.cern.ch/record/235242, doi:10.5170/CERN-1994-001.

[8] R. Tomás, *Adiabaticity of the ramping process of an ac dipole*, Phys. Rev. ST Accel. Beams **8** (2005), p. 024401. url: https://link.aps.org/doi/10.1103/PhysRevSTAB.8.024401, doi:10.1103/PhysRevSTAB.8.024401.

[9] J. Buon, *Beam phase space and emittance; rev. version* (1992), p. 27 p. url: https://cds.cern.ch/record/242313, doi:10.5170/CERN-1994-001.89.

[10] W. Herr and B. Muratori, *Concept of luminosity* (2006). url: https://cds.cern.ch/record/941318.

[11] G. Robert-Démolaize, *Design and Performance Optimization of the LHC Collimation System*, PhD thesis, 2006. Presented on 20 Nov 2006. url: http://cds.cern.ch/record/1004869.

[12] P. J. Bryant, *A simple theory for weak betatron coupling* (1994). url: https://cds.cern.ch/record/261066, doi:10.5170/CERN-1989-005.50.

[13] A. Verdier, *Chromaticity (particle accelerators)* (1995). url: https://cds.cern.ch/record/302491, doi:10.5170/CERN-1995-006.77.

[14] *The ATLAS Experiment at the CERN Large Hadron Collider*, JINST **3** (2008), p. S08003. 437 p. Also published by CERN Geneva in 2010. url: http://cds.cern.ch/record/1129811.

[15] *The CMS experiment at the CERN LHC. The Compact Muon Solenoid experiment*, JINST **3** (2008), p. S08004. 361 p. Also published by CERN Geneva in 2010. url: http://cds.cern.ch/record/1129810.

[16] *The ALICE experiment at the CERN LHC. A Large Ion Collider Experiment*, JINST **3** (2008), p. S08002. 259 p. Also published by CERN Geneva in 2010. url: https://cds.cern.ch/record/1129812.

[17] *The LHCb Detector at the LHC*, JINST **3** (2008), p. S08005. Also published by CERN Geneva in 2010. url: https://cds.cern.ch/record/1129809, doi:10.1088/1748-0221/3/08/S08005.

[18] O. Brüning and L. Rossi, *The High Luminosity Large Hadron Collider*, World Scientific, 2015. url: https://www.worldscientific.com/doi/abs/10.1142/9581, doi:10.1142/9581.

[19] H. Damerau, A. Funken, R. Garoby, S. Gilardoni, B. Goddard, K. Hanke, A. Lombardi, D. Manglunki, M. Meddahi, B. Mikulec, G. Rumolo, E. Shaposhnikova, M. Vretenar, and J. Coupard, *LHC Injectors Upgrade, Technical Design Report, Vol. I: Protons*, Tech. Rep. CERN-ACC-2014-0337, Dec 2014. url: https://cds.cern.ch/record/1976692.

[20] S. Fartoukh, *Achromatic telescopic squeezing scheme and application to the lhc and its luminosity upgrade*, Phys. Rev. ST Accel. Beams **16** (2013), p. 111002. url: https://link.aps.org/doi/10.1103/PhysRevSTAB.16.111002, doi:10.1103/PhysRevSTAB.16.111002.

[21] S. Fartoukh, M. Albert, Y. Le Borgne, C. Bracco, R. Bruce, F. S. Carlier, J. M. Coello De Portugal Martinez Vazquez, A. Garcia-Tabares Valdivieso, K. Fuchsberger, R. Giachino, E. H. Maclean, L. Malina, A. Mereghetti, D. Mirarchi, D. Nisbet, L. Normann, G. Papotti, T. H. B. Persson, M. Pojer, L. Ponce, S. Redaelli, B. M. Salvachua Ferrando, P. K. Skowronski, M. Solfaroli Camillocci, R. Suykerbuyk, R. Tomás Garcia, D. Valuch, A. Wegscheider, and J. Wenninger, *ATS MD's in 2016* (2016). url: http://cds.cern.ch/record/2242513.

[22] M. Benedikt, M. Capeans Garrido, F. Cerutti, B. Goddard, J. Gutleber, J. M. Jimenez, M. Mangano, V. Mertens, J. A. Osborne, T. Otto, J. Poole, W. Riegler, D. Schulte, L. J. Tavian, D. Tommasini, and F. Zimmermann, *Future Circular Collider*, Tech. Rep. CERN-ACC-2018-0058, CERN, Geneva, Dec 2018. Submitted for publication to Eur. Phys. J. ST. url: https://cds.cern.ch/record/2651300.

[23] R. Bartolini and F. Schmidt, *A Computer Code for Frequency Analysis of Non-Linear Betatron Motion*, Tech. Rep. SL-Note-98-017-AP, CERN, Geneva, Feb 1998. url: https://cds.cern.ch/record/702438.

[24] L. Malina, J. Coello de Portugal, J. Dilly, P. Skowronski, and R. Tomás, *Optics Measurements in Storage Rings: Simultaneous 3-Dimensional Beam Excitation and Novel Harmonic Analysis*,

Proc. 7th Int. Beam Instrumentation Conf. (IBIC'18) (2018), pp. 177–181. url: doi:10.18429/JACoW-IBIC2018-TUOB02.

[25] A. Garcia-Tabares Valdivieso, *Optics-measurement-based Beam Position Monitor Calibration.. Calibración de monitores de posición del haz basado en medidas ópticas.*, PhD thesis, Sep 2019. Presented 08 Nov 2019. url: https://cds.cern.ch/record/2701414.

[26] A. G.-T. Valdivieso and R. Tomás, *Optics-measurement-based beam position monitor calibrations in the lhc insertion regions*, Phys. Rev. Accel. Beams **23** (2020), p. 042801. url: https://link.aps.org/doi/10.1103/PhysRevAccelBeams.23.042801, doi:10.1103/PhysRevAccelBeams.23.042801.

[27] A. S. Langner, *A Novel Method and Error Analysis for Beam Optics Measurements and Corrections at the Large Hadron Collider*, PhD thesis, Feb 2017. Presented 2017. url: http://cds.cern.ch/record/2265177.

[28] R. Miyamoto, S. E. Kopp, A. Jansson, and M. J. Syphers, *Parametrization of the driven betatron oscillation*, Phys. Rev. ST Accel. Beams **11** (2008), p. 084002. url: https://link.aps.org/doi/10.1103/PhysRevSTAB.11.084002, doi:10.1103/PhysRevSTAB.11.084002.

[29] A. Langner, G. Benedetti, M. Carlà, U. Iriso, Z. Martí, J. C. de Portugal, and R. Tomás, *Utilizing the n beam position monitor method for turn-by-turn optics measurements*, Phys. Rev. Accel. Beams **19** (2016), p. 092803. url: https://link.aps.org/doi/10.1103/PhysRevAccelBeams.19.092803, doi:10.1103/PhysRevAccelBeams.19.092803.

[30] A. Wegscheider, A. Langner, R. Tomás, and A. Franchi, *Analytical n beam position monitor method*, Phys. Rev. Accel. Beams **20** (2017), p. 111002. url: https://link.aps.org/doi/10.1103/PhysRevAccelBeams.20.111002, doi:10.1103/PhysRevAccelBeams.20.111002.

[31] M. Aiba, S. Fartoukh, A. Franchi, M. Giovannozzi, V. Kain, M. Lamont, R. Tomás, G. Vanbavinckhove, J. Wenninger, F. Zimmermann, R. Calaga, and A. Morita, *First β-beating measurement and optics analysis for the cern large hadron collider*, Phys. Rev. ST Accel. Beams **12** (2009), p. 081002. url: https://link.aps.org/doi/10.1103/PhysRevSTAB.12.081002, doi:10.1103/PhysRevSTAB.12.081002.

[32] E. Fol, J. Coello de Portugal, and R. Tomás, *Unsupervised machine learning for detection of faulty beam position monitors*, Melbourne, Australia, May 2019, p. 2668–2671.

[33] E. Fol, J. Coello de Portugal, and R. Tomás, *Isolation forest algorithm for faulty beam position monitors detection*, to be published .

[34] H. Grote and F. Schmidt, *MAD-X: An Upgrade from MAD8* (2003), p. 4 p. url: https://cds.cern.ch/record/618496.

[35] R. Bartolini and F. Schmidt, *Normal form via tracking or beam data*, Part. Accel. **59** (1997), pp. 93–106. 10 p. url: https://cds.cern.ch/record/333077.

[36] R. Tomasi, *Direct Measurement of Resonance Driving Terms in the Super Proton Synchrotron (SPS) of CERN using Beam Position Monitors*, Uni. of Valencia (2003). url: https://cds.cern.ch/record/615164.

[37] T. Persson and R. Tomás, *Improved control of the betatron coupling in the large hadron collider*, Phys. Rev. ST Accel. Beams **17** (2014), p. 051004. url: https://link.aps.org/doi/10.1103/PhysRevSTAB.17.051004, doi:10.1103/PhysRevSTAB.17.051004.

[38] T. Persson, F. Carlier, J. Coello de Portugal, A. Garcia-Tabares Valdivieso, A. Langner, E. H. Maclean, L. Malina, P. Skowronski, B. Salvant, R. Tomás, and A. C. G. Bonilla, *Lhc optics commissioning: A journey towards 1% optics control*, Phys. Rev. Accel. Beams **20** (2017), p. 061002. url: https://link.aps.org/doi/10.1103/PhysRevAccelBeams.20.061002, doi:10.1103/PhysRevAccelBeams.20.061002.

[39] R. Tomás, O. Brüning, M. Giovannozzi, P. Hagen, M. Lamont, F. Schmidt, G. Vanbavinckhove, M. Aiba, R. Calaga, and R. Miyamoto, *Cern large hadron collider optics model, measurements, and corrections*, Phys. Rev. ST Accel. Beams **13** (2010), p. 121004. url: https://link.aps.org/doi/10.1103/PhysRevSTAB.13.121004, doi:10.1103/PhysRevSTAB.13.121004.

[40] A. Langner, J. Coello de Portugal, P. K. Skowronski, and R. Tomás, *Developments of the Segment-by-Segment Technique for Optics Corrections in the LHC*, Proc. 6th Int. Particle Accelerator Conf. (IPAC'15) (2015), pp. 419–422. url: doi:10.18429/JACoW-IPAC2015-MOPJE054.

[41] R. Tomás Garcia, M. Aiba, C. Alabau, O. Brüning, R. Calaga, M. Giovannozzi, V. Kain, P. Hagen, M. Lamont, R. Miyamoto, F. Schmidt, M. Strzelczyk, and G. Vanbavinckhove, *The LHC optics in practice* (2010). url: https://cds.cern.ch/record/1359183, doi:oai:cds.cern.ch:1359183.

[42] R. Tomás, T. Bach, R. Calaga, A. Langner, Y. I. Levinsen, E. H. Maclean, T. H. B. Persson, P. K. Skowronski, M. Strzelczyk, G. Vanbavinckhove, and R. Miyamoto, *Record low β beating in the lhc*, Phys. Rev. ST Accel. Beams **15** (2012), p. 091001. url: https://link.aps.org/doi/10.1103/PhysRevSTAB.15.091001, doi:10.1103/PhysRevSTAB.15.091001.

[43] F. Carlier and R. Tomás, *Accuracy and feasibility of the β^* measurement for LHC and High Luminosity LHC using k modulation*, Phys. Rev. Accel. Beams **20** (2017), p. 011005. doi:10.1103/PhysRevAccelBeams.20.011005.

[44] E. H. Maclean, R. Tomas Garcia, F. S. Carlier, J. M. Coello De Portugal, E. Fol, K. Fuchsberger, A. Garcia-Tabares Valdivieso, M. Giovannozzi, M. Hofer, L. Malina, T. H. B. Persson, P. K. Skowronski, M. Solfaroli Camillocci, and A. Wegscheider, *Detailed review of the LHC optics commissioning for the nonlinear era*, Tech. Rep. CERN-ACC-2019-0029, CERN, Geneva, Feb 2019. url: https://cds.cern.ch/record/2655741.

[45] F. S. Carlier, J. Coello De Portugal, S. Fartoukh, E. Fol, D. Gamba, A. Garcia-Tabares, M. Giovannozzi, M. Hofer, A. S. Langner, E. H. Maclean, L. Malina, L. E. Medina Medrano, T. H. B. Persson, P. K. Skowronski, R. Tomás Garcia, F. Van Der Veken, and A. Wegscheider, *Optics Measurements and Correction Challenges for the HL-LHC* (2017). url: https://cds.cern.ch/record/2290899.

[46] M. Hofer, R. Tomas, and F. Carlier, *K-modulation in future high energy colliders*, Proc. 10th Int. Particle Accelerator Conf. (IPAC'19) (2019), pp. 476–479.

[47] G. Apollinari, I. Bejar, O. Bruning, P. Fessia, M. Lamont, L. Rossi, and L. Tavian, eds., *High-Luminosity Large Hadron Collider (HL-LHC): Technical Design Report V. 0.1*, CERN Yellow Reports: Monographs, CERN, Geneva, 2017. url: http://cds.cern.ch/record/2284929.

[48] L. E. Medina Medrano, R. Tomas, G. Arduini, and M. Napsuciale Mendívil, *Assessment of the performance of High Luminosity LHC operational scenarios: integrated luminosity and effective pile-up density*, Canadian Journal of Physics (2018). url: https://doi.org/10.1139/cjp-2018-0291, doi:10.1139/cjp-2018-0291.

[49] J. M. Coello De Portugal, S. Fartoukh, E. Fol, A. Garcia-Tabares Valdivieso, E. H. Maclean, L. Malina, T. H. B. Persson, P. K. Skowronski, M. Solfaroli Camillocci, R. Tomas Garcia, and A. Wegscheider, *MD2148: Flat optics* (2018). url: https://cds.cern.ch/record/2632141.

[50] S. Fartoukh et al., *LHC Beam experiments with telescopic flat optics in 2018*, To be publised (2019).

[51] T. H. B. Persson et al., *Run 2 Optics and Corrections*, 9th LHC Operations Evian Workshop (2019).

[52] R. Calaga, R. Tomás, and A. Franchi, *Betatron coupling: Merging hamiltonian and matrix approaches*, Phys. Rev. ST Accel. Beams **8** (2005), p. 034001. url: https://link.aps.org/doi/10.1103/PhysRevSTAB.8.034001, doi:10.1103/PhysRevSTAB.8.034001.

[53] G. Ambrosio, *QXF Progress & Recent Results*. Presented in the 4th Joint HiLumi LHC-LARP Annual Meeting, Nov 2014. url: https://indico.cern.ch/event/326148/contributions/1711569/attachments/633148/871397/Ambrosio_QXF_Progress_RecentResults_v5b.pdf.

[54] H. M. Durand et al., *HL-LHC Alignment Requirements and Associated Solutions*, Proc. 8th Int. Particle Accelerator Conf. (IPAC'17) (2017), pp. 1893–1896. url: doi:10.18429/JACoW-IPAC2017-TUPIK085.

[55] A. Boccardi, A. Butterworth, E. Calvo Giraldo, R. Denz, M. Gasior, J. Gonzalez, S. Jackson, L. Jensen, O. Jones, Q. King, G. Kruk, M. Lamont, S. Page, R. Steinhagen, and J. Wenninger, *Commissioning and Initial Performance of the LHC Beam-Based Feedback Systems* (2010), p. 3 p. url: http://cds.cern.ch/record/1272167.

[56] J. Coello de Portugal, *Minimum trim requirements and advantages of the single-circuit configuration*, Presented at the HL-LHC Magnet Circuits Internal Review (2017). url: https://indico.cern.ch/event/611018/.

[57] M. Gasior, G. Baud, J. Olexa, and G. Valentino, *First Operational Experience with the LHC Diode ORbit and OScillation (DOROS) System* (2017), p. MOPG07. 4 p. url: https://cds.cern.ch/record/2313935.

[58] T. Persson, J. Coello de Portugal, A. Garcia-Tabares, M. Gasior, A. Langner, T. Lefevre, E. Maclean, L. Malina, J. Olexa, P. Skowronski, and R. Tomas, *Experience with DOROS BPMs for Coupling Measurement and Correction* (2016), p. MOPMR029. 3 p. url: http://cds.cern.ch/record/2207315.

[59] A. Morita, *Status of SuperKEKB phase-2 commissioning*, Proceedings, 39th International Conference on High Energy Physics (ICHEP2018): Seoul, Korea, July 4-11, 2018 (2019), p. 228. doi:10.22323/1.340.0228.

[60] A. Morita, *Status of SuperKEKB phase-2 commissioning*. Presented in the 39th International Conference on High Energy Physics (ICHEP2018), 2018. url: https://indico.cern.ch/event/686555/contributions/2962552/attachments/1681111/2700857/ichep2018_KEK_A.Morita.pdf.

[61] L. van Riesen-Haupt, J. M. Coello de Portugal, E. Fol, A. Seryi, and R. Tomás, *K-Modulation Developments via Simultaneous Beam Based Alignment in the LHC* (2017), p. TUPVA042. 4 p. url: https://cds.cern.ch/record/2289680.

[62] J. Coello De Portugal, E. Fol, L. Malina, and R. Tomas Garcia, *MD3287: Luminosity scans with waist shifts* (2020). url: https://cds.cern.ch/record/2733019.

[63] G. Avoni et al., *The new LUCID-2 detector for luminosity measurement and monitoring in ATLAS*, JINST **13** (2018), p. P07017. doi:10.1088/1748-0221/13/07/P07017.

[64] *Luminosity determination in pp collisions at* $\sqrt{s} = 13$ *TeV using the ATLAS detector at the LHC*, Tech. Rep. ATLAS-CONF-2019-021, CERN, Geneva, Jun 2019. url: http://cds.cern.ch/record/2677054.

[65] S. Fartoukh, R. Bruce, F. Carlier, J. C. De Portugal, A. Garcia-Tabares, E. Maclean, L. Malina, A. Mereghetti, D. Mirarchi, T. Persson, M. Pojer, L. Ponce, S. Redaelli, B. Salvachua, P. Skowronski, M. Solfaroli, R. Tomás, D. Valuch, A. Wegscheider, and J. Wenninger, *Experimental validation of the Achromatic Telescopic Squeezing (ATS) scheme at the LHC*, J. Phys. : Conf. Ser. **874** (2017), p. 012010. 7 p. url: https://cds.cern.ch/record/2275964.

[66] P. Ferracin, G. Ambrosio, M. Anerella, F. Borgnolutti, R. Bossert, D. Cheng, D. R. Dietderich, H. Felice, A. Ghosh, A. Godeke, S. Izquierdo Bermudez, P. Fessia, S. Krave, M. Juchno, J. C. Perez, L. Oberli, G. Sabbi, E. Todesco, and M. Yu, *Magnet Design of the 150 mm Aperture Low-β Quadrupoles for the High Luminosity LHC*, IEEE Transactions on Applied Superconductivity **24** (2014), pp. 1–6. doi:10.1109/TASC.2013.2284970.

[67] A. Godeke, D. Cheng, D. R. Dietderich, P. Ferracin, S. O. Prestemon, G. Sabbi, and R. M. Scanlan, *Limits of NbTi and* Nb_3Sn*, and Development of W&R Bi–2212 High Field Accelerator Magnets*, IEEE Transactions on Applied Superconductivity **17** (2007), pp. 1149–1152. doi:10.1109/TASC.2007.898447.

[68] W. Meissner and R. Ochsenfeld, *Ein neuer effekt bei eintritt der supraleitfähigkeit*, Naturwissenschaften **21** (1933), pp. 787–788. url: https://doi.org/10.1007/BF01504252, doi:10.1007/BF01504252.

[69] D. Boussard, W. Höfle, and T. P. R. Linnecar, *The LHC Transverse Damper (ADT) Performance Specification*, Tech. Rep. SL-Note-99-055-HRF, CERN, Geneva, Mar 2000. url: http://cds.cern.ch/record/702559.

[70] L. Fiscarelli, *Measurements and analysis of flux jumps*. Presented in the 144th HiLumi WP2 meeting, Mar 2019. url: https://indico.cern.ch/event/803396/.

[71] M. Martino, P. Arpaia, and S. Ierardi, *Impact of Flux Jumps on High-Precision Powering of Nb3Sn Superconducting Magnets*, Proc. 10th Int. Particle Accelerator Conf. (IPAC'19) (2019), pp. 1338–1340. url: doi:10.18429/JACoW-IPAC2019-TUPMP040.

[72] M. Martino, *Progress on: Impact of Flux Jumps of Nb3Sn Magnets on Power Converter Performance*. Presented in the 144th HiLumi WP2 meeting, Mar 2019. url: https://indico.cern.ch/event/803396/.

[73] E. Metral, S. Antipov, F. Antoniou, R. B. Appleby, G. Arduini, J. Barranco Garcia, P. Baudrenghien, N. Biancacci, C. Bracco, R. Bruce, X. Buffat, R. Calaga, L. R. Carver, E. Chapochnikova, M. P. Crouch, R. De Maria, S. Fartoukh, D. Gamba, M. Giovannozzi, P. Goncalves Jorge, W. Hofle, G. Iadarola, N. Karastathis, A. Lasheen, T. Mastoridis, L. E. Medina Medrano, A. Mereghetti, D. Mirarchi, B. Muratori, P. S. Papadopoulou, Y. Papaphilippou, D. Pellegrini, T. Pieloni, S. Redaelli, G. Rumolo, B. Salvant, M. Solfaroli Camillocci, C. Tambasco, R. Tomas Garcia, and D. Valuch, *Update of the HL-LHC operational scenarios for proton operation* (2018). url: https://cds.cern.ch/record/2301292.

[74] D. Gamba, G. Arduini, M. Cerqueira Bastos, J. M. Coello De Portugal Martinez Vazquez, R. De Maria, M. Giovannozzi, M. Martino, and R. Tomas Garcia, *Beam dynamics requirements for HL-LHC electrical circuits*, Tech. Rep. CERN-ACC-2017-0101, CERN, Geneva, Dec 2017. url: https://cds.cern.ch/record/2298764.

[75] X. Xingchen, X. Peng, M. Rochester, J. Sumption, and J. Lee, *Opportunities and Challenges with APC Nb3Sn*, presented at the 22nd joint Cryogenic Engineering Conference and International Cryogenic Materials Conference (CEC-ICMC 2019) (2019).

[76] X. Xu, M. D. Sumption, and X. Peng, *Internally oxidized nb3sn strands with fine grain size and high critical current density*, Advanced Materials **27** (2015), pp. 1346–1350. url: https://onlinelibrary.wiley.com/doi/abs/10.1002/adma.201404335, doi:10.1002/adma.201404335.

[77] R. Tomás et al., *Prospects for the lhc optics measurements and corrections at higher energy*, Proc. 5th Int. Particle Accelerator Conf. (IPAC'14) (2014), pp. 1046–1048. url: doi:10.18429/JACoW-IPAC2014-TUPRO018.

[78] J. Coello de Portugal, F. Carlier, A. Langner, T. Persson, P. K. Skowronski, and R. Tomás, *OMC Software Improvements in 2014*, Proc. 6th Int. Particle Accelerator Conf. (IPAC'15) (2015), pp. 426–429. url: doi:10.18429/JACoW-IPAC2015-MOPJE056.

[79] R. Tomas et al., *Lhc optics measurement and correction software progress and plans*, Proc. 10th Int. Particle Accelerator Conf. (IPAC'19) (2019), pp. 2773–2776.

[80] OMC Team, *OMC Beta-Beat.src*, GitHub . url: https://github.com/pylhc/Beta-Beat.src.git.

[81] R. Tomás García, *Direct Measurement of Resonance Driving Terms in the Super Proton Synchrotron (SPS) of CERN using Beam Position Monitors*, PhD thesis, 2003. Presented on 30 Mar 2003. url: https://cds.cern.ch/record/615164.

[82] J. W. Backus and W. P. Heising, *Fortran*, IEEE Transactions on Electronic Computers (1964), pp. 382–385.

[83] J. Laskar, C. Froeschlé, and A. Celletti, *The measure of chaos by the numerical analysis of the fundamental frequencies. application to the standard mapping*, Physica D: Nonlinear Phenomena **56** (1992), pp. 253 – 269. url: http://www.sciencedirect.com/science/article/pii/016727899290028L, doi:https://doi.org/10.1016/0167-2789(92)90028-L.

[84] B. Stroustrup, *The C++ programming language*, Pearson Education India, 2000.

[85] G. Van Rossum and F. L. Drake Jr, *Python reference manual*, Centrum voor Wiskunde en Informatica Amsterdam, 1995.

[86] K. Arnold, J. Gosling, and D. Holmes, *The Java programming language*, Addison Wesley Professional, 2005.

[87] M. Borland and R. Soliday, *"application programmer's guide for sdds version 1.5"*, APS LS Note . url: http://ops.aps.anl.gov/asd/oag/manuals/sdds/SDDS.html.

[88] The pandas development team, *pandas-dev/pandas: Pandas*, Feb. 2020. url: https://doi.org/10.5281/zenodo.3509134, doi:10.5281/zenodo.3509134.

[89] A. Belk, P. Defert, P. Hofmann, and R. Keyser, *TFS version 3.1 Table file system reference guide*. Technical Notes - 1991. url: http://cds.cern.ch/record/91632.

[90] C. Candan, *A method for fine resolution frequency estimation from three dft samples*, IEEE Signal Processing Letters **18** (2011), pp. 351–354.

[91] S. van der Walt, S. C. Colbert, and G. Varoquaux, *The numpy array: A structure for efficient numerical computation*, Computing in Science Engineering **13** (2011), pp. 22–30.

[92] *JPype*, GitHub . url: https://github.com/jpype-project/jpype.git.